

## REPORT DOCUMENTATION PAGE

AFRL-SR-AR-TR-04-

Public reporting burden for this collection of information is estimated to average 1 hour per response, including the time for reviewing instructions, searching existing data sources, gathering the required information, reviewing and collecting the information, and completing and reviewing the collection of information. Send comments regarding this burden estimate or any other aspect of this collection of information, including suggestions for reducing the burden, to Washington Headquarters Services, Directorate for Information Operations and Reports, 1215 Jefferson Davis Highway, Suite 1204, Arlington, VA 22202-4302, and to the Office of Management and Budget, Paperwork Project, Washington, DC 20503.

1 reviewing  
information

1. AGENCY USE ONLY (Leave blank)		2. REPORT DATE February 25, 2004	3. REPORT TYPE AND DATES COVERED Final Technical Report (5 Jul 01 - 31 Oct 03)
4. TITLE AND SUBTITLE Unified Framework for Development of Pressure-Strain Correlation, Turbulent Transport and Sub-Grid Stress Closure Models for Turbulence Simulation			5. FUNDING NUMBERS F49620-01-1-0476 2307/BX 61102F
6. AUTHOR(S) Sharath S. Girimaji			
7. PERFORMING ORGANIZATION NAME(S) AND ADDRESS(ES) Texas A&M University Dept of Aerospace Engineering College Station, TX 77843--3141			8. PERFORMING ORGANIZATION REPORT NUMBER
9. SPONSORING/MONITORING AGENCY NAME(S) AND ADDRESS(ES) AFOSR/NA 4015 Wilson Blvd., Room 713 Arlington, VA 22230-1954 Program Manager: Dr. Thomas Beutner			10. SPONSORING/MONITORING AGENCY REPORT NUMBER
11. SUPPLEMENTARY NOTES  <div style="text-align: right; font-size: 2em; font-weight: bold;">20040305 013</div>			
12a. DISTRIBUTION AVAILABILITY STATEMENT APPROVED FOR PUBLIC RELEASE, DISTRIBUTION IS UNLIMITED			12b. DISTRIBUTION CODE
13. ABSTRACT (Maximum 200 words) Study of turbulence is of vital scientific, military and economic interest. Advances in several areas of external aerodynamics and internal combustor flows of interest to Air Force hinge on our ability to clearly understand and adequately predict the effects of turbulence. At the current time, however, there exists a substantial gap between our knowledge of the physics of turbulence phenomenon and the physics that is incorporated into turbulence models, especially subgrid closures. The disciplines of turbulence theory/analysis (e.g., rapid distortion theory, spectral closure models), high-order turbulence modeling (e.g., second-moment closures, structure-based models and realizability constraints) and turbulence simulation (DNS- direct numerical simulations, and LES- large eddy simulations) are evolving independently with very little cross fertilization of ideas. For example, the currently popular LES subgrid closures (e.g., Smagorinsky, dynamic Smagorinsky) are algebraic in nature; completely insensitive to extra rates of strain such as rotation, curvature, and buoyancy and, further, may not even be realizable. These major deficiencies in the LES-SGS modeling are tolerated despite the fact that, in higherorder closures, these physical effects and mathematical constraints have long been represented adequately. Further, we would like to point out that the very premise of detached-eddy simulation (DES) approach - that is seen as the practical computational tool for turbulence - is erroneous. This is due to the fact that that inhomogeneous spatial filtering is inevitable in this method, and yet the governing equations ignore the effects that necessarily arise with inhomogeneous filtering of the velocity field.			
14. SUBJECT TERMS			15. NUMBER OF PAGES 88
			16. PRICE CODE
17. SECURITY CLASSIFICATION OF REPORT U	18. SECURITY CLASSIFICATION OF THIS PAGE U	19. SECURITY CLASSIFICATION OF ABSTRACT U	20. LIMITATION OF ABSTRACT

***AFOSR Project Report***

***Grant No.: F49620-01-1-0476***

***Grant duration: Jan. 2001 – Sept. 2003***

***Program Monitor: Dr. Thomas Beutener***

***Title:***

**Unified framework for development of pressure-strain correlation,  
turbulent transport and sub-grid stress closure models for  
turbulence simulation**

***Principal Investigator: Sharath S. Girimaji***

***Institution: Aerospace Engineering Department, Texas A&M  
University***

**Students: E. Jeong (Ph. D, 2003); A. Murthi (M.S., 2004)**

---

## GENERAL INTRODUCTION.

---

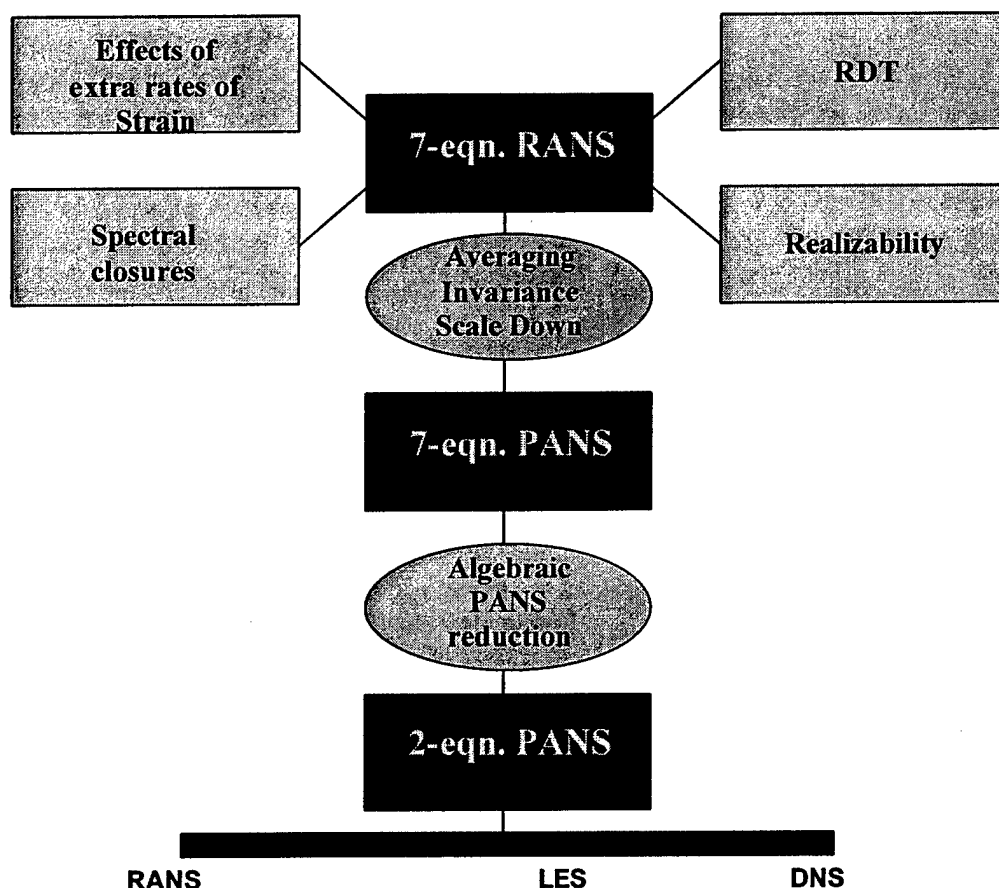
Study of turbulence is of vital scientific, military and economic interest. Advances in several areas of external aerodynamics and internal combustor flows of interest to Air Force hinge on our ability to clearly understand and adequately predict the effects of turbulence. At the current time, however, there exists a substantial gap between our knowledge of the physics of turbulence phenomenon and the physics that is incorporated into turbulence models, especially subgrid closures. The disciplines of turbulence theory/analysis (e.g., rapid distortion theory, spectral closure models), high-order turbulence modeling (e.g., second-moment closures, structure-based models and realizability constraints) and turbulence simulation (DNS- direct numerical simulations, and LES- large eddy simulations) are evolving independently with very little cross fertilization of ideas. For example, the currently popular LES subgrid closures (e.g., Smagorinsky, dynamic Smagorinsky) are algebraic in nature; completely insensitive to extra rates of strain such as rotation, curvature, and buoyancy and, further, *may not even be realizable*. These major deficiencies in the LES-SGS modeling are tolerated despite the fact that, in higher-order closures, these physical effects and mathematical constraints have long been represented adequately. Further, we would like to point out that the very premise of detached-eddy simulation (DES) approach – that is seen as the practical computational tool for turbulence – is erroneous. This is due to the fact that inhomogeneous spatial filtering is inevitable in this method, and yet the governing equations ignore the effects that necessarily arise with inhomogeneous filtering of the velocity field.

Much of the disparity between what is known of turbulence physics and what is incorporated into the LES models is due to the reason that the frameworks of various developments have traditionally been vastly different. *The objective of the research performed under this grant was to find means of unifying these disciplines on a common framework such that turbulence closure models – especially, LES-SGS closures - can benefit from the decades of wisdom and experience incumbent in turbulence theories and high-order closures.*

The flowchart given below summarizes the planned sequence of investigations that is purported to result in a turbulence closure model that can be used at any degree of evolution. We start with the premise that turbulence modeling can be accomplished with some degree of fidelity to the governing Navier-Stokes equations only at the second-order closure level. At this level, different turbulence theories and analyses like RDT (rapid distortion theory), realizability and effects of extra rates of strain (via the Poisson equation for fluctuating pressure) can formally contribute to the closure models of rapid pressure-strain correlation and dissipation. In the flowchart, the rectangular boxes in light blue represent the fundamental theory/analysis studies that directly contribute to the seven-equation second-order (RANS) turbulence modeling closure (dark-blue box). Once the RANS closure has been achieved, one can (proposed future work) systematically develop a seven-equation PANS (partially-averaged Navier-Stokes) model to represent the effects of partially-averaged fields. Under work funded mostly by NASA, we have already established the PANS protocol for simple two-equation models. This experience will definitely aid us in the development of the PANS protocol for seven-equation closure. As the seven-equation closure for PANS or LES-SGS is certain to be infeasible, we will have to effect reduction to a smaller equation set. This can be accomplished by employing algebraic stress modeling approach that has been perfected in our group. This will ultimately result in the

derivation of an algebraic PANS closure model that can be used in the context of PANS or even LES. Thus, the body of turbulence knowledge developed over the years in turbulence theory-analysis-modeling studies can be brought to bear on computing filtered velocity fields. With such models, any new physical effect (rotation, curvature, buoyancy) can be systematically introduced into model closure with resorting to any kind of *ad hoc* modifications.

## Unifying Framework



In the completed research, three important topics that make crucial contributions to the above model development strategy were investigated: (i) **new realizability constraints** for rapid pressure-strain correlation modeling; (ii) new physical modeling constraints that are needed for ensuring **consistency with rapid distortion theory**; and (iii) turbulent transport models for partially-averaged (sub-grid) kinetic energy and dissipation. We will first provide brief

descriptions of each of the topic and present the detailed reports from each study in the following chapters.

**New realizability constraints.** In second-moment-closure method in turbulence modeling, measures to insure a realizable turbulence model are currently limited to constraining the Reynolds stress to physically possible values. These constraints address neither the realizability of the other modified statistical moments (e.g., pressure-strain correlation) nor the underlying causes of unrealizable Reynolds stresses. For achieving increased consistency with flow physics in SMC, we propose the additional requirement that the closure model for each of the unclosed statistical moments in the Reynolds stress equation be individually realizable. We then proceed to derive two realizability constraints on the rapid pressure-strain term: (i) the so-called Mijkl tensor must be positive semi-definite and (ii) the correlation closure must satisfy Schwarz inequality. Calculations with currently-popular models show that unrealizable rapid pressure-strain correlation precedes unrealizable Reynolds stress. It is also demonstrated that when the Launder, Reece and Rodi (LRR) rapid pressure-strain correlation model is modified (truncated) to satisfy the new constraints, Reynolds stress realizability is always preserved. These findings clearly indicate that unrealizable closure model is the cause of Reynolds stress realization violation and highlight the importance of the new constraints. Incidentally, the truncated LRR model - which is fully realizable and piece-wise linear - comes close to satisfying two crucial requirements of a rapid pressure-strain closure.

**New physical constraints based on RDT.** Rapid distortion calculations of initially anisotropic turbulence are performed to better understand the physics of the pressure-strain correlation in strain dominated flows. Based on the results of simulations we infer important physical characteristics of the "rapid" pressure-strain correlation  $\Phi_{ij}^{(r)}$  in mean strain-dominated turbulence: i) it vanishes when there is no production of anisotropy, ii) it tends to decrease Reynolds stress anisotropy, and iii) its magnitude is mostly smaller than that of production. The observed characteristics are proposed as criteria that pressure-strain correlation models should satisfy. Although these properties of  $\Phi_{ij}^{(r)}$  appear intuitively self-evident, all of the current popular models violate the above criteria for a sizeable subset of anisotropic initial conditions. Reynolds stress transport model calculations show that unphysical (inconsistent) and unrealizable model behavior can be directly attributed to these violations.

**Transport models for subgrid kinetic energy and dissipation.** If the filtered stresses are to be calculated from transport equations (rather than algebraic closures), processes such as pressure-strain correlation, turbulent transport and dissipation (in the filtered equation context) need to be modeled. In previous work (performed under NASA grant), we have demonstrated that closure for all processes, except, transport can be inferred from the parent RANS model by simply invoking the averaging-invariance principal in a consistent manner. The turbulent transport model, however, requires independent calibration.

---

# Chapter 1 New perspectives on realizability of pressure-strain correlation closures

---

## 1.1 Introduction

Realizability requirement enunciates the rudimentary expectation that an acceptable turbulence model closure expression be based on the statistics of the velocity field that is physically achievable or realizable. The covariance tensor, or the Reynolds stress, of any velocity field governed by the Navier-Stokes equations is positive semi-definite exhibiting two important characters: the diagonal components (energies) are non-negative and the off-diagonal components satisfy the Schwarz inequality. For second moment-closures (SMC), the realizability constraint as proposed by Schumann (1977) requires that a turbulence model yield Reynolds stresses that satisfy these conditions (see also Lumley, 1978). Over the last two decades, Schumann realizability constraint has served as the theoretical basis for several turbulence models (e.g., Ristorcelli, Lumley and Abid, 1995; Johansson and Hallback, 1994; and Sjogren and Johansson, 2000). In this paper, we revisit the realizability issue and present a new perspective.

We suggest that a SMC turbulence model must *not only yield a positive semi-definite Reynolds stress tensor, but the model expressions for individual unclosed moments (e.g., pressure-strain correlations) must themselves be realizable*. While the theoretical justification for this extended or comprehensive realizability condition is to achieve improved consistency with turbulence physics, there is also an important practical consideration. In SMC (second-moment closure) methodology, Reynolds stress is calculated from an evolution equation. The evolution rate is composed of contributions from production, pressure-strain correlation, turbulent transport, dissipation and other processes. Most of these terms require closure modeling. It is logical then that the most probable of unrealizable calculated stress is unphysical models for the individual terms contributing towards the evolution rate. One of the most fundamental prerequisites of a physically acceptable closure model is that it be realizable. Each unclosed SMC term is a statistical moment, the closure model for which must satisfy certain realizability constraints. For example, an unrealizable pressure-strain correlation model is one in which the closure expression cannot be possibly obtained from any physically permissible (real) pressure and velocity fields. Closure models not satisfying the appropriate realizability constraints (given in Section 1.2) must be considered unphysical and unacceptable.

The current approach attempts to enforce realizability of Reynolds stress without due consideration of the realizability of the underlying closure models. Although such a model may lead to apparently plausible Reynolds stresses, the dynamics of SMC models will certainly be inconsistent with turbulence physics. Such realizability enforcement will defeat the ultimate goal which is to develop turbulence models of high degree of fidelity to the Navier-Stokes equation.

The flow physics underlying the new constraints can be explained as follows. All velocity fields that are solutions of the Navier-Stokes equations are real-valued and, hence, yield a covariance matrix (Reynolds stress) whose diagonal components are positive and off-diagonal components satisfy the Schwarz inequality. However, not all real-valued fields with covariance tensor satisfying the above conditions can be solutions of the flow equations. A permissible flow-field

solution must be real-valued and satisfy additional kinematic criteria such as the appropriate compressibility condition. For example, in incompressible flow, the real-valued velocity field must also be divergence-free. The new constraints proposed in this paper go a step beyond and attempt to eliminate real-valued velocity fields that do not satisfy the additional requirements.

In this paper we will focus on the reliability issues of rapid pressure-strain correlation term. Exploiting the divergence-free character of an incompressible flow field, we derive reliability constraints on the rapid pressure-strain correlation term. Simple analysis shows that many popular linear and non-linear models do not satisfy these constraints. Detailed model calculations are performed in homogeneous turbulence to demonstrate unequivocally that the onset of unrealizable Reynolds stress is preceded by unrealizable rapid pressure-strain correlation. This establishes the cause-effect relationship between unrealizable pressure-strain correlation model and unrealizable Reynolds stress highlighting the importance of the new constraints.

An introduction to the rapid pressure-strain correlation modeling is given in section 2. In section 1.3, we discuss the current reliability approach and motivate the need for additional constraints. The new realizability constraints on the rapid-pressure statistics are derived in section 1.4. Section 1.5 contains the solution procedure and the results are presented in section 1.6. We close with a summary and conclusions section 1.7.

## 1.2 Rapid pressure-strain correlation

The Reynolds stress evolution is equation by:

$$\frac{D\overline{u_i u_j}}{Dt} = P_{ij} - \phi_{ij} - \epsilon_{ij} + T_{ij}, \quad (1.2.1)$$

where  $\overline{u_i u_j}$  is the Reynolds stress. The various terms in the above equation are the time-rate-of-change following the mean flow, production, pressure-strain correlation, dissipation and transport. Several of these require closure modeling.

Pressure-strain correlation modeling methodology for incompressible flows is derived from the early work of Chou (1945). We start with the Poisson equation for the fluctuating pressure:

$$\frac{\partial^2 p}{\partial x_i \partial x_i} = \frac{\partial^2 (p' + p^s)}{\partial x_i \partial x_i} = -2(S_{ij} s_{ji} + W_{ij} w_{ji}) - (s_{ij} s_{ji} + w_{ij} w_{ji}) \quad (1.2.2)$$

Here, and throughout the remainder of the paper, the following notation will be used:  $S_{ij}$  and  $W_{ij}$  represent the strain and rotation rates of mean flow;  $s_{ij}$  and  $w_{ij}$  represent those of the fluctuating field. Repeated English indices will imply summation. The pressure fluctuations are composed of two parts  $p = p^s + p'$ : the slow part ( $p^s$ ) is due to the fluctuating velocity field alone, and the rapid part ( $p'$ ) is due to the interaction between the mean and fluctuation velocity fields. Accordingly, it is normal practice to decompose the pressure-strain correlation into slow and rapid parts ( $\phi_{ij} = \phi_{ij}^s + \phi_{ij}'$ ) and model each component separately (Launder, Reece and Rodi, 1975).

The Poisson equation for fluctuating rapid pressure can be written as

$$\frac{\partial^2 p'}{\partial x_i \partial x_i} = -2(S_{ij} s_{ji} + W_{ij} w_{ji}). \quad (1.2.3)$$

Using the Greens function solution to the Poisson equation, it can be shown that the (rapid) pressure velocity-gradient correlation tensor can be written in the form

$$\overline{p' \frac{\partial u_i}{\partial x_j}} \equiv 2 \frac{\partial \overline{U_k}}{\partial x_l} M_{ilkj}. \quad (1.2.4)$$

The fourth-order tensor  $M_{ijkl}$  is given by

$$M_{ijkl} = -\frac{1}{4\pi} \int \frac{1}{r} \frac{\partial^2 R_{il}}{\partial r_j \partial r_k} d\mathbf{r} \quad (1.2.5)$$

where  $R_{il}$  is the two-point velocity correlation:  $R_{il}(\mathbf{r}) = \overline{u_i(\mathbf{x}) u_l(\mathbf{x} + \mathbf{r})}$ . It is then straight-forward to show that the rapid pressure-strain correlation can be expressed as

$$\phi'_{ij} = 2 p' s_{ij} \equiv 2 \frac{\partial \overline{U_k}}{\partial x_l} (M_{ilkj} + M_{jlik}) \quad (1.2.6)$$

Modeling rapid pressure-strain correlation is tantamount to modeling the  $M_{ijkl}$  tensor. Complete description of the  $M_{ijkl}$  tensor requires the knowledge of the Reynolds stress (compatibility tensor) and the so-called dimensionality tensor ( $D_{ij}$ ) as is well explained in Kassinos, Reynolds and Rogers (2001). The evolution of dimensionality tensor is governed, to a large extent, by the initial dimensionality and the mean-velocity gradients. The dimensionality tensor is unclosed in terms of the single-point tensors used in the conventional SMC methods. For the given Reynolds stress, the rapid pressure-strain correlation can take a range of values depending on the dimensionality of turbulence. This is the crux of the closure problem. While carrying evolution equations for dimensionality is an option, it is not generally undertaken due to the added computational expense. The practice in traditional SMC modeling is to postulate a closure expression for the  $M_{ijkl}$  tensor that is based on some implied average value of dimensionality tensor. In effect, the conditional (based on a specific value of dimensionality tensor) correlation between pressure and strain fluctuations is modeled with the unconditional correlation (based on some average dimensionality tensor). Thus, the need for dimensionality tensor is obviated, at the expense of accuracy.

Lacking knowledge of the dimensionality tensor, the closure expression for pressure-strain correlation is generally required to satisfy several physical and mathematical constraints to ensure some degree of fidelity of the flow physics. A complete list of currently mandated constraints can be found in Pope (2000). Three of the important constraints are that rapid pressure-strain correlation model must (i) be linear in Reynolds stress; (ii) confirm to a specific functional form (given in equation 1.2.6); and, (iii) lead to realizable Reynolds stress. While the need for the realizability requirement is now clear, the linearity requirement also stems from



important turbulence physics. It is easy to see that Poisson equation for rapid pressure is linear in fluctuating velocity (Reynolds, 1976). Therefore, the rapid or linear pressure term cannot increase or proliferate the number of (Fourier) modes of fluctuation. In other words, the rapid pressure term conserves the number of fluctuating modes. Any non-linear model cannot preserve this important physical character rapid pressure. The  $M_{ijk}$ -form requirement is a consequence of the form of the Greens function solution of the Poisson equation. As pointed out in Pope (2000), currently, there exists no rapid pressure-strain correlation model that satisfies all the required constraints. Specifically, none of the current models satisfy all realizability and linearity requirements. In fact, there has been much speculation that it is virtually impossible to satisfy realizability fully with linear models (Lumley, 1978). While realizability is an important constraint, it is equally desirable to achieve it in a manner consistent with turbulent physics, that is, without compromising on the other two physical requirements.

In this paper we propose additional constraints on  $\phi'_{ij}$  and  $M_{ijk}$  that should enable the development of more accurate closure models.

### 1.3 Realizability constraints

We will first discuss the strong and weak forms of Schumann constraints. Realizability of Reynolds stresses is most conveniently considered in terms of the determinant of the normalized Reynolds-stress tensor:

$$F \equiv \det \left( \frac{\overline{u_i u_j}}{\frac{1}{3} \overline{u_k u_k}} \right) \quad (1.3.1)$$

In the realizable state-space of Reynolds stress (Lumley invariant triangle),  $F$  is positive:  $F$  is negative through most of the unrealizable space. The realizable and the unrealizable Reynolds stress state-spaces are separated by two-componential turbulence in which determinant  $F$  vanishes. The current realizability conditions constrain the behavior of the model in the neighborhood of  $F=0$ .

**Strong realizability.** The strong Reynolds stress realizability condition requires the turbulence model to satisfy the following conditions (Pope, 2000):

$$\left( \frac{dF}{dT} \right)_{F=0} = 0; \quad \left( \frac{d^2 F}{dT^2} \right)_{F=0} > 0. \quad (1.3.2)$$

The strong realizability condition permits accessibility to two-component turbulence. Rigorous implementation of strong realizability constraints to develop closure models is best exemplified in Ristorcelli, Lumley and Abid (1995), Sjogren and Johansson (2000), etc. In fact, in Johansson and Hallback (1994) a recipe for deriving a rapid pressure-strain correlation model that satisfies the strong realizability constraint at any order of tensor expansion is provided. It is found that the fourth-order model was successful over a wider range of flows than typical linear models. In Sjogren and Johansson (2000), the use of strong realizability constraint to develop slow pressure correlation and anisotropic dissipation are also summarized.

**Weak realizability.** Many authors point to major difficulties in enforcing the strong realizability constraint and opt for the easier to implement weak realizability version.

The weak realizability constraint simply requires that the rate of change of  $F$  be positive as the two-componential limit is approached (Pope, 2000):

$$\left(\frac{dF}{dT}\right)_{F=0} > 0. \quad (1.3.3)$$

This constraint doesn't permit access to two-component turbulence. The stochastic realizability analysis of Durbin and Speziale (1994) is a variant of the weak-realizability approach. They demonstrate that every turbulence model equation can be represented by an equivalent stochastic equation. The requirement that the coefficient of the random forcing term be real yields constraints on the pressure-strain correlation model. This approach leads to the dependence of the rapid pressure-strain correlation model coefficients on the coefficients in the dissipation and the slow pressure-strain correlation models. Such interdependence of model coefficients is not physically justifiable. For example, if turbulence model yields unrealizable results in the rapid distortion limit, it is the rapid pressure-strain correlation model that needs modification. Slow pressure-strain correlation and dissipation processes are completely irrelevant in this limit and modifying their models to achieve realizability must be deemed unphysical. The realizability issues of each process should be considered independently as is well demonstrated in Sjogren and Johansson (2000).

**Need for further constraints.** In the second-moment closure approach, Reynolds stress is calculated using a modeled evolution equation. Any non-physical behavior of the Reynolds stress must originate from unphysical closure models in its evolution equation. In Navier-Stokes turbulence, the realizability of the Reynolds stress is achieved while maintaining all the contributing statistical moments individually realizable. Any realizability analysis is incomplete without the examination of the realizability of the individual closure models that contribute towards Reynolds stress evolution. The strong realizability approach indirectly addresses this issue, but only in the two-componential turbulence limit. The weak realizability approach, as currently practiced, completely ignores the realizability of individual moments in the Reynolds stress evolution equation. Thus, both the strong and weak realizability approaches can and do (as will be demonstrated later) permit unrealizable pressure-strain correlation values.

In order to achieve a greater degree of consistency with turbulence physics, we recommend that the closure model for each moment in the Reynolds stress evolution equation be individually realizable, not only in the two-componential limit but also at all other states of turbulence. Physically achievable or realizable models for each of the unclosed statistical moments must satisfy the following requirements:

- (a) Auto-covariances must be non-negative.
- (b) Cross-covariances must satisfy Schwarz inequality.

In this paper, we address the realizability of the rapid pressure-strain correlation term. In most modeling methods, it is the  $M_{ijkl}$  tensor that is first modeled – see for example, Launder, Reece and Rodi (1975); Ristorcelli, Lumley and Abid (1995) or equation (54) in Sjogren and Johansson (2000) – and the pressure-strain correlation closure is simply obtained from equation (1.2.6). Hence, postulating constraints on  $M_{ijkl}$  is as effective and useful as constraining pressure-strain correlation itself. Here, we derive constraints on the  $M_{ijkl}$  tensor that guarantees realizable rapid pressure-stress correlation.

The need for further constraints on  $M_{ijkl}$  can also be motivated from the turbulence structure tensors point of view. As Kassinos et al (2001) point out, a statistically complete one-point description of turbulence requires specification several tensors: componentiality or Reynolds stress ( $R_{ij}$ ); Dimensionality ( $D_{ij}$ ); Circularity ( $C_{ij}$ ); and, finally, stropholysis ( $Q_{ijk}$ ). In general, each tensor carries independent information and all of them are needed to fully specify the one-point statistical state of turbulence. It then stands to reason that closure for all tensors should be individually realizable. In the special case of incompressible homogeneous turbulence these structure tensors can be related to the  $M_{ijkl}$  tensor (Kassinos et al, 2001):

$$Q_{ijk} = e_{ipq} M_{jqpk}; R_{ij} = M_{ijrr}; D_{ij} = M_{rrij}; F_{ij} = e_{imp} e_{jrs} M_{psrm}, \quad (1.3.4)$$

where  $e_{ijk}$  is the alternating tensor. Therefore, in homogeneous incompressible turbulence, all physical and realizability issues are embodied in  $M_{ijkl}$  tensor. Hence, constraints that can guarantee the physical fidelity of this tensor are of great importance.

#### 1.4 Realizability of rapid pressure moments

The concept of realizability requires that the closure models for turbulence statistics are based on a velocity field that is realizable or physically achievable. But what is a physically possible fluctuating velocity field? It is generally, although tacitly, assumed that any real-valued vector field (as opposed to complex or imaginary fields) is an achievable velocity field. Any real-valued vector field would yield non-negative values for the diagonal components of Reynolds stress. Only complex or imaginary velocity field would lead to negative energy components. This argument is the basis of Schumann constraints which permit real vector fields.

We argue that not all real-valued vector fields are achievable velocity fields. Additional kinematic constraints must be satisfied including the compressibility condition. If a flow is incompressible, then the velocity vector field must be divergence free at all points in space and time. Equivalently, the pressure field obtained by Poisson equation from a candidate real-valued vector field must also be real-valued. *Thus, a fully realizable turbulent velocity field must not only be real-valued, but also be divergence free. Alternatively, the implied pressure field must be real.* The incompressibility aspect of the velocity field is not considered in any of the current realizability methods. While the Schumann constraints are necessary for achieving a realizable turbulence model, they are not sufficient.

The incompressibility requirement can be enforced by constraining the pressure fluctuations. It is the pressure field, after all, that preserves the incompressibility of the flow. Further, pressure gradient is responsible of the evolution of the velocity field. It is, therefore, essential to mandate realizable pressure statistics along with constraints on the Reynolds stress. For compressible velocity fields, the divergence of the velocity field must be consistent with density fluctuations. Then, the realizability issues of the velocity field will be inextricably coupled with those of pressure and temperature statistical moments. Compressible flows will be considered in future works.

**Realizability bounds.** In homogeneous turbulence, the pressure-strain correlation ( $\phi_{ij}$ ) is identical in magnitude and opposite in sign to the velocity pressure-gradient correlation ( $\Pi_{ij}$ ):

$$\Pi_{ij} = \overline{u_i \frac{\partial p}{\partial x_j} + u_j \frac{\partial p}{\partial x_i}} = -2\overline{p' s_{ij}} = -\phi'_{ij}. \quad (1.4.1)$$

The velocity pressure-gradient correlation is more fundamental as it is the one that appears in the Reynolds stress closure equation before decomposition into homogeneous and inhomogeneous components. We will now investigate the realizability bounds on the rapid portion of the velocity pressure-strain correlation ( $\phi'_{ij}$ ). The magnitude of this correlation is bound by

$$|\phi'_{\alpha\beta}| = \left| \overline{u_\alpha \frac{\partial p'}{\partial x_\beta} + u_\beta \frac{\partial p'}{\partial x_\alpha}} \right| \leq \left| \overline{u_\alpha \frac{\partial p'}{\partial x_\beta}} \right| + \left| \overline{u_\beta \frac{\partial p'}{\partial x_\alpha}} \right|. \quad (1.4.2)$$

Schwarz inequality as applied to the last two correlations on the extreme right requires

$$\left| \overline{u_\alpha \frac{\partial p'}{\partial x_\beta}} \right| \leq \overline{u_\alpha u_\alpha}^{\frac{1}{2}} \overline{\frac{\partial p'}{\partial x_\beta} \frac{\partial p'}{\partial x_\beta}}^{\frac{1}{2}}. \quad (1.4.3)$$

(Whereas repeated English indices imply summation, Greek indices do not.) As a consequence, the rapid portion of velocity pressure correlation must be bounded by:

$$|\phi'_{\alpha\beta}| \leq \overline{u_\alpha u_\alpha}^{\frac{1}{2}} \overline{\frac{\partial p'}{\partial x_\beta} \frac{\partial p'}{\partial x_\beta}}^{\frac{1}{2}} + \overline{u_\beta u_\beta}^{\frac{1}{2}} \overline{\frac{\partial p'}{\partial x_\alpha} \frac{\partial p'}{\partial x_\alpha}}^{\frac{1}{2}}. \quad (1.4.4)$$

Since  $\overline{\frac{\partial p'}{\partial x_\beta} \frac{\partial p'}{\partial x_\beta}}^{\frac{1}{2}} \leq \overline{\frac{\partial p'}{\partial x_i} \frac{\partial p'}{\partial x_i}}^{\frac{1}{2}}$ , the following inequality must hold:

$$|\phi'_{\alpha\beta}| \leq (\overline{u_\alpha u_\alpha}^{\frac{1}{2}} + \overline{u_\beta u_\beta}^{\frac{1}{2}}) \overline{\frac{\partial p'}{\partial x_i} \frac{\partial p'}{\partial x_i}}^{\frac{1}{2}} = G_{\alpha\beta}, \quad (1.4.5)$$

where the second identity defines the tensor  $G_{\alpha\beta}$ . Due to the fact that we replace  $\overline{\frac{\partial p'}{\partial x_\beta} \frac{\partial p'}{\partial x_\beta}}^{\frac{1}{2}}$  in the

inequality by the larger  $\overline{\frac{\partial p'}{\partial x_i} \frac{\partial p'}{\partial x_i}}^{\frac{1}{2}}$ , we must regard the constraint in equation (1.4.5) as less

stringent than required to satisfy the Schwarz inequality. This inequality is valid for homogeneous and inhomogeneous flows. From equation (1.4.5), it can be seen that the realizability bounds on the rapid pressure-strain correlation depends on the componentiality (via

$\overline{u_\alpha u_\alpha}$ ) and dimensionality (via  $\overline{\frac{\partial p'}{\partial x_\beta} \frac{\partial p'}{\partial x_\beta}}^{\frac{1}{2}}$ ) of the turbulence.

The inequality in expression (1.4.5) forms the basis of the new constraints developed in this paper. In the limit of two-componential turbulence, this inequality yields the strong realizability constraint: if velocity fluctuations in the  $a$ -direction vanish, then

$$\overline{u_\alpha u_\alpha} = 0, \quad (1.4.6)$$

which immediately implies

$$\phi'_{\alpha\alpha} \approx \left| \overline{u_\alpha u_\alpha} \right|^{\frac{1}{2}} \overline{\frac{\partial p'}{\partial x_\beta} \frac{\partial p'}{\partial x_\beta}}^{\frac{1}{2}} = 0. \quad (1.4.7)$$

Apart from this requirement, the inequality in equation (1.4.5) has not been exploited for formulating all other possible modeling constraints. For example, it is obvious that when the pressure-gradient variance vanishes, so must the pressure-strain correlation. Yet, this fundamental requirement has never been posed as a modeling constraint. This is most likely due to the fact that rapid pressure-gradient statistics (indicative of the dimensionality of turbulence) are not considered in traditional modeling approaches where only the Reynolds stresses (componetiality of turbulence) is solved for explicitly. In this work, we will derive an exact analytical expression for rapid pressure-gradient variance. Knowledge of rapid pressure-gradient variance opens up the possibility of a new set of constraints of the rapid pressure-strain correlation that are much more general than the strong realizability requirement.

**Rapid pressure-gradient variance.** Multiplying equation (1.2.3) through by the rapid pressure and taking average leads to:

$$\overline{p' \frac{\partial^2 p'}{\partial x_i \partial x_i}} = -2S_{ij} \overline{p' s_{ij}} - 2W_{ij} \overline{p' w_{ji}}. \quad (1.4.8)$$

In homogeneous turbulence which is of interest here, we can further write

$$\overline{p' \frac{\partial^2 p'}{\partial x_i \partial x_i}} = \overline{\frac{\partial p'}{\partial x_i} \frac{\partial p'}{\partial x_i}} = -2S_{ij} \overline{p' s_{ij}} - 2W_{ij} \overline{p' w_{ji}} = -2 \frac{\partial \overline{U_i}}{\partial x_j} \overline{p' \frac{\partial u_j}{\partial x_i}}. \quad (1.4.9)$$

It was shown in the previous section that the rapid pressure-strain correlation tensor is related to the fourth order tensor  $M_{ijkl}$ . The relationship between this tensor and the pressure-gradient variance can be easily derived from equations (1.2.4) and (1.4.9):

$$\overline{p' \frac{\partial^2 p'}{\partial x_i \partial x_i}} = 4 \frac{\partial \overline{U_j}}{\partial x_i} \frac{\partial \overline{U_k}}{\partial x_i} M_{ijkl}. \quad (1.4.10)$$

Thus, the rapid pressure-gradient variance can be obtained as a function of the rapid pressure-strain correlation. In purely-strained flows, the relationship is even simpler:

$$\overline{p' \frac{\partial^2 p'}{\partial x_i \partial x_i}} = 2S_{ij} \overline{p' s_{ij}} \quad (1.4.11)$$

It has to be pointed out that the Kassinos, Reynolds and Rogers (2001) derive an expression for pressure-gradient variance in the rapid reference-frame rotation limit. The expression involves

the rotation rate and the circularity tensor which contains information about the large-scale vorticity. The circularity tensor is not known the traditional second-moment closure modeling.

### *New realizability constraints*

With the knowledge of rapid pressure-gradient variance, we will now formulate the new realizability constraints in one-, two- and three-componential homogeneous turbulence. These pressure-strain correlation constraints account for dimensionality as well as componentiality, whereas, the Schumann constraints takes only componentiality into consideration.

**Constraint #1.** In two-componential turbulence (with no velocity fluctuations in the  $a$  direction), the realizability of rapid pressure-strain correlation requires

$$\phi'_{\alpha\alpha} = \phi'_{\alpha\alpha} = 0. \quad (1.4.12)$$

The values of the off-diagonal terms will depend on the dimensionality of the turbulence. This is similar to the strong realizability requirement. Alternatively, the realizability constraint on  $M_{ijkl}$  in the two-component limit is

$$M_{aaij} = 0. \quad (1.4.13)$$

In one-component turbulence, all three diagonal pressure-strain correlation components must be zero. The diagonal components in the direction of zero fluctuating velocity clearly must be zero for the same reason as above. The correlation component in the third direction is zero for a different reason. Continuity requires that the fluctuating pressure gradient be zero in the direction of velocity. Thus, in one-dimensional turbulence (if  $\beta$  is the direction of non-zero velocity) the realizability constraints are

For  $\alpha \neq \beta$ :  $\overline{u_\alpha u_\alpha} = 0$ , implying  $\phi'_{\alpha\alpha} = 0$ ; and  $M_{aaij} = 0$ .

For  $\alpha = \beta$ :  $\frac{\partial p}{\partial x_\alpha} \frac{\partial p}{\partial x_\alpha} = 0$ , implying  $\phi'_{\alpha\alpha} = 0$ ; and  $M_{ijaa} = 0$ . (1.4.14)

The pressure-strain constraints are valid for the slow term as well.

**Constraint # 2.** The rapid pressure-strain correlation model must lead to non-negative values for the rapid pressure-gradient variance. Physically, this ensures that the pressure fluctuations are real and, hence, the velocity field is divergence-free. Thus, the first of two realizability constraints on  $M_{ijkl}$  is

$$\frac{\partial \overline{U_j}}{\partial x_i} \frac{\partial \overline{U_k}}{\partial x_l} M_{ijkl} \geq 0. \quad (1.4.15)$$

This inequality should hold for any arbitrary non-zero mean-velocity gradient tensor. Hence, the  $M_{ijkl}$  must be positive semi-definite. Unless  $M_{ijkl}$  is positive semi-definite, there will be a mean velocity field, for which the fluctuating rapid pressure gradient will be negative.

For purely strained flows, positivity condition on the pressure-gradient variance can also be written as

$$S_{ij} \phi'_{ij} \geq 0. \quad (1.4.16)$$

**Constraint # 3** The pressure-gradient variance must not only be positive, but also be large enough to satisfy the Schwarz inequality on rapid pressure-strain correlation. This can be guaranteed if the model satisfies the following inequality (from equations 1.4.10 and 1.4.5):

$$2\left|\overline{p's_{\alpha\beta}}\right| \leq \left|\overline{p's_{\alpha\beta}}\right| \leq 2(\overline{u_\alpha u_\alpha}^{\frac{1}{2}} + \overline{u_\beta u_\beta}^{\frac{1}{2}}) \left[ \frac{\partial \overline{U}_j}{\partial x_i} \frac{\partial \overline{U}_k}{\partial x_l} M_{ijkl} \right]^{\frac{1}{2}} \quad (1.4.17)$$

Satisfaction of this constraint in conjunction with constraint # 2 will ensure realizable velocity pressure-gradient correlation. For purely strained flows the above constraint can be expressed directly in terms of pressure-strain correlation:

$$\left|\overline{\phi'_{ij}}\right| \leq (\overline{u_\alpha u_\alpha}^{\frac{1}{2}} + \overline{u_\beta u_\beta}^{\frac{1}{2}}) \left[ \overline{S_{ij}\phi'_{ij}} \right]^{\frac{1}{2}}. \quad (1.4.18)$$

It can be recognized that the first constraint (equation 1.4.12), derived for one-and two-componential turbulence, is equivalent to the strong realizability constraint. However, constraint # 2 (equation 1.4.15) and #3 (equation 1.4.17) are not addressed in existing literature. In light of these new constraints several questions arise:

- Do the current models violate the new realizability constraints? If not, the new constraints are only of academic interest.
- Does Reynolds-stress realizability automatically imply realizability of pressure-strain correlation? If yes, then the current constraints would be redundant.
- Conversely, does pressure-strain correlation realizability guarantee Reynolds-stress realizability? If yes, then the new realizability constraints are more complete and the Reynolds-stress realizability is redundant.
- Or, are the old and new realizability constraints mutually exclusive so that both should be required of the pressure-strain correlation models?

In an attempt to find the answers, we perform model calculations in the next section.

### 1.5 Solution procedure

Fourth-order Runge-Kutta scheme is used for time integration of second-order closure equations. The mean flows investigated are

<p><i>Homogenous shear (HS)</i></p> $\frac{\partial \overline{U}_i}{\partial x_j} = \begin{bmatrix} 0 & S & 0 \\ S & 0 & 0 \\ 0 & 0 & 0 \end{bmatrix}$	<p><i>Plain strain (PS)</i></p> $\frac{\partial \overline{U}_i}{\partial x_j} = \begin{bmatrix} S & 0 & 0 \\ 0 & -S & 0 \\ 0 & 0 & 0 \end{bmatrix}$	<p><i>Axisymmetric contraction (AC)</i></p> $\frac{\partial \overline{U}_i}{\partial x_j} = \begin{bmatrix} S & 0 & 0 \\ 0 & -S/2 & 0 \\ 0 & 0 & -S/2 \end{bmatrix}$
<p><i>Axisymmetric expansion (AE)</i></p> $\frac{\partial \overline{U}_i}{\partial x_j} = \begin{bmatrix} -S & 0 & 0 \\ 0 & S/2 & 0 \\ 0 & 0 & S/2 \end{bmatrix}$	<p><i>Mixed shear (MS)</i></p> $\frac{\partial \overline{U}_i}{\partial x_j} = \begin{bmatrix} 0.8S & 0.2S & 0 \\ 0 & -0.8S & 0 \\ 0 & 0 & 0 \end{bmatrix}$	

Evolution trajectories are tracked on the  $(\xi, \eta)$  invariant plane, where the invariants are defined by  $6\eta^2 = b_{ij}b_{ji}$  and  $6\xi^3 = b_{ij}b_{jk}b_{ki}$ . For each mean flow, numerous initial values of  $(\xi, \eta)$  encompassing the entire Lumley triangle, are chosen. Each point  $(\xi, \eta)$  on the Lumley triangle corresponds to six combinations of anisotropy tensor components. All six combinations are investigated. All together, it results in over 64000 initial conditions considered for each mean flow. In all simulations, initial values of  $k$  ( $k_o$ ) and  $\varepsilon$  ( $\varepsilon_o$ ) are taken (without any loss of generality) to be unity. Calculations are performed for three values of  $S^* = Sk_o/\varepsilon_o$ : 5, 15 and 50. The case  $S^* = 5$  corresponds to near equilibrium turbulence, while  $S^* = 50$  corresponds to rapidly distorted turbulence.

## 1.6 Realizability study

The results are presented in four steps: (i) the set of anisotropy initial conditions that ultimately lead to RS-realizability violation are identified for each model; (ii) contribution of the various terms in the Reynolds stress evolution equation towards unrealizable trajectories is examined, and the term responsible for RS-realizability violation is identified; (iii) connection between RS-realizability violation and an unrealizable rapid pressure-strain correlation model is analyzed; (iv) truncated LRR model (Girimaji, 2002), which satisfies all constraints listed in Pope (2000) and also rapid PSC- realizability constraint (1.4.17), is considered.

### 1.6.1 RS-realizability violation

Solution trajectories obtained from model calculations can be classified into two types, namely the ones that are always realizable and asymptote to equilibrium and the ones that violate realizability (leave the Lumley triangle). The area in the Lumley triangle containing initial conditions from which only realizable trajectories originate is called the *basin-of-attraction*. The area inside the Lumley triangle, but outside the basin-of-attraction will be called as the *basin-of-violation*. Notice though, that initial conditions  $(\xi, \eta)$  inside the basin-of-violation may or may not lead to unrealizable solution trajectories depending on the combination of  $b_{ij}$ -components. The line that demarcates two basins is called the *violation boundary*. The location of the violation boundary depends upon pressure-strain model employed, mean flow, and  $S^*$ -value. All initial conditions below the violation boundary belong to the basin-of-attraction.

Violation boundaries for the LRR-QI model are shown in figure 1 at  $S^* = 5$  and in figure 2 at  $S^* = 50$ . At  $S^* = 5$ , the smallest basin-of-violation is observed in the homogenous shear flow and the largest one in the axisymmetric expansion flow. Basins-of-violation for other three cases fall between those two regions. The basin-of-violation in the axisymmetric contraction flow is smaller than the one in the axisymmetric expansion flow; and such region in the plain strain flow is almost similar to the one in the mixed shear flow. The mixed shear flow considered here has 80% of strain and only 20% of rotation. Hence, basins-of-violation in this flow and in the plain strain flow are similar. Once the ratio of strain to rotation is decreased, the mixed shear basins-of-violation start to transform towards the basins-of-violation corresponding to the homogeneous shear flow. With increasing  $S^*$ , a violation boundary goes down, and the basin-of-violation area increases. The overall shape of the region does not change though. Such tendencies are observed in all flows (see figures 1.1 and 1.2).



The unrealizable regions corresponding to the SSG model (figures 1.3 and 1.4) behave similarly. The only notable difference between LRR-QI and SSG models is that basins-of-violation for the SSG model are larger than those of the LRR-QI model in all flows considered.

Selected solution trajectories evolving from the basin-of-attraction and outside that area are presented in figures 1.5-1.9. In the figures, a violation boundary is shown by solid thick line. The cross (⊗) marks the equilibrium point in the flow. The values of the anisotropy tensor components in the equilibrium point are shown in table 1.1 for different flow conditions and for two models: LRR-QI and SSG. Some of equilibrium  $b_{ij}$ -values given in table 1.1 slightly differ from those used in previous studies. It is explained by different  $C_{e2}$  value employed in those studies. The rest of the symbols in figures 1.5-1.9 show initial conditions from which solution trajectories evolve. Arrows on trajectories show the direction of trajectory evolution.

**Table 1.1** Equilibrium anisotropy values.

	LRR-QI model				SSG model			
	$b_{11}$	$b_{22}$	$b_{33}$	$b_{12}$	$b_{11}$	$b_{22}$	$b_{33}$	$b_{12}$
A	-	-	-	-	-	-	-	-
C	0.2513	0.1256	0.1256	0.0000	0.2267	0.1134	0.1134	0.0000
HS	0.1565	-	-	-	0.2216	-	-	-
		0.1223	0.0342	0.1877		0.1485	0.0731	0.1640
AE	0.2855	-	-	-	0.3216	-	-	-
		0.1428	0.1428	0.0000		0.1608	0.1608	0.0000
PS	-	-	-	-	-	-	-	-
	0.2167	0.2510	0.0342	0.0000	0.1861	0.2548	0.0688	0.0000
M	-	-	-	-	-	-	-	-
		0.2334	-	-		0.2616	-	-
S	0.1992		0.0342	0.0889	0.1885		0.0731	0.1025

In the homogenous shear flow (figure 1.5) trajectories evolving from initial conditions below the violation boundary end up in the equilibrium point. In the plain strain flow, realizable trajectories evolve in the complicated manner (figure 1.6) as they make loops before reaching equilibrium. The behavior of the realizable trajectories in the mixed shear flow (figure 1.7) resembles the behavior of trajectories in both plain strain and homogenous shear flows. In the presence of shear though, loops are reduced and they do not reach axisymmetric expansion and axisymmetric contraction limits, as it would be in the plain strain flow (figure 1.6). The shape of trajectories appears to depend on the ratio of strain to shear. It is observed that when the ratio reduces, trajectories evolve closer to the homogenous shear flow case. In the axisymmetric contraction flow, the trajectories ( $\circ$ ,  $\downarrow$ ,  $\diamond$ ) that asymptote to equilibrium also exhibit the looping behavior (figure 1.8). In the axisymmetric expansion flow, similar behavior of realizable trajectories is observed (figure 1.9). In figures 1.5-1.9, trajectories which start from initial conditions above the violation boundary evolve outside the Lumley triangle and so, are unrealizable.

Results of this subsection show that *there exists a sizable finite set of initial conditions for which the solution trajectories violate realizability. The basin-of-violation grows with increasing the*

parameter  $S^*$  in all flows. It also depends on the rapid pressure-strain model and the mean flow. We will now try to identify which term in the Reynolds stress evolution equation contributes most toward RS-realizability violation.

### 1.6.2 Closure model responsible for RS-realizability violation

The closure model responsible for the RS-realizability violation can be identified by examining the contribution of various terms in the Reynolds stress evolution equation. The evolution equation of the Reynolds stresses can be split into three parts:

1. due to production

$$\left[ \frac{d}{dt} \overline{u_i u_j} \right]^p = P_{ij}, \quad (1.6.1)$$

2. due to rapid pressure-strain

$$\left[ \frac{d}{dt} \overline{u_i u_j} \right]^r = R_{ij}^r, \quad (1.6.2)$$

3. due to non-linear processes of dissipation and slow pressure-strain correlation

$$\left[ \frac{d}{dt} \overline{u_i u_j} \right]^s = R_{ij}^s - \frac{2}{3} \varepsilon \delta_{ij}. \quad (1.6.3)$$

At every point, the resultant from these three parts will determine the direction of a trajectory. Some unrealizable trajectories are shown in figures 1.10 and 1.11 in plain strain and axisymmetric expansion flows. They correspond to the initial conditions (□) in figure 1.6 (PS) and (★) in figure 1.9 (AE). Contribution of the production, the rapid pressure-strain correlation, and non-linear processes in trajectory evolution is depicted at two different stages, when  $M_{ijkl}$  and RS violations occur.

In figure 1.10, contribution of different parts towards anisotropy evolution is qualitatively similar at both points. Details can be summarized as follows:

- Production (p) drives the trajectory parallel to the two-component limit and hence, does not lead to realizability violation. Since this term is 'exact', it is indeed expected to be physically realizable.
- Slow pressure-strain and dissipation (s) always attract the trajectory towards the interior of the Lumley triangle. These terms have isotropizing, rather than anisotropizing effect.
- Rapid pressure-strain correlation (r) points in a direction away from the Lumley triangle. It is clear that this is the component responsible for RS realizability violation.

The same trends are seen in figure 1.11 and in other unrealizable trajectories investigated (figures not shown).

It can be said with a great degree of generality that this is a rapid pressure-strain correlation model, which leads to an unrealizable trajectory of the Reynolds stresses in considered flows. Thus, conclusion of this subsection is that *the rapid pressure-strain component is responsible for Reynolds stress realizability violation.*

### 1.6.3 Connection between RS- and rapid PSC-realizabilities

All of the unrealizable trajectories from the previous subsection are now investigated for compliance with  $M_{ijkl}$  constraint (1.4.17). As it is seen on figures 1.10 and 1.11, violation of the  $M_{ijkl}$  constraint precedes RS-realizability violation. It happens in all cases considered. In figures 1.12-1.15, the line formed by points at which the  $M_{ijkl}$  constraint is first violated by unrealizable trajectories, is shown in various mean flows for LRR-QI and SSG rapid pressure-strain correlation models. We will call this line as the  $M_{ijkl}$ -violation boundary. In all these cases the line is nearly parallel to the two-component line of the Lumley triangle. Comparing SSG and LRR-QI models, one can say that the former violates the  $M_{ijkl}$  constraint over larger portion of the Lumley triangle than the LRR-QI model.

Investigation of realizable trajectories reveals a surprising fact. Although most of them satisfy the  $M_{ijkl}$  constraint, some trajectories do violate it. In figure 1.16, two sample trajectories calculated with the LRR-QI model are shown in the axisymmetric expansion flow at  $S^* = 50$ . One of the trajectories (starting from ?) becomes unrealizable at (⊗) after violating the  $M_{ijkl}$  constraint at (⊘). The other trajectory (starting from □) violates the  $M_{ijkl}$  constraint at (⊘), but the Reynolds stresses remain realizable at all times. In fact, at later stages the  $M_{ijkl}$  constraint is again satisfied by the very same trajectory as it asymptotes to the equilibrium point. However, because the  $M_{ijkl}$ -constraint violation occurs, the behavior of this trajectory must be deemed unphysical.

Figure 1.16 demonstrates clearly that realizable Reynolds stresses do not always guarantee the realizable rapid pressure-strain correlation. It means that new  $M_{ijkl}$  constraint (1.4.17) cannot be guaranteed even by the strong realizability condition. Prompted by this finding, an investigation of non-linear rapid pressure-strain correlation models (Shih and Lumley, 1985; Sjogren and Johansson, 2000) that satisfy the strong realizability condition is performed. The SL model always produces realizable trajectories. However, this model yields unrealizable rapid pressure-strain correlations over a significant portion of the Lumley triangle near the two-component line. These unrealizable zones for the plain strain and axisymmetric contraction cases are shown in figure 1.17.

Calculations were also performed with a fourth-order rapid pressure-strain correlation model of Sjögren and Johansson (2000). The coefficients of this model are

$$g_1 = -0.143, g_2 = 0.0295, g_3 = -0.0484, g_4 = 14.$$

The relationship between  $g$ 's and  $f$ 's can be found in Sjögren and Johansson (2000). It was found that this model yields fully realizable results everywhere except the near vicinity of the two-component turbulence line. While the Reynolds stresses are always realizable (as guaranteed by the model development), the pressure-strain correlation shows small region of unrealizability.

The final conclusion from this subsection is that *the rapid pressure-strain realizability constraint cannot be guaranteed by compliance with strong realizability.*

### 1.6.4 Truncated LRR model

The new PSC-realizability constraint (1.4.17) should aid in the development of simple rapid pressure-strain correlation models with higher degree of fidelity to turbulence physics. As a

simple demonstration, a new truncated (clipped) LRR model for the pressure-strain correlation has been derived in Girimaji (2002):

$$R_{ij} = \begin{cases} R_{ij}^s + R_{ij}^r & \text{if Constraint (1.4.17) is valid} \\ R_{ij}^s & \text{if (1.4.17) is violated} \end{cases} \quad (1.6.4)$$

In the model, terms  $R_{ij}^s$  and  $R_{ij}^r$  are corresponding slow and rapid components of the LRR-QI pressure-strain correlation model. This model is piece-wise linear. Due to its simplicity (compared to non-linear models (Shih and Lumley, 1985; Sjogren and Johansson, 2000) satisfying strong realizability), it is likely to be of high practical value. We do not advocate the use of this clipped model in practical computations. Rather, we use it here to demonstrate that satisfying the new constraints will guarantee Reynolds stress realizability.

By testing model (1.6.4) in different flows, it was confirmed that the truncated LRR model is realizable for all initial conditions in the Lumley triangle. Sample corrected trajectories are shown in the plain strain flow at  $S^* = 5$  (figure 1.18) and in the axisymmetric expansion flow at  $S^* = 15$  (figure 1.19). In figure 1.18 (a), the trajectory obtained with the original LRR-QI model (solid line) starts from the initial condition (?). Then, it violates the rapid PSC-realizability constraint at (Ø) and the RS-realizability at (?). This trajectory is corrected in the truncated model (dash line). It is clearly seen that the trajectory returns to equilibrium after taking a circuitous and fully realizable path. The same is observed on figures 1.18 (b) and 1.19 (a,b). In Figures 1.20 and 1.21 we show various contributions toward the evolution of original and truncated LRR model trajectories. The contributions are shown at two different stages: RS- and rapid PSC-realizability violation states. Initial conditions are same as those in figures 1.18 (b) and 1.19(b).

### 1.7 Summary and Conclusions

A detailed study of Reynolds stress realizability issues is presented in this paper. It is shown that all realizable trajectories asymptote to a unique equilibrium point. The set of anisotropy initial conditions that ultimately lead to Reynolds stress realizability violation (basin-of-violation) is identified for each model (Speziale *et al*, 1991; Launder *et al*, 1975; Shih *et al*, 1985) in different mean flows and at different initial values of  $S^*$ . The basin-of-violation grows with increasing the parameter  $S^*$ . It also depends on the rapid pressure-strain correlation model and the mean flow considered.

Contribution of various terms of the model Reynolds stress equation toward trajectory evolution is studied. The rapid part of the pressure-strain correlation is identified to be the term responsible for the Reynolds stress realizability violation. In this connection, the realizability of a rapid pressure-strain correlation closure is examined, and its direct connection with RS-realizability is established in the first time. Computations demonstrate that violation of the rapid pressure-strain correlation realizability precedes violation of Reynolds stress realizability in all considered cases. Also, Reynolds stress realizability based on either weak or strong formulation does not guarantee the realizable rapid pressure-strain correlation. Thus, realizability constraint (1.4.17) on the rapid

pressure-strain correlation is more fundamental. Such understanding of the turbulence model dynamics is crucial for developing a realizable and physically consistent turbulence model.

Using the rapid pressure-strain correlation realizability constraint (1.4.17), the piece-wise linear model (1.6.4) for the rapid pressure-strain correlation was first suggested in Girimaji (2002) by simply truncating (clipping) the LRR-QI model. Here, by testing the model in different flows, it was confirmed that the truncated LRR model is fully realizable for all initial conditions in the Lumley triangle. In the near future, we will undertake the development of fully realizable and physically superior models based on the new constraints.

## References

- [1] Chou, P.Y. 1945 On velocity correlations and the solution of the equations of turbulent fluctuation. *Quart. Appl. Math.* **3**, 38-54
- [2] Chung M K & Kim S K 1995 A nonlinear return-to-isotropy model with Reynolds number and anisotropy dependency. *Phys. Fluids* **7**, 1425-1436.
- [3] Crow S.C. 1968 Viscoelastic properties of fine-grained incompressible turbulence. *J. Fluid mech.* **33**, 1-20.
- [4] Durbin, P.A. & Speziale, C.G. 1994 Realizability of second-moment closures via stochastic analysis. *J. Fluid Mech.* **280**, 395-407.
- [5] Fu S, Lunder B E & Tselepidakis D P 1987 Accommodating the effects of high strain rates in modeling the pressure-strain correlation. *Technical Report* TFD/87/5, Mech. Engg. Dept, UMIST.
- [6] Girimaji, S.S. 1996 Fully explicit and self-consistent algebraic Reynolds stress model. *Theoret. Comput. Fluid Dynamics* **8**, 387-402
- [7] Girimaji, S.S. 2000 Pressure-strain correlation modeling of complex turbulent flows. *J. Fluid Mech.* **422**, 91-123.
- [8] Girimaji, S.S. 2002 New perspective on realizability of turbulence models *J. Fluid Mech.* (Submitted for publication)
- [8] Girimaji, S.S. Jeong, E., & Poroseva, S. 2003 Pressure-strain correlation in homogeneous anisotropic turbulence subject to rapid strain-dominated distortion. To appear in *Phys. Fluids*.
- [9] Johansson, A.V. & Hallback, M. 1994 Modeling of rapid pressure-strain in Reynolds stress closures. *J. Fluid Mech.* **269**, 143.
- [10] Jones, W.P. & Musonge, P. 1988 Closure of Reynolds stress and scalar flux equations. *Phys. Fluids*. **31**, 3589-3604.
- [11] Kassinos, S.C., Reynolds, W.C., & Rogers, M.M. 2001 One-point turbulence structure tensors. *J. Fluid Mech.* **428**, 213-248.
- [12] Launder, B.E., Reece, G.J., & Rodi, W. 1975 Progress in the development of a Reynolds stress turbulence closure. *J. Fluid Mech.* **58**, 537-566.
- [13] Lumley, J.L. 1978 Computational modeling of turbulent flows. *Adv. App. Mech.* **18**, 123-176.
- [14] Pope S B 1985 PDF methods for turbulent reactive flows *Prog. Energy Combust. Sci.* **11**, 119-192.
- [15] Pope, S.B. 2000 Turbulent Flows. Cambridge University Press. London.
- [16] Reynolds, W.C. 1976 Computation of turbulent flows. *Ann. Rev. Fluid Mech.* **8**, 183-208.

- [17] Ristorcelli, J.R., Lumley, J.L. & Abid, R. 1995 A rapid pressure covariance representation consistent with the Taylor-Proudman theorem and materially frame indifferent in the 2-D limit *J. Fluid Mech.* **292**, 111-152.
- [18] Rotta J C 1951 Statistische theorie nichthomogener turbulentz 1. *Z. Phys.* **129** 547-572.
- [19] Sarkar S & Speziale C G 1990 A simple nonlinear model for return to isotropy in turbulence. *Phys. Fluids A* **2**, 84-93.
- [20] Schumann, U. 1977 Realizability of Reynolds stress turbulence models. *Phys. Fluids* **20**, 721-725.
- [21] Shih, T.H., Lumley, J.L. 1985 Modeling of pressure correlation terms in Reynolds stress and scalar flux equations. *Rep. FDA 85-3*, Sibley School of Mechanical and Aerospace Engineering, Cornell University, Itacha, NY, USA.
- [22] Sjogren, T. & Johansson, A.V. 2000 Development and calibration of algebraic non-linear models for terms in the Reynolds stress transport equation *Phys. Fluids*. **12**, No.6, 1554-1572.
- [23] Speziale, C.G., Sarkar, S. & Gatski, T.B. 1991 Modeling pressure-strain correlation in turbulence: A dynamic invariant approach. *J. Fluid Mech.* **227**, 245-272.

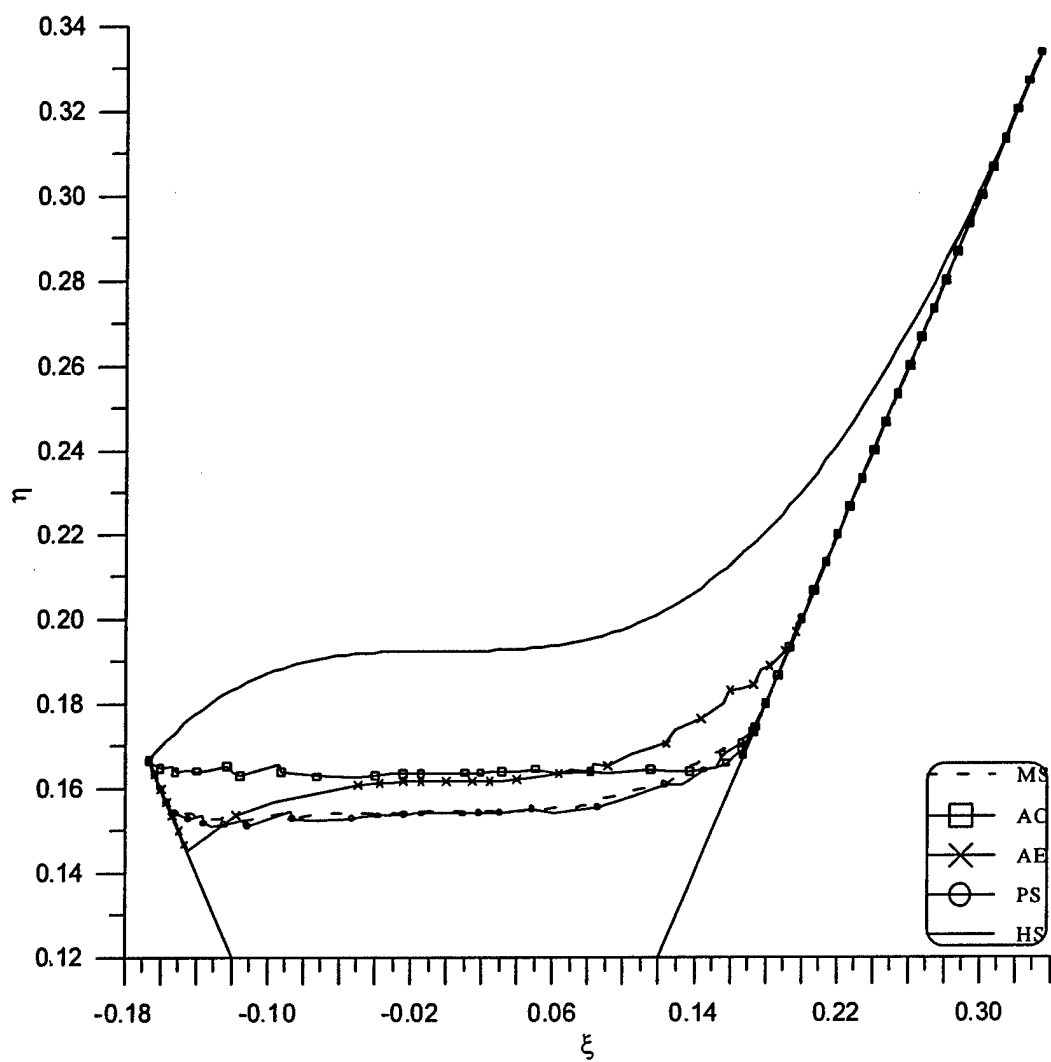


**Figure 1.1** Violation boundaries for LRR-QI model in different flows at  $S^* = 5$ .

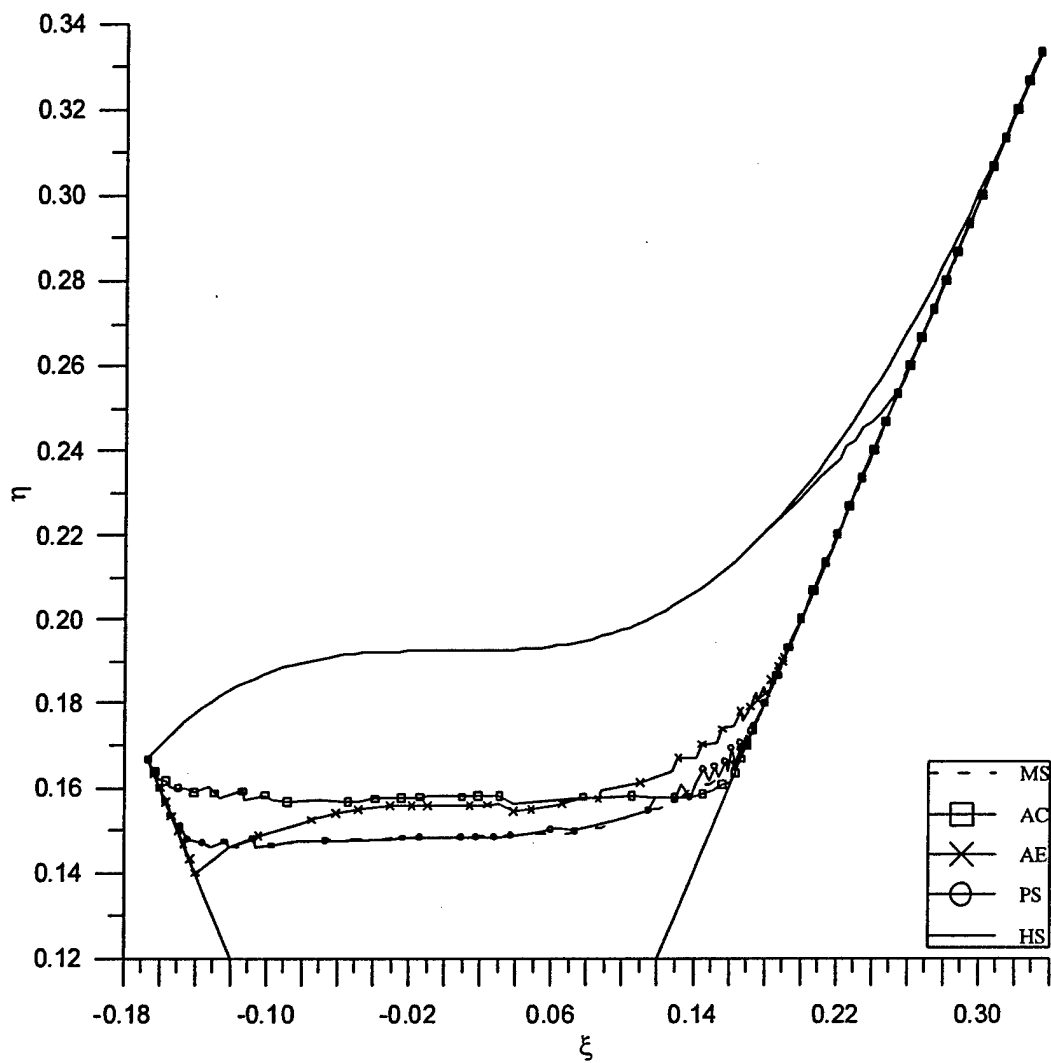


**Figure 1.2** Violation boundaries for LRR-QI model in different flows at  $S^* = 50$ .



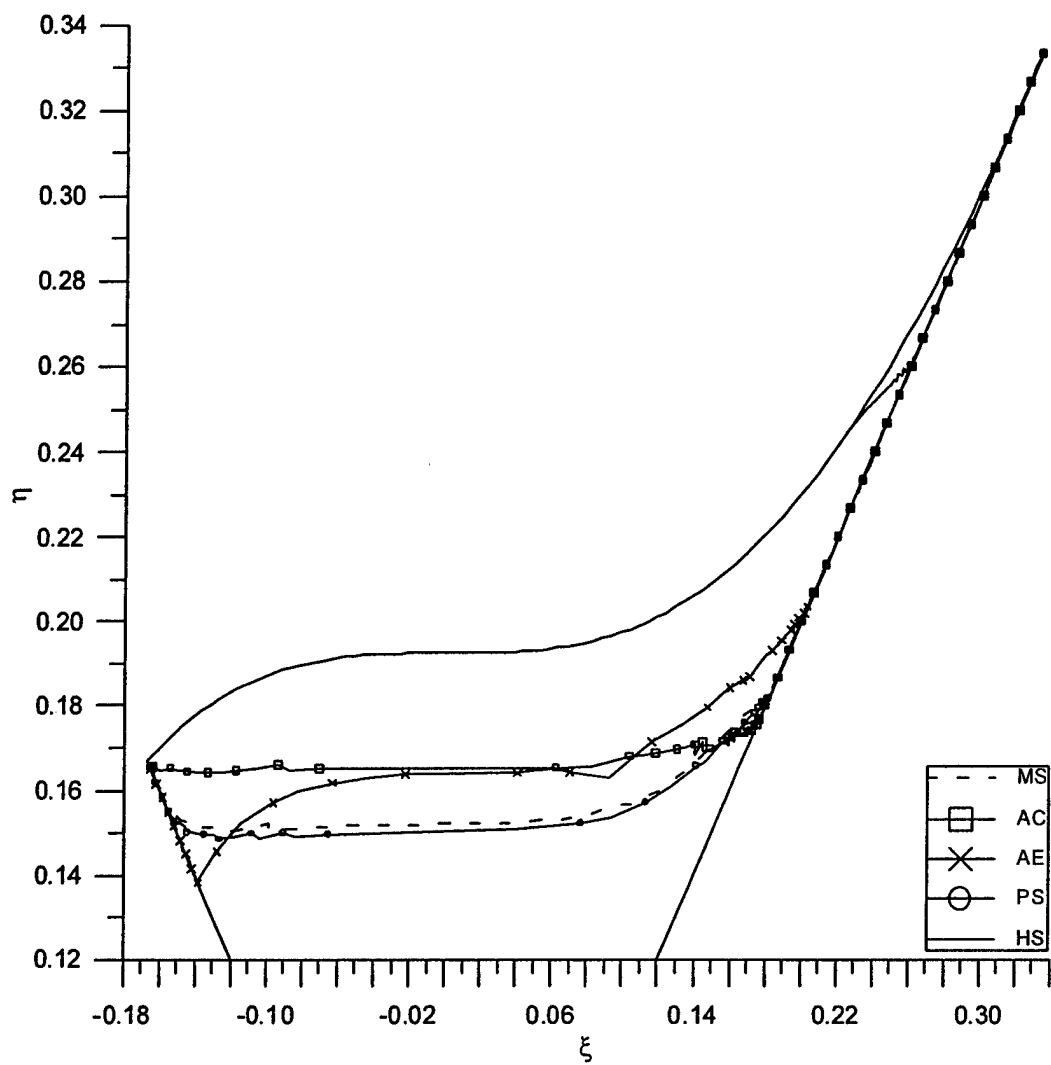


**Figure 1.3** Violation boundaries for SSG model in different flows at  $S^* = 5$ .

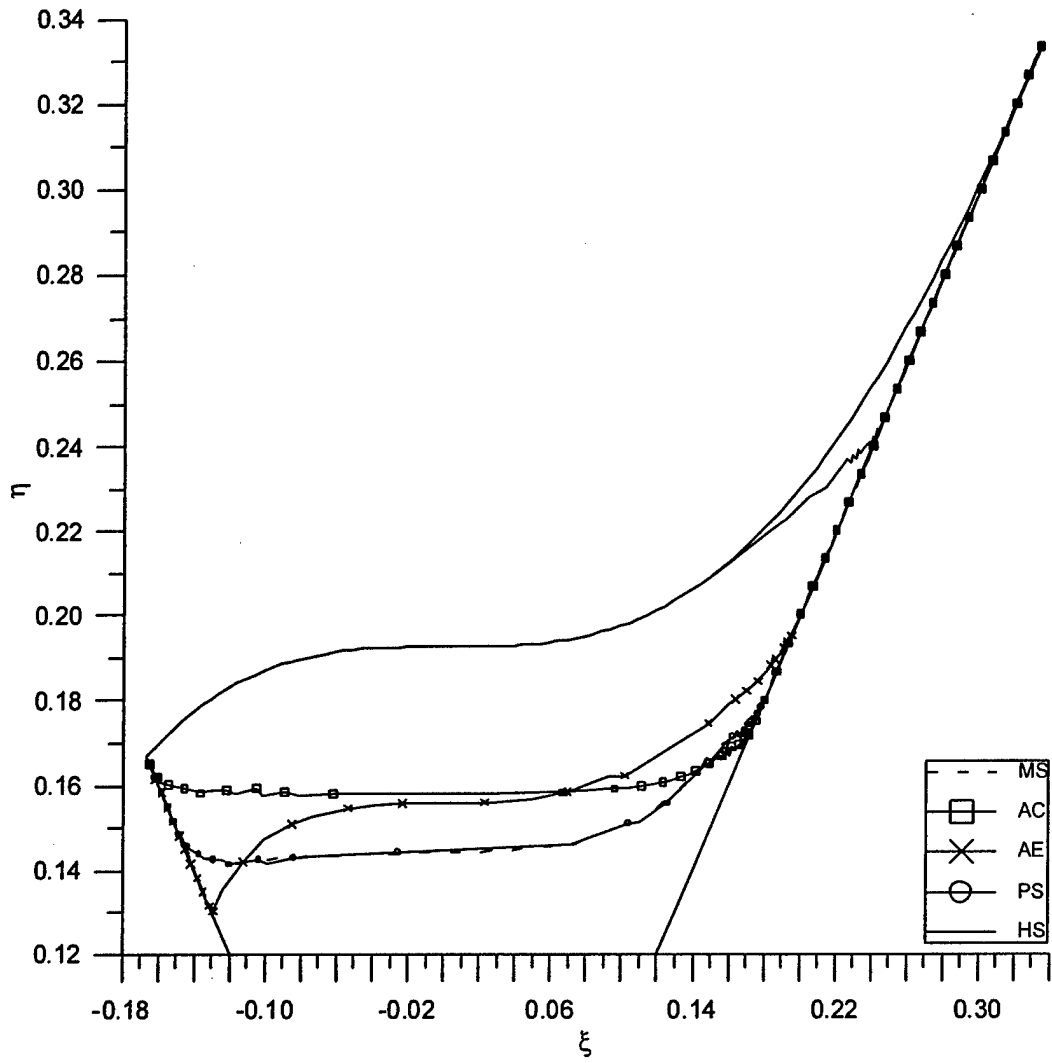


**Figure 1.4** Violation boundaries for SSG model in different flows at  $S^* = 50$ .

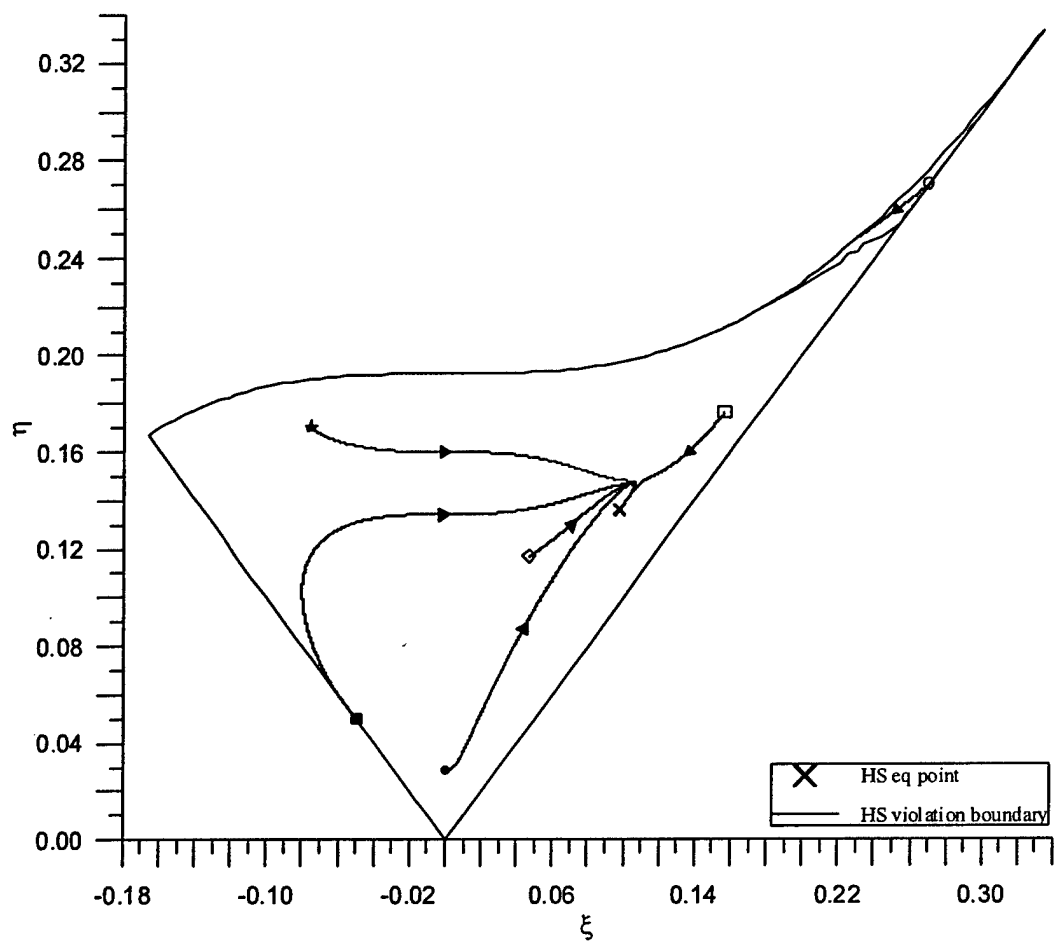


**Figure 1.5** Selected trajectories ( $\odot$ ,  $\otimes$ ,  $\square$ ,  $\blacksquare$ ,  $\triangle$ , and  $\blacktriangle$ ) in HS flow calculated with the LRR-QI model at  $S^* = 50$

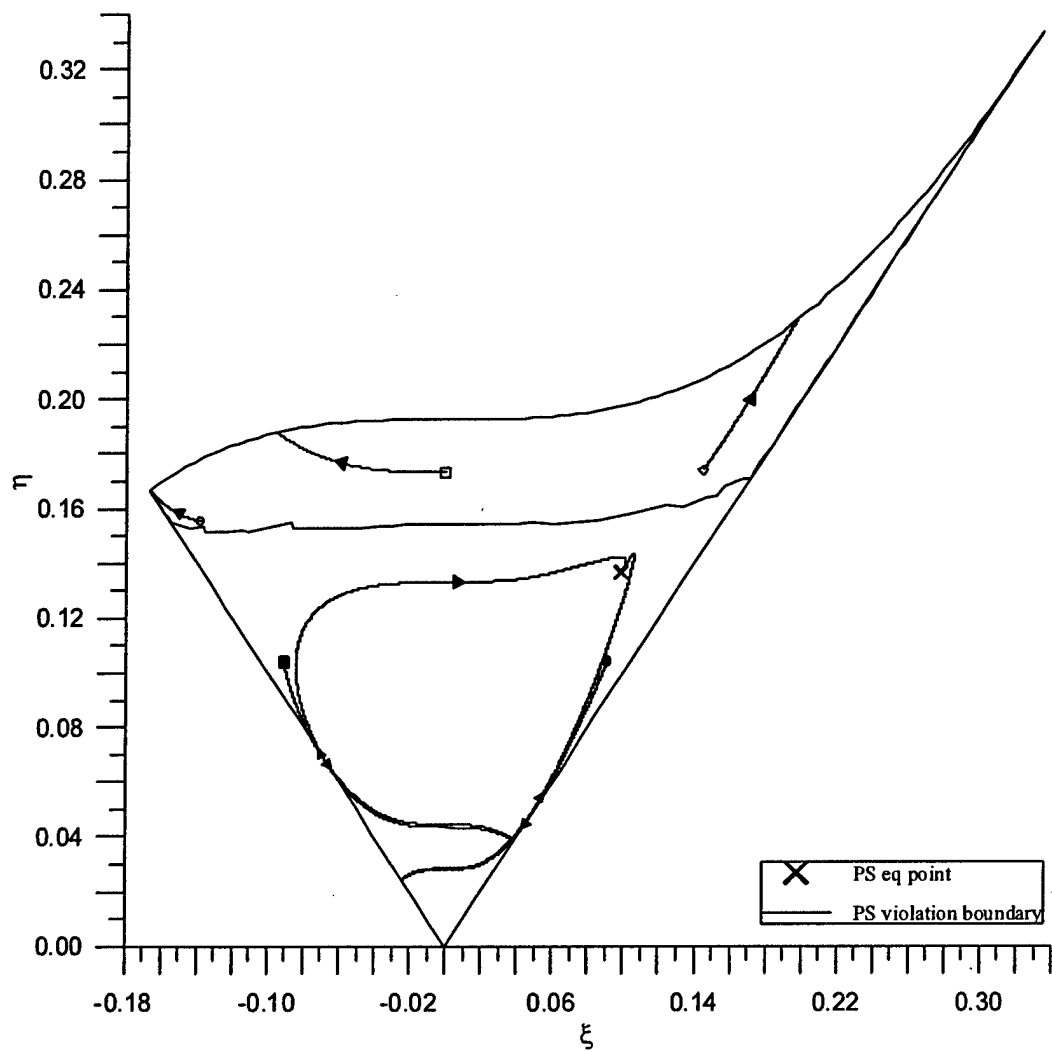


**Figure 1.6** Selected trajectories ( $\odot$ ,  $\boxtimes$ ,  $\blacktriangle$ ,  $\diamond$ , and  $\oplus$ ) in PS flow calculated with the LRR-QI model at  $S^* = 5$ .

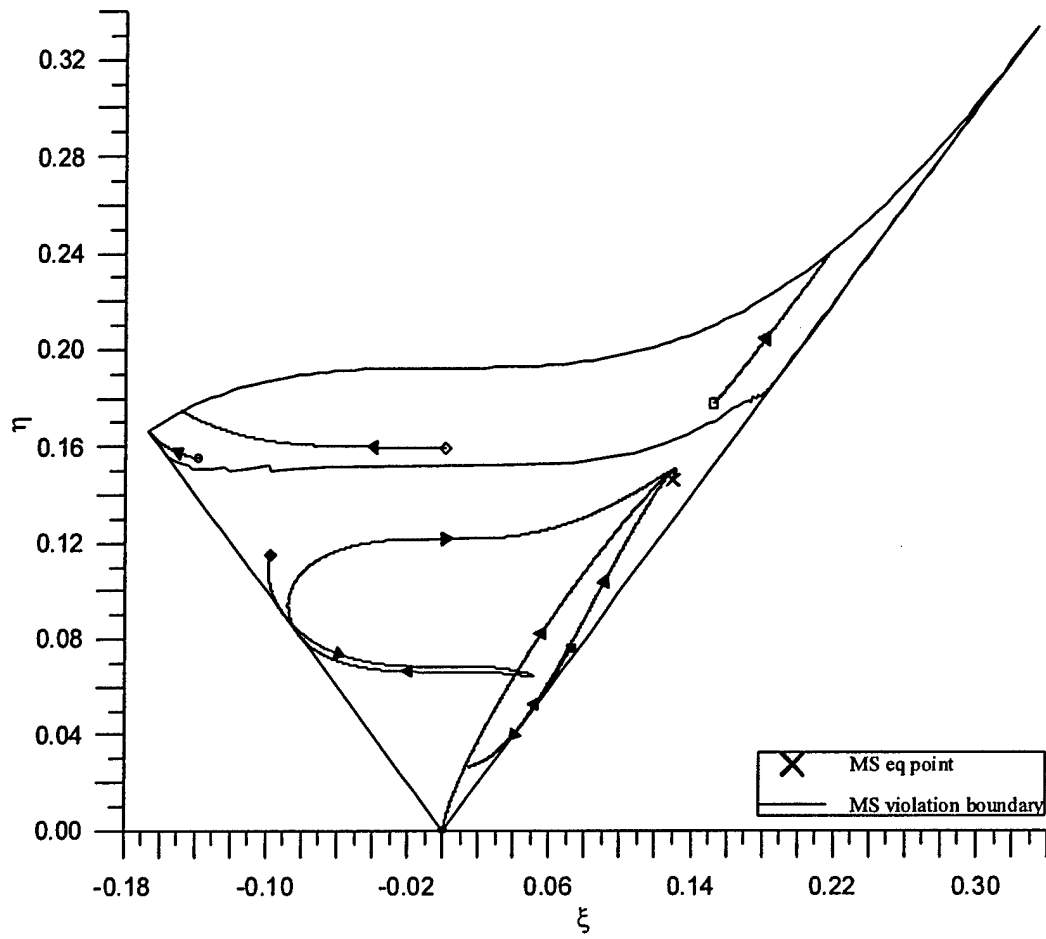


**Figure 1.7** Selected trajectories ( $\odot$ ,  $\boxtimes$ ,  $\diamond$ ,  $\triangle$ ,  $\times$ , and  $\oplus$ ) in MS flow calculated with the SSG model at  $S^* = 5$ .

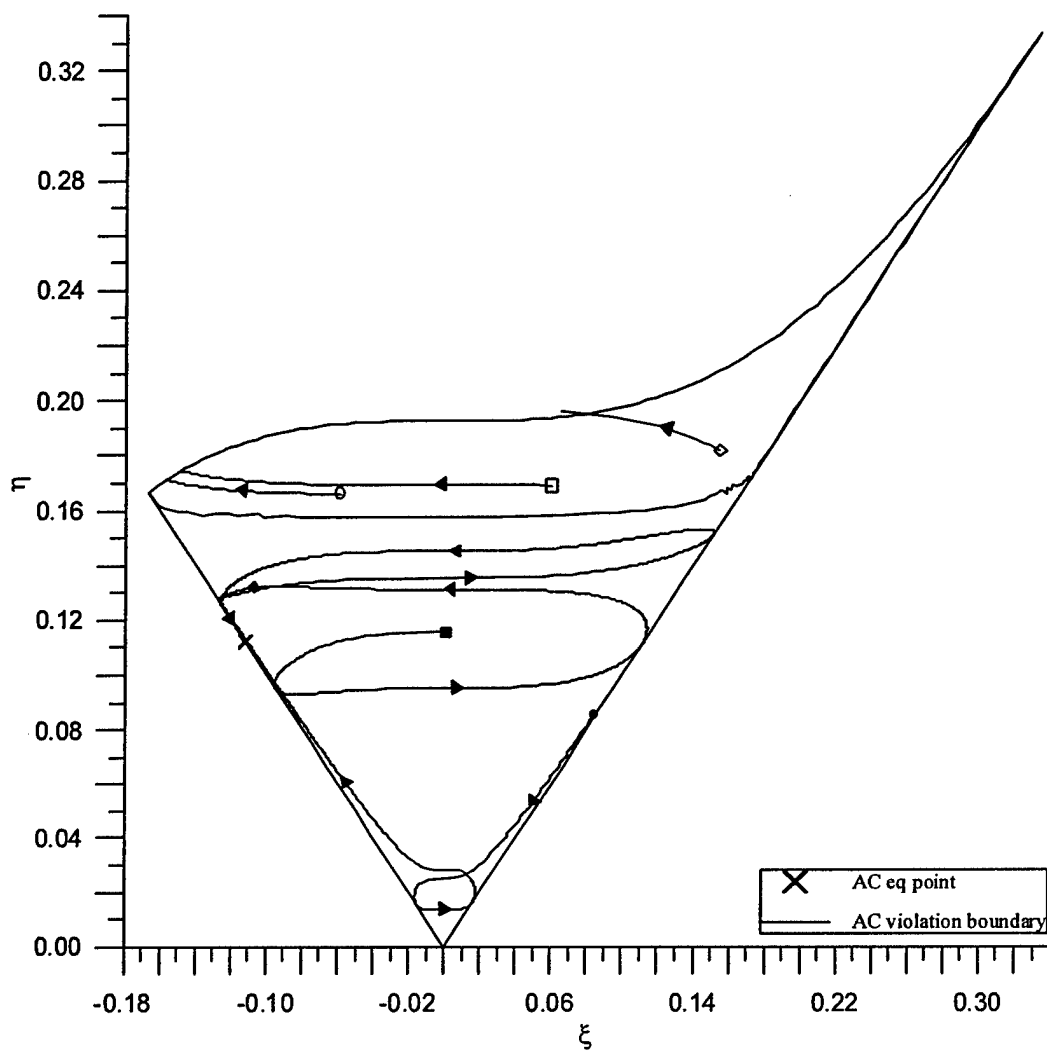


**Figure 1.8** Selected trajectories ( $\odot$ ,  $\boxtimes$ ,  $\boxplus$ ,  $\boxminus$ ,  $\times$ , and  $\bullet$ ) in AC flow calculated with the SSG model at  $S^* = 50$ .

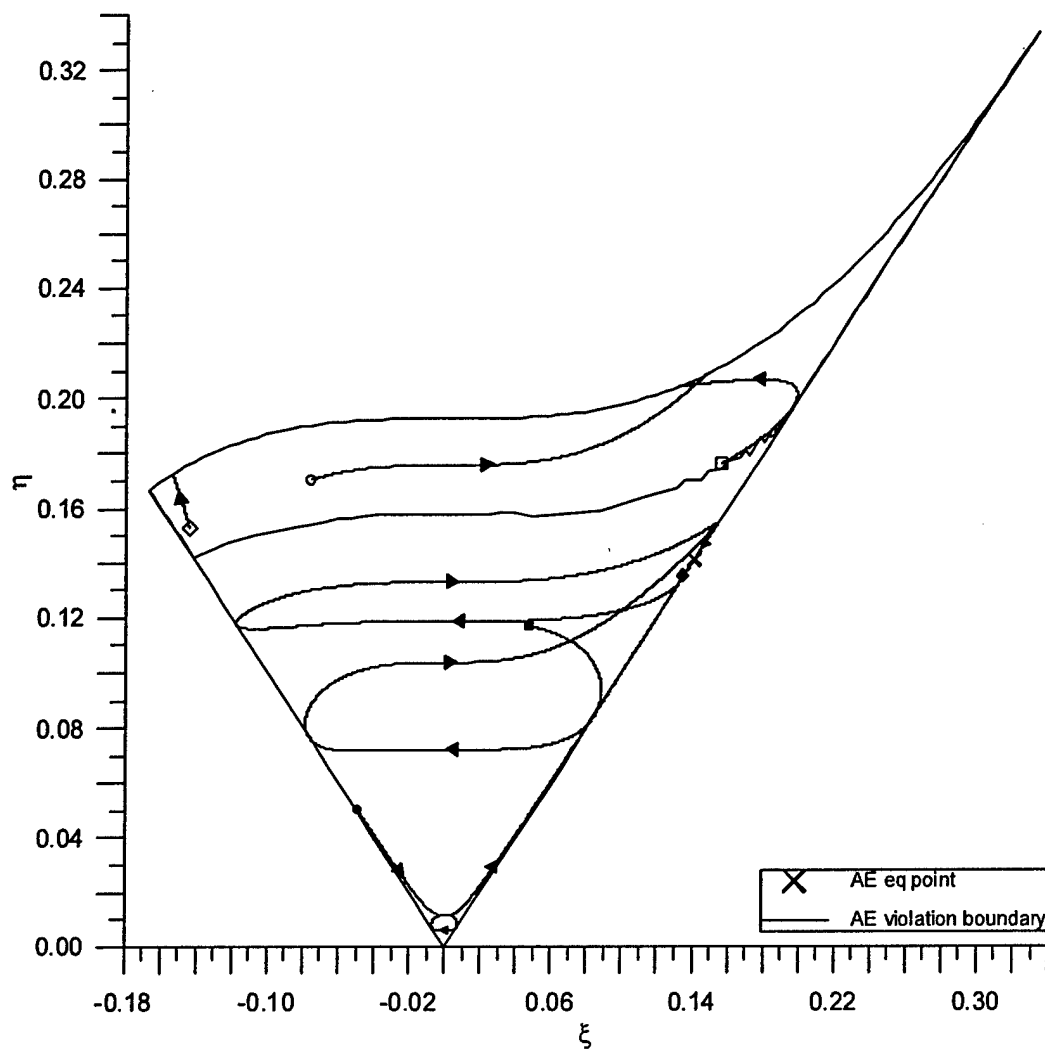


**Figure 1.9** Selected trajectories ( $\odot$ ,  $\boxtimes$ ,  $\ominus$ ,  $\boxdot$ ,  $\blacktriangle$ , and  $\bullet$ ) in AE flow calculated with the LRR-QI model at  $S^* = 15$ .

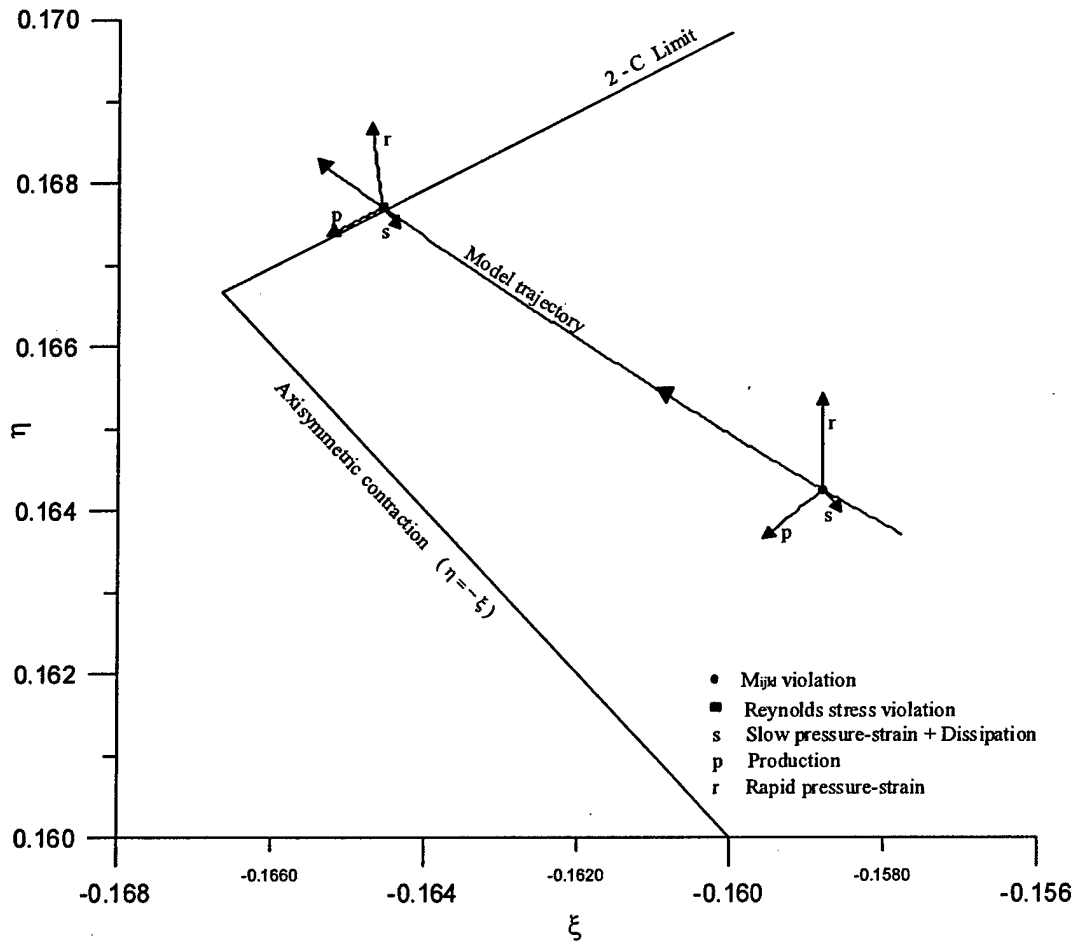


**Figure 1.10** Contribution of three parts of the Reynolds stress equation in trajectory evolution shown at stages of  $M_{ijk}$  and RS violations. Case: PS flow at  $S^*=5$ ; LRR-QI model describes rapid pressure strain correlation.



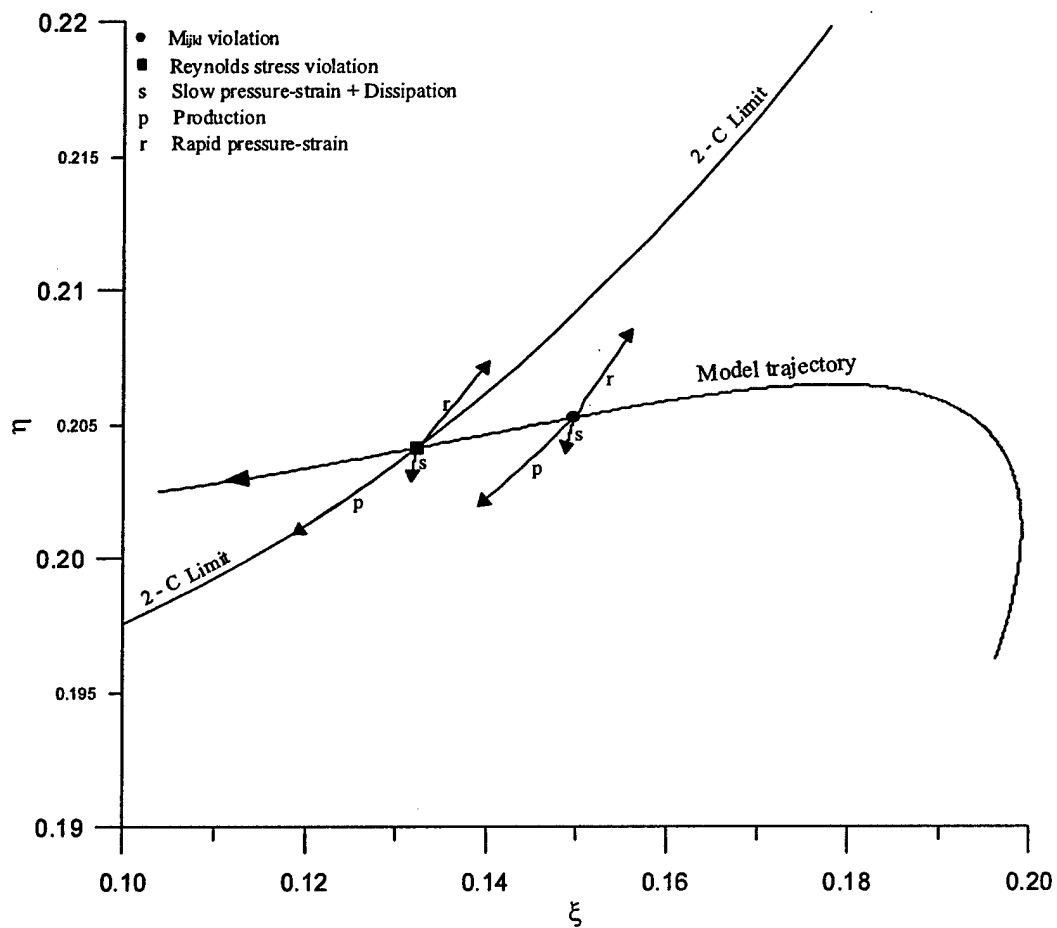


**Figure 1.11** Contribution of three parts of the Reynolds stress equation in trajectory evolution shown at stages of  $M_{ijk}$  and RS violations. Case: AE flow at  $S^*=15$ ; LRR-QI model describes rapid pressure strain correlation.

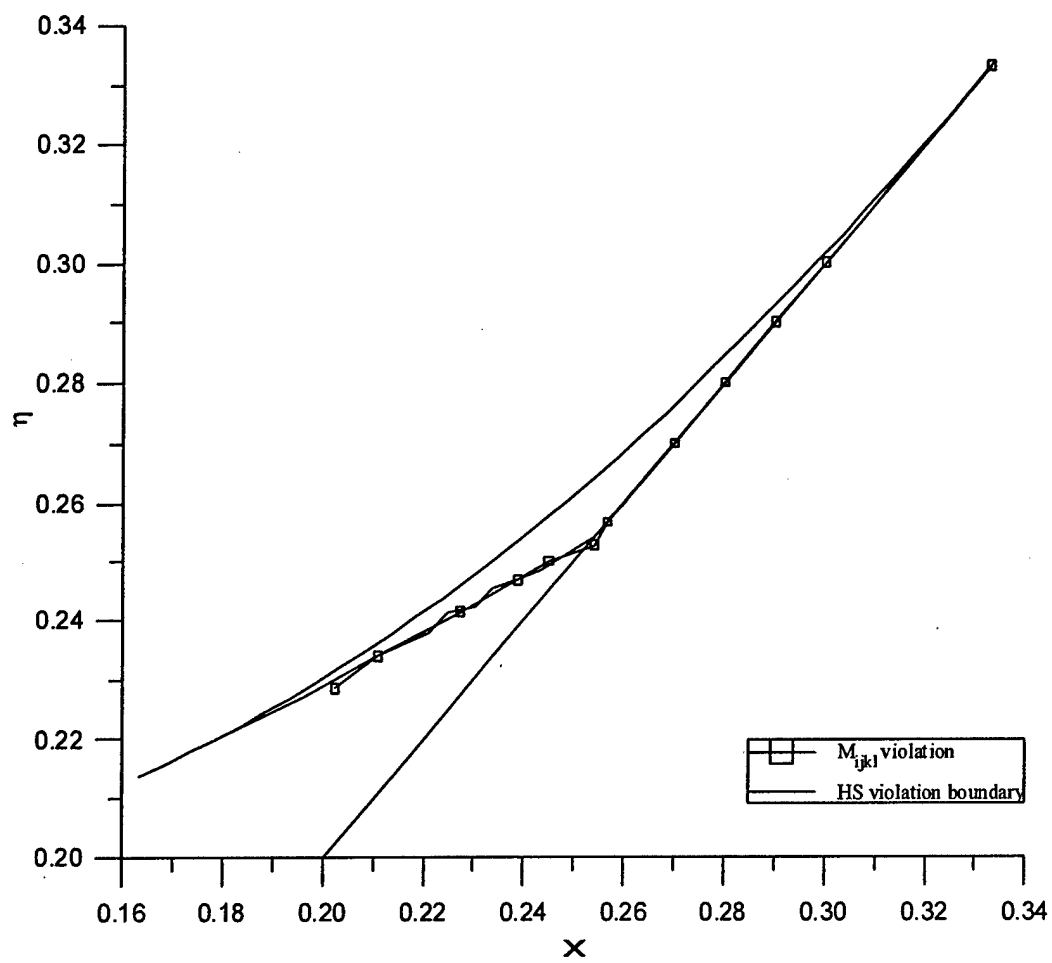


**Figure 1.12** The  $M_{ijkl}$ -violation boundary (symbols) for the LRR-QI model in HS flow at  $S^* = 50$ .

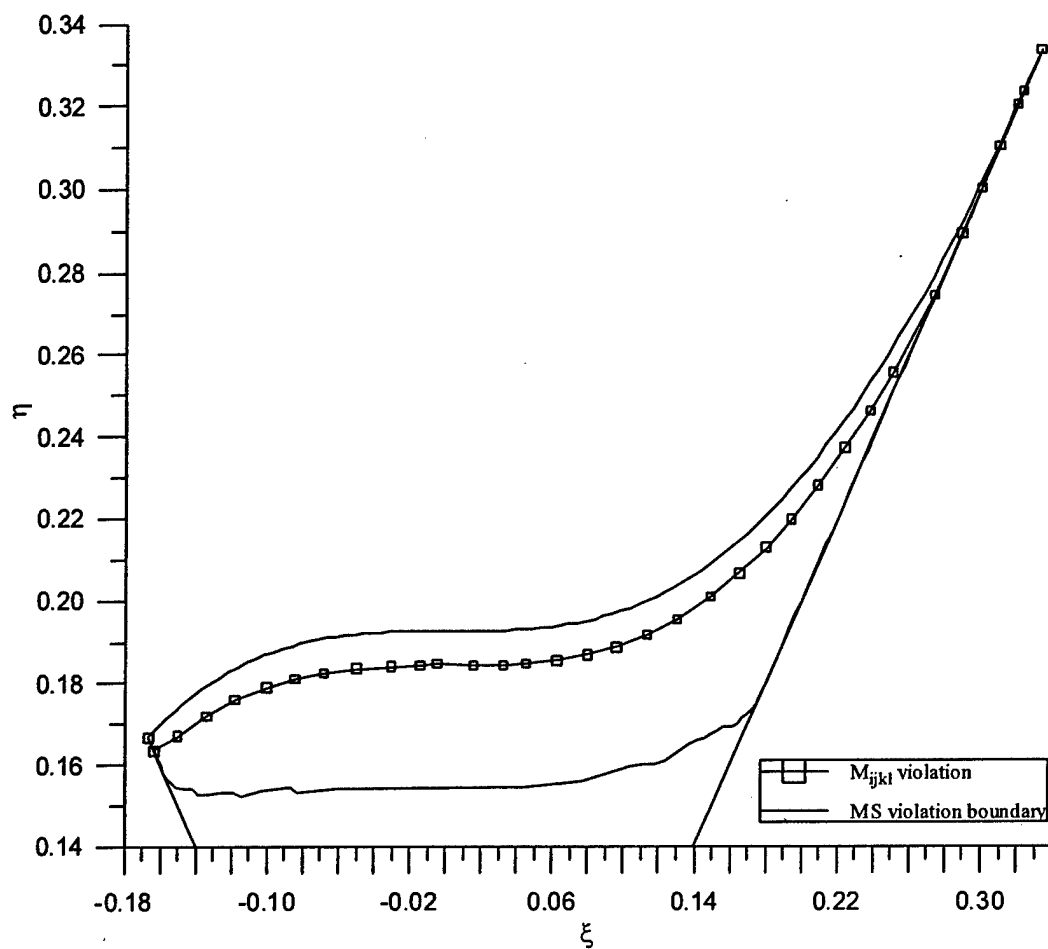


**Figure 1.13** The  $M_{ijkl}$ -violation boundary (symbols) for the LRR-QI model in MS flow at  $S^* = 5$ .

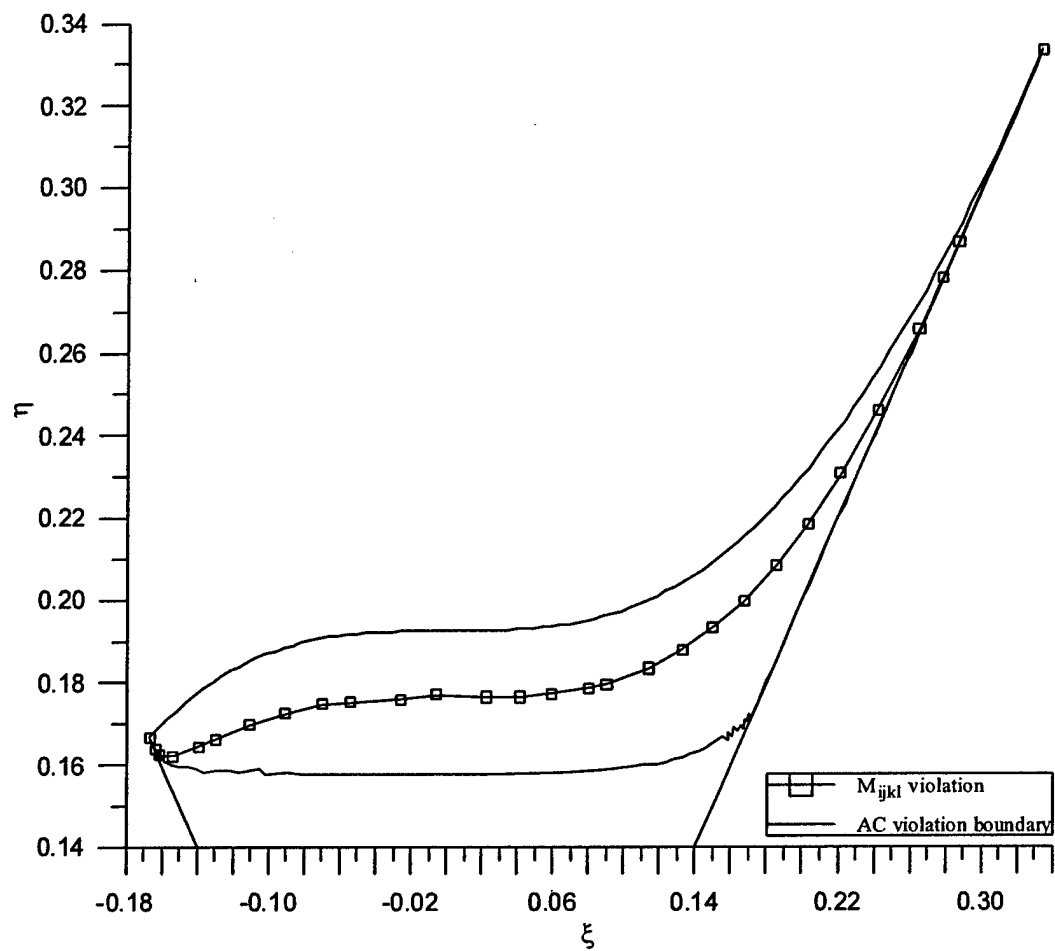


**Figure 1.14** The  $M_{ijkl}$ -violation boundary (symbols) for the SSG model in AC flow at  $S^* = 50$ .

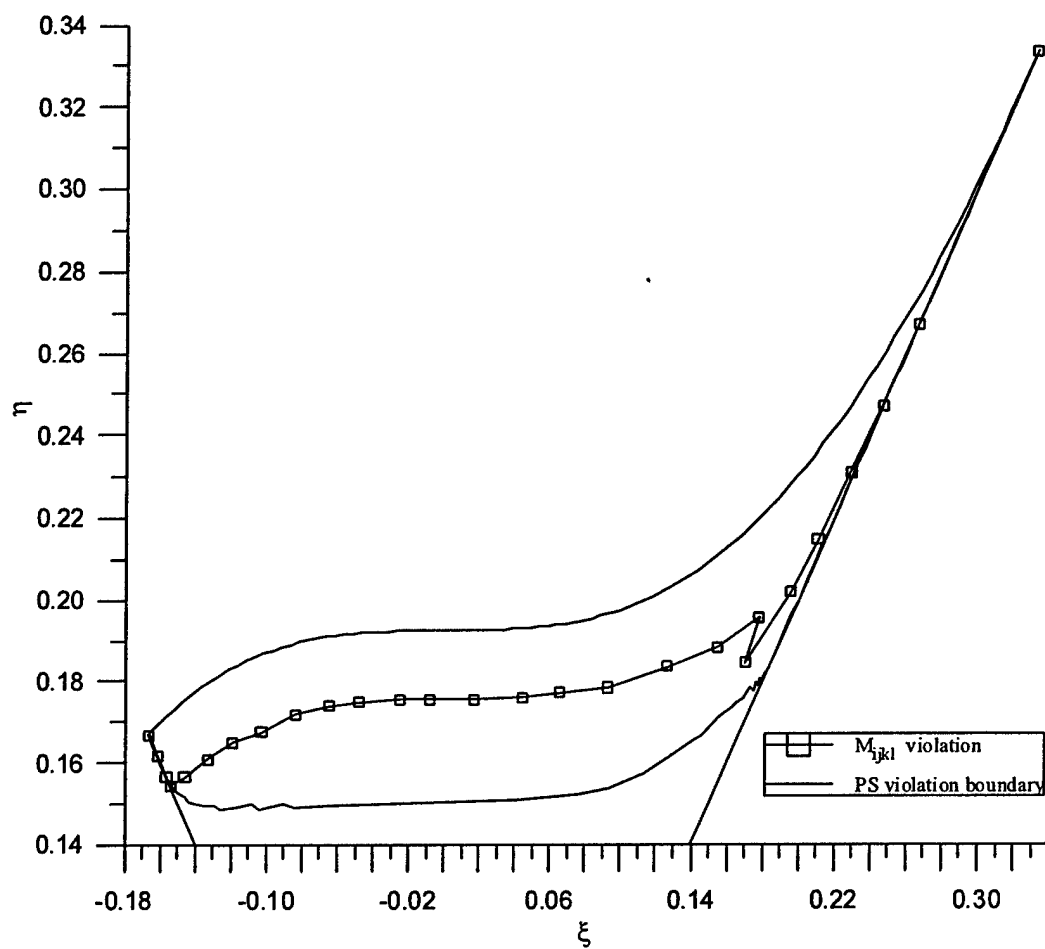


**Figure 1.15** The  $M_{ijkl}$ -violation boundary (symbols) for the SSG model in PS flow at  $S^* = 5$ .

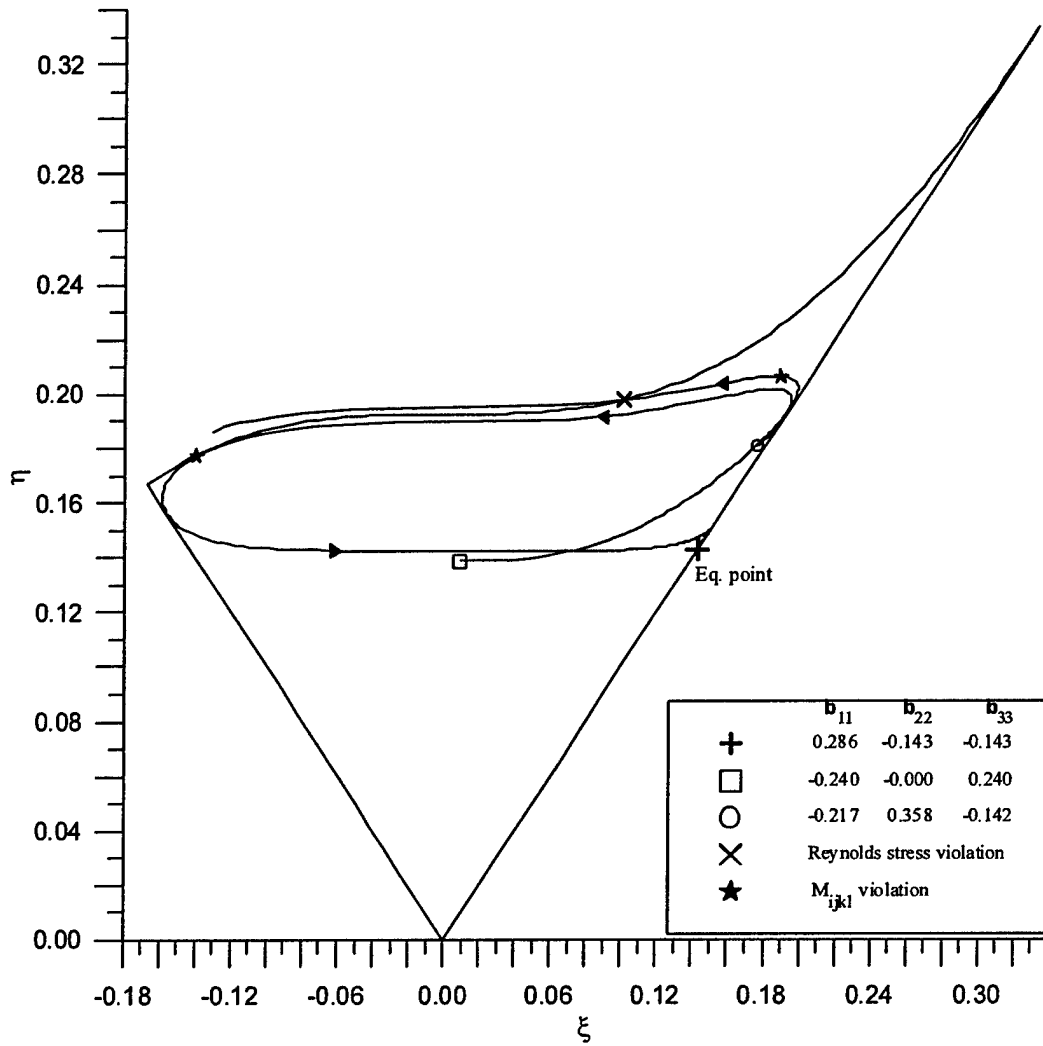


**Figure 1.16** Selected trajectories calculated with the LRR-QI model in AE flow at  $S^* = 50$ .  
**Denotations:** (+, □) initial conditions, (X) equilibrium point, (○) locations of the  $M_{ijkl}$ -constraint violation, (⊗) RS-realizability violation point.

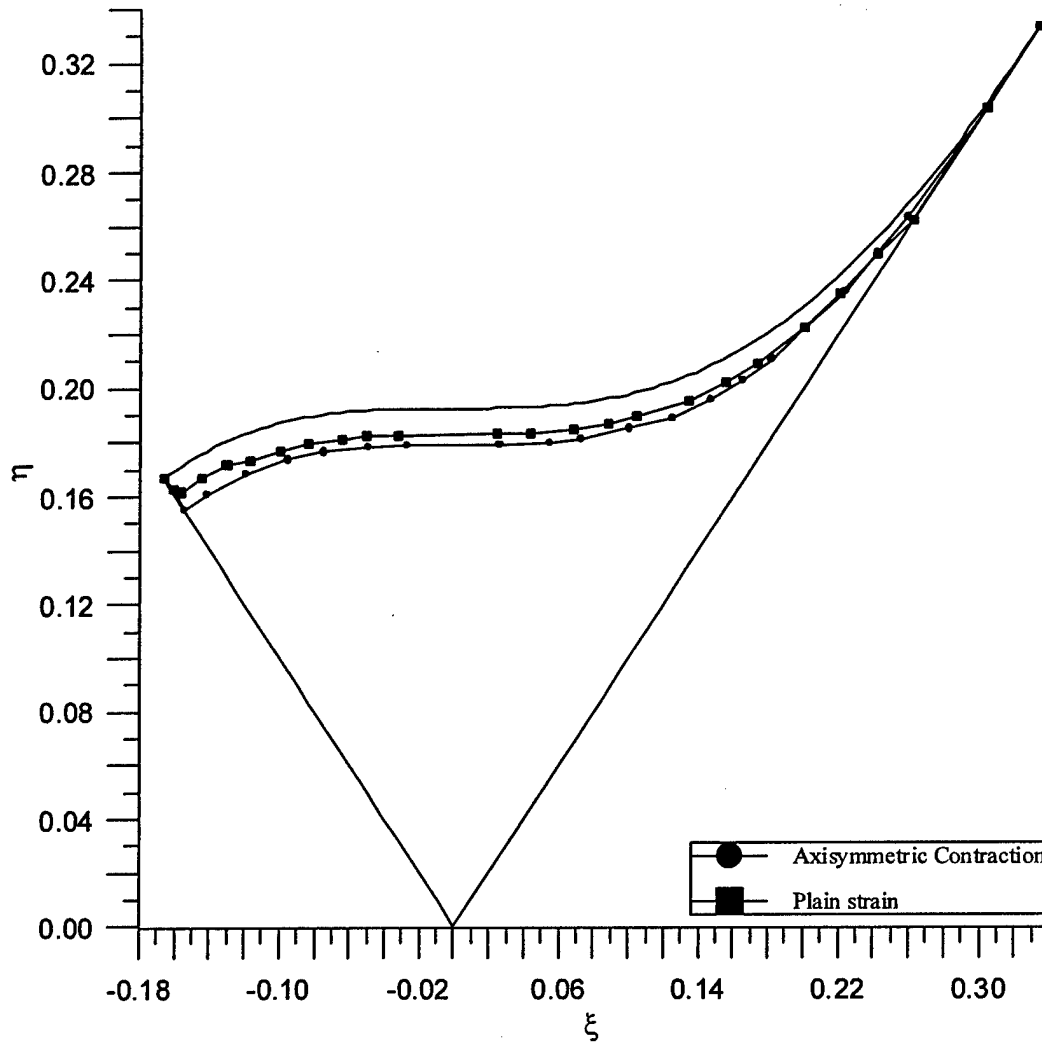


**Figure 1.17**  $M_{ijkl}$ -violation boundaries for the SL model in PS and AC flows at  $S^* = 5$ .

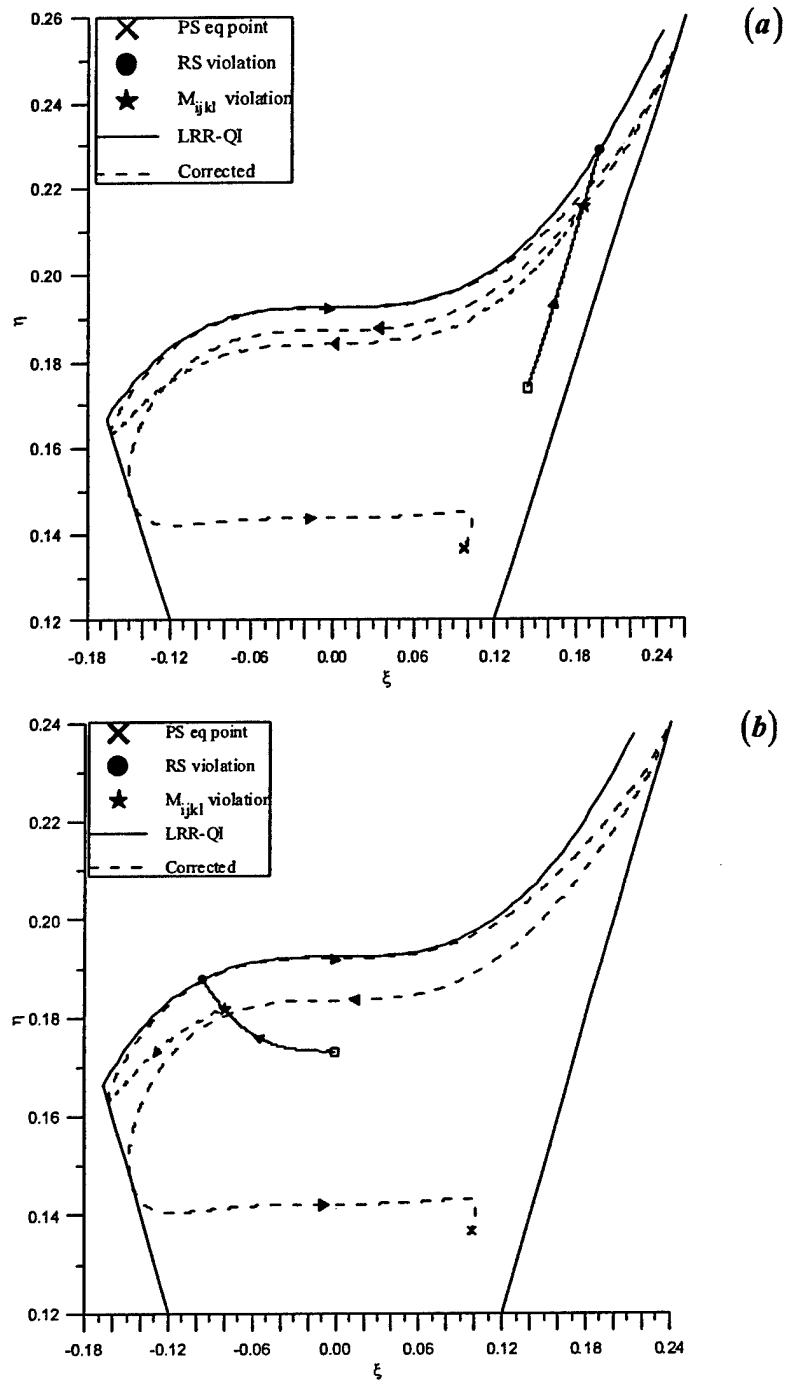


**Figure 1.18** Trajectories obtained with the original LRR-QI model (—) and truncated LRR model (---) for two initial conditions (a) and (b) in PS flow at  $S^* = 5$ .



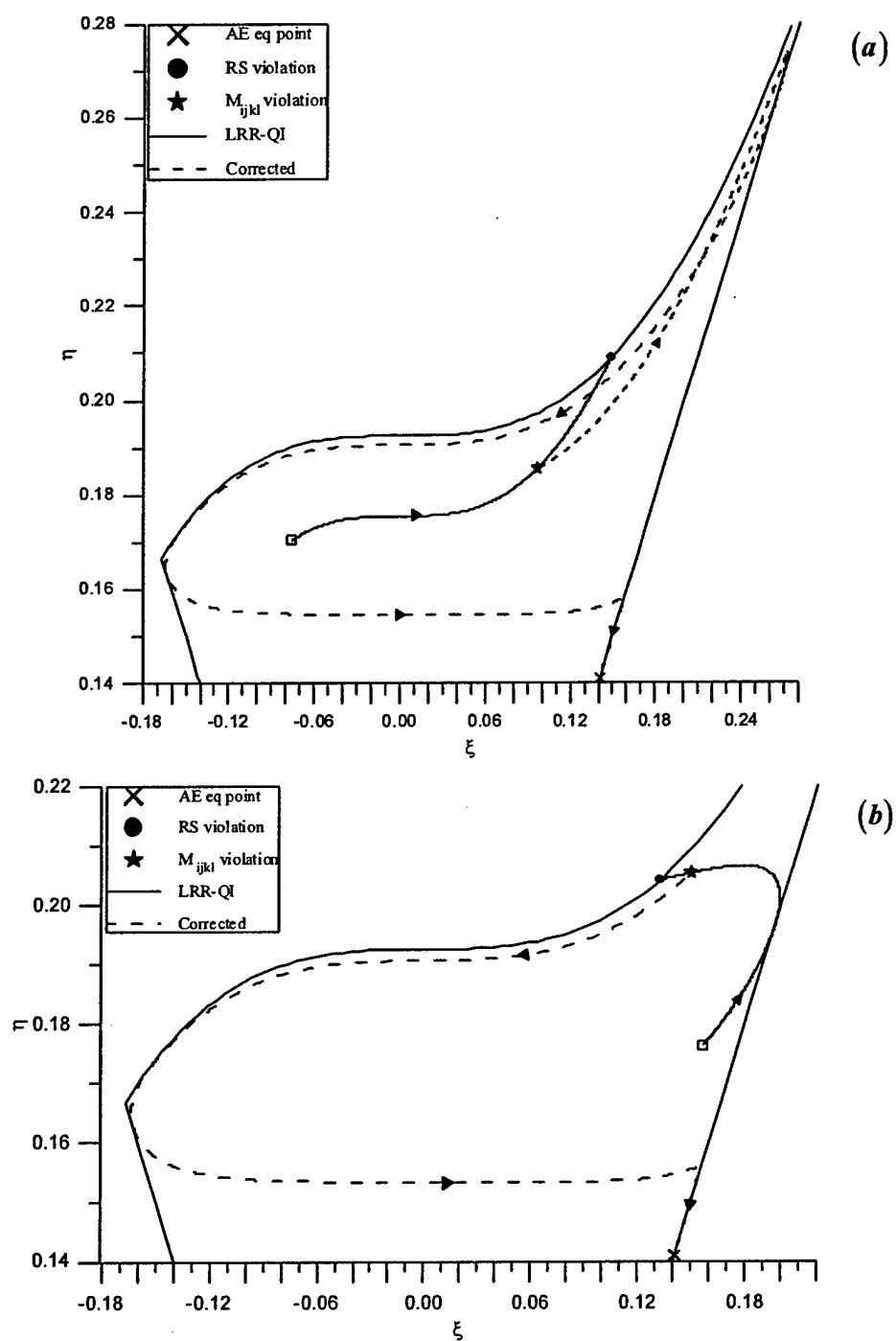


**Figure 1.19** Trajectories obtained with the original LRR-QI model (—) and truncated LRR model (---) for two initial conditions (a) and (b) in AE flow at  $S^* = 15$ .

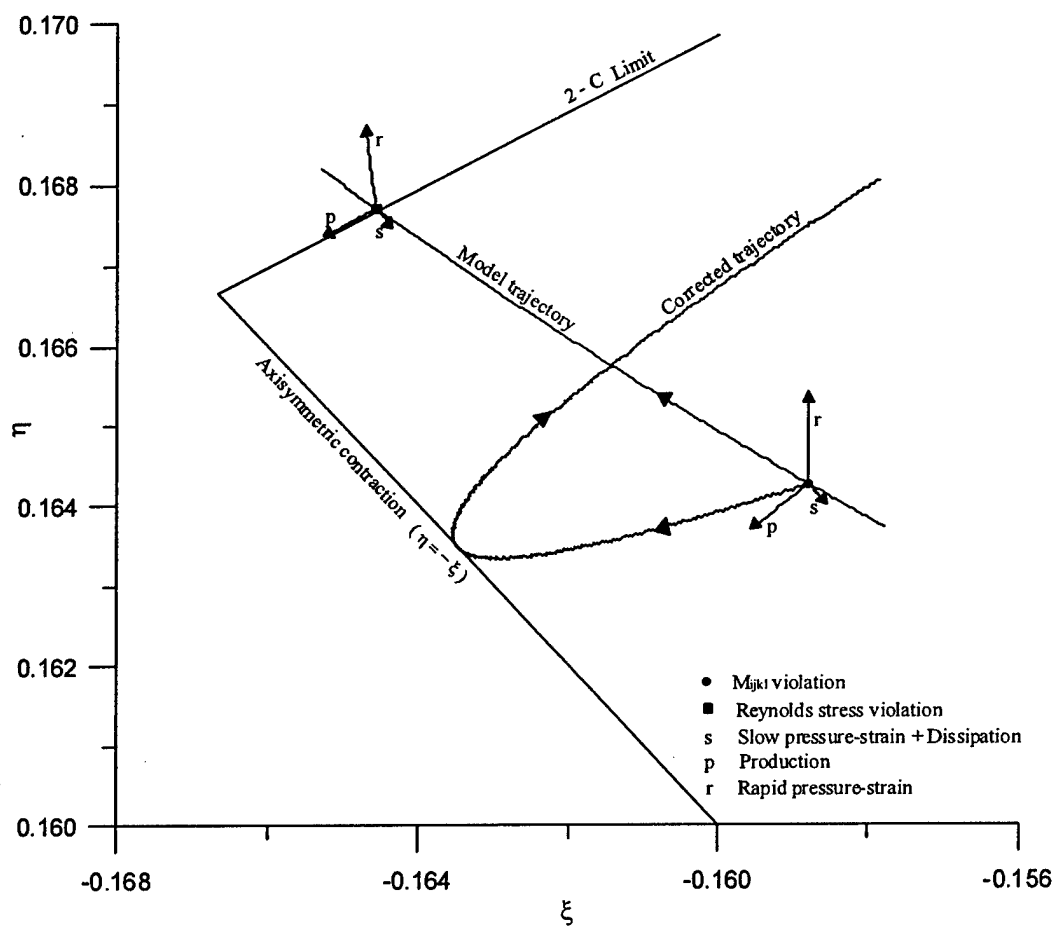


**Figure 1.20** Contribution of three parts of the Reynolds stress equation in evolution of original and corrected LRR trajectories shown at stages of  $M_{ijkl}$  and RS violations. Case: PS flow at  $S^*=5$ .

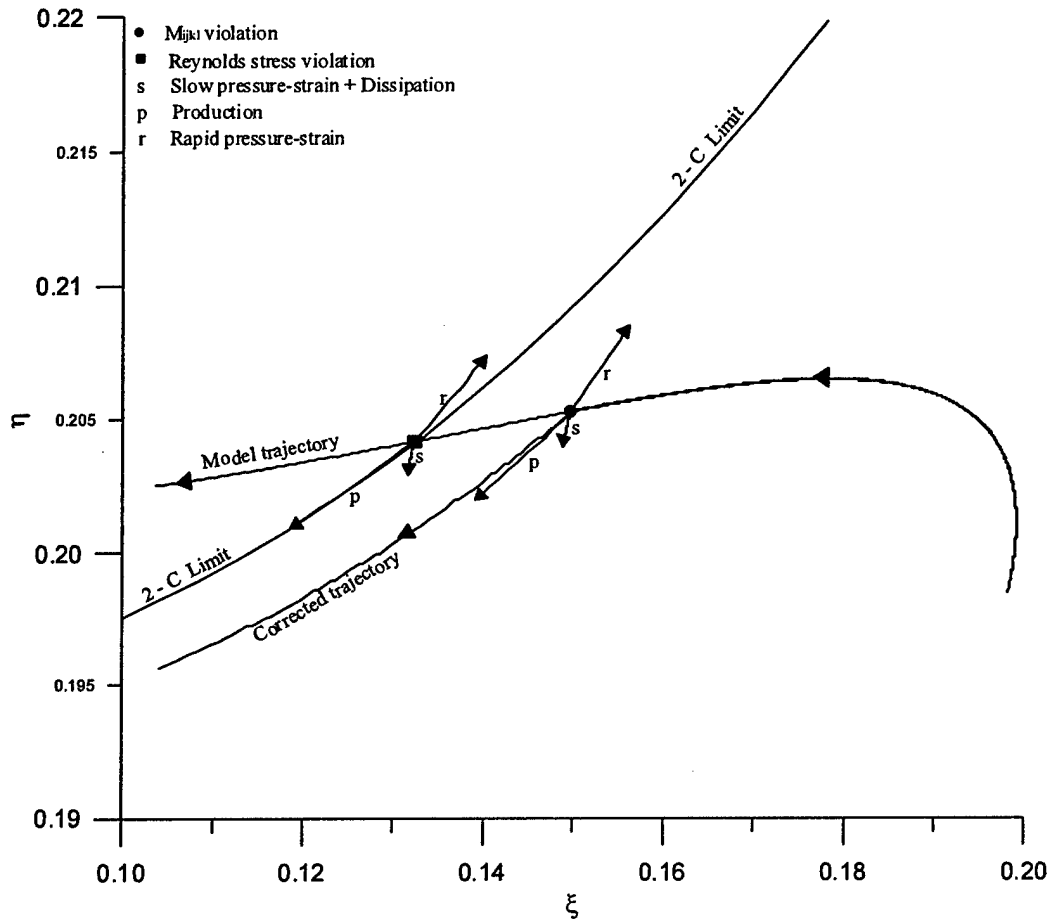


**Figure 1.21** Contribution of three parts of the Reynolds stress equation in evolution of original and corrected LRR trajectories shown at stages of  $M_{ijkl}$  and RS violations. Case: AE flow at  $S^* = 15$ .

---

## Chapter 2 Pressure-Strain Correlation in Homogeneous Anisotropic Turbulence Subjected to Rapid Strain-Dominated Distortion

---

### 2.1 INTRODUCTION

Accurate modeling of the pressure-strain correlation continues to be one of the important challenges in the second-moment closure method of turbulence modeling. In particular, the "rapid" portion of the pressure-strain correlation has been the subject of many analytical and modeling studies.

When turbulence is subjected to rapid distortion (RD), the description of turbulence evolution simplifies significantly leading to the so-called rapid-distortion theory (RDT) equations which are linear in fluctuating velocity. In this limit, the physics of rapid pressure-strain correlation can be studied in relative isolation as the complicating effects of slow pressure-strain correlation and dissipation are absent. Another important feature of this limit is that the fluid behaves as an elastic rather than a viscous medium. The stresses and other turbulence properties including the pressure-strain correlation depend on the total strain (deformation) experienced by the fluid element rather than the current strain rate. Beyond this, our understanding of the behavior of initially anisotropic turbulence subject to rapid distortion is relatively poor as much of the previous RD studies have focused on initially isotropic turbulence.

The focus of this work is on physics of pressure-strain correlation in homogeneous anisotropic turbulence subject to rapid strain-dominated distortion. Specifically, we study extreme cases of initial turbulence anisotropy: two-component (2C) and one-component (1C) turbulence, along with isotropic turbulence. This choice is motivated by the argument that if rapidly-distorted turbulence behavior can be well understood and modeled at the three extremes of the Lumley invariant triangle map<sup>7</sup>, the behavior at any arbitrary level of anisotropy can be inferred by suitable interpolation. Several types of strain-dominated rapid deformation: homogeneous shear (HS), plain strain (PS), axisymmetric contraction (AC), and axisymmetric expansion (AE), are considered in this study. Once, some degree of understanding of the rapid pressure-strain correlation physics is developed, we will attempt to extract some general guidelines to aid in future model developments.

Rotation-dominated (elliptic flows) mean flows and flow in rotating frames are examined in a separate study as the behavior of these flows in the RD limit is significantly different from that of strain-dominated flows.

#### *Modeling Issues*

The rapid pressure-strain correlation, in general, depends on the velocity spectrum tensor and, hence, cannot be a unique function of Reynolds stresses and mean velocity gradients<sup>8</sup>. In the RDT calculations (multi-point closure) pressure-strain correlations appears in closed form as the velocity spectrum is fully known. To accurately describe pressure-strain correlation at the one-point closure level, at a minimum two independent turbulence field tensors - componentiality (C) and dimensionality (D) -- are needed<sup>15, 13</sup>. *Componentiality* refers to the number of non-zero

diagonal components in the Reynolds stress tensor, whereas *dimensionality* is a statement about the wavenumber vector: it refers to the number of orthogonal directions in which wave numbers are permitted<sup>13</sup>. Pressure-strain correlation can possibly take a large range of values for a given combination of Reynolds stresses and mean velocity field, depending on the dimensionality tensor<sup>15</sup>. In the traditional second moment closure (SMC) approach, this all important dimensionality tensor is not known. Without the knowledge of dimensionality tensor, the pressure-strain correlation closure problem is not well-posed as the solution is not unique. The challenge of traditional one-point closure modeling is to select a single appropriate value within the range of allowable values for the pressure-strain correlation.

Given this limitation, no single one-point closure model can simulate the entire range of physics incumbent in the RDT equations. The best that can be expected of any traditional one-point closure model is that it captures the most fundamental features of the RDT equations. As a result, in one-point closure modeling, many of the pathological aspects of the RDT behavior will have to be excluded in favor of the more dominant features. In this paper, we will focus only on modeling issues pertaining to realizability and fundamental consistency with rapid distortion theory.

Our goal is, rather, to develop modeling constraints that go beyond the Crow constraint and enjoy a wider range of validity and applicability in rapidly distorted turbulence.

Simple analysis shows that pressure-strain correlation can be written as following<sup>1</sup> in rapidly distorted isotropic turbulence:

$$\Phi_{ij}^{(r)} = \frac{4}{5}kS_{ij} = -\frac{3}{5}(P_{ij} - \frac{2}{3}P\delta_{ij}), \quad (2.1.1)$$

where

$$\Phi_{ij}^{(r)} = -\langle p^{(r)}(u_{i,j} + u_{j,i}) \rangle,$$

$$S_{ij} = \frac{1}{2} \left( \frac{\partial U_i}{\partial x_j} + \frac{\partial U_j}{\partial x_i} \right),$$

$$P_{ij} = -\langle u_i u_k \rangle \frac{\partial U_j}{\partial x_k} - \langle u_j u_k \rangle \frac{\partial U_i}{\partial x_k}.$$

In the above:  $\Phi_{ij}^{(r)}$  is the “rapid” part of the pressure-strain correlation;  $p^{(r)}$  is the “rapid” part of the pressure fluctuation;  $U_i$  and  $u_i$  are mean and fluctuating velocities components;  $k = \frac{1}{2} \langle u_i u_i \rangle$  is the turbulent kinetic energy;  $P_{ij}$  is the production tensor;  $P = \frac{1}{2} P_{ii}$ ; and  $\delta_{ij}$  is the Kronecker delta symbol. Equation (2.1.1) is called the Crow constraint and its use in pressure-strain correlation modeling can be traced to Rotta<sup>2</sup>.

Currently, coefficients in pressure-strain correlation models are chosen to satisfy (2.1.1) at the RD limit. Models satisfying the Crow constraint perform well in rapidly-distorted isotropic turbulence. The models, however, are much less satisfactory (unphysical and unrealizable) in anisotropic turbulence, as will be shown later. As rapidly-distorted anisotropic turbulence is of great practical interest, it is important to develop modeling constraints such as equation (2.1.1) for anisotropic turbulence.

### *Previous research*

A review of previous rapid-distortion modeling studies is given in Hunt and Carruthers<sup>3</sup>. Sreenivasan and Narasimha<sup>4</sup> and Maxey<sup>5</sup> (and references therein) investigated the influence of various types of distortion and anisotropy levels on turbulence evolution. In their studies, only special cases of the initial energy spectrum tensor were considered. Various cases of three-component (3C) axisymmetric turbulence, with the Reynolds stress component along the axis of symmetry increasing from its isotropic value of  $2/3k$  to the maximum allowed value of  $k$ , were studied. Maxey<sup>5</sup> investigated, in some detail, the role of the pressure-strain correlation at the rapid distortion limit and the performance of the model of Launder *et al.*<sup>6</sup> in the homogeneous shear flow. Hunt & Carruthers<sup>3</sup> further pointed out that the asymptotic value of Reynolds stresses depend on the initial anisotropy level. An important conclusion from all these studies is that the level of initial anisotropy plays a crucial role in the subsequent turbulence evolution. However, these studies stop well short of developing general modeling constraints or guidelines in rapidly distorted anisotropic turbulence.

### *Current study*

The objectives of the present study are to:

- 1) Develop a better understanding of the pressure-strain correlation in highly anisotropic turbulence subject to various types of rapid distortion;
- 2) Assess model performance (physical consistency, realizability) by comparison with RDT data;
- 3) Seek physical principles and mathematical constraints, which can be used to guide development of better pressure-strain correlation models in the RD limit for anisotropic turbulence;
- 4) To estimate bounds on the values of the pressure-strain correlation.

Our first objective is similar to that of previous studies mentioned above. In the present study, we proceed further to characterize important physical features of pressure-strain correlation and establish new modeling guidelines in anisotropic turbulence. These guidelines should lead to pressure-strain correlation models of high degree of fidelity to the Navier-Stokes equations in the RD limit.

## **2.2 GOVERNING EQUATIONS**

The velocity fluctuation evolution equations in the RD limit are the following (see, *e.g.*, Pope<sup>8</sup>)

$$\frac{\overline{D} u_j}{\overline{D} t} = -u_i \frac{\partial U_j}{\partial x_i} - \frac{1}{\rho} \frac{\partial p^{(r)}}{\partial x_j};$$

$$\frac{\partial u_i}{\partial x_i} = 0; \quad (2.2.1)$$

$$\frac{1}{\rho} \nabla^2 p^{(r)} = -2 \frac{\partial U_i}{\partial x_j} \frac{\partial u_j}{\partial x_i}.$$

Here,  $\frac{\overline{D}}{\overline{D} t} = U_i \frac{\partial}{\partial x_i} + \frac{\partial}{\partial t}$ . The equations are written in Cartesian coordinates.

In homogeneous turbulence, the velocity and the pressure fields can be written in terms of their Fourier components:

$$\vec{u}(\vec{x}, t) = \sum_{\vec{k}} \hat{\vec{u}}(\vec{k}, t) e^{i\vec{k}(t) \cdot \vec{x}}, \quad p^{(r)}(\vec{x}, t) = \sum_{\vec{k}} \hat{p}(\vec{k}, t) e^{i\vec{k}(t) \cdot \vec{x}} \quad (2.2.2)$$

where  $\vec{k}(t)$  is the wavenumber vector and  $\hat{\vec{u}}(\vec{k}, t)$  is the Fourier coefficient vector of the velocity fluctuation. Then, equations (2.2.1) transform to the evolution equations for the components of vectors  $\vec{k}(t)$  and  $\hat{\vec{u}}(t)$

$$\frac{d\kappa_j}{dt} = -\kappa_l \frac{\partial U_l}{\partial x_j}, \quad (2.2.3)$$

$$\frac{d\hat{u}_j}{dt} = -\hat{u}_k \frac{\partial U_l}{\partial x_k} \left( \delta_{jl} - 2 \frac{\kappa_j \kappa_l}{\kappa^2} \right) \quad (2.2.4)$$

subject to the incompressibility condition:

$$\hat{u}_i \kappa_i = 0. \quad (2.2.5)$$

In Cambon and Scott<sup>9</sup>, it is suggested that equations (2.2.3)-(2.2.4) be referred to as the Kelvin-Townsend equations. For given initial conditions, equations (2.2.23)-(2.2.5) can be solved directly. Then, the covariance of two Fourier coefficients

$$\hat{R}_{ij}(\vec{k}, t) = \langle \hat{u}_i^*(\vec{k}, t) \hat{u}_j(\vec{k}, t) \rangle \quad (2.2.6)$$

can be extracted from the data for each given  $\vec{k}(t)$ . Summation of (2.2.6) over all wavenumber vectors gives the Reynolds stress components in the physical space:

$$\langle u_i u_j \rangle = \sum_{\vec{\kappa}} \hat{R}_{ij}(\vec{\kappa}, t). \quad (2.2.7)$$

Another way to obtain  $\hat{R}_{ij}$  and Reynolds stresses is to solve directly the evolution equation for the covariance of two Fourier coefficients of a given wavenumber vector

$$\frac{d \hat{R}_{ij}}{dt} = -\hat{R}_{ik} \frac{\partial U_j}{\partial x_k} - \hat{R}_{jk} \frac{\partial U_i}{\partial x_k} + 2 \hat{R}_{ik} \frac{\partial U_l}{\partial x_k} \frac{\kappa_j \kappa_l}{\kappa^2} + 2 \hat{R}_{jk} \frac{\partial U_l}{\partial x_k} \frac{\kappa_i \kappa_l}{\kappa^2}, \quad (2.2.8)$$

which is derived using equation (2.2.4). Details of the derivation can be found in Pope<sup>8</sup> (p. 412), for instance. Now, the continuity equation takes the following form

$$\kappa_i \hat{R}_{ij}(\vec{\kappa}) = \kappa_j \hat{R}_{ij}(\vec{\kappa}) = 0. \quad (2.2.9)$$

Equation (2.2.8) is a numerically more efficient alternative to equation (2.2.4) for calculating Reynolds stresses at the RD limit<sup>10</sup> and, hence, has been adopted in this study. Summation of (2.2.8) over all  $\vec{\kappa}(t)$  yields the Reynolds stress evolution equation in the RD limit:

$$\frac{d \langle u_i u_j \rangle}{dt} = P_{ij} + \Phi_{ij}^{(r)}, \quad (2.2.10)$$

where production  $P_{ij}$  is given by

$$P_{ij} = -\sum_{\vec{\kappa}} \left( \hat{R}_{ik} \frac{\partial U_j}{\partial x_k} + \hat{R}_{jk} \frac{\partial U_i}{\partial x_k} \right)$$

and the “rapid” pressure-strain correlation  $\Phi_{ij}^{(r)}$  is

$$\Phi_{ij}^{(r)} = 2 \sum_{\vec{\kappa}} \left( \hat{R}_{ik} \frac{\partial U_l}{\partial x_k} \frac{\kappa_j \kappa_l}{\kappa^2} + \hat{R}_{jk} \frac{\partial U_l}{\partial x_k} \frac{\kappa_i \kappa_l}{\kappa^2} \right).$$

Thus, the RDT equations can be used directly to study the physics of production and pressure-strain redistribution processes.

In the current study, RDT data are used to evaluate directly the accuracy of three popular models for the “rapid” part of the pressure-strain correlation - IP (isotropization-of-production) model<sup>11</sup>, LRR model<sup>6</sup>, and SSG model<sup>12</sup> - for given isotropic and anisotropic initial conditions. All models can be represented by the general form:



$$\Phi_{ij}^{(r)} = -C_1 P b_{ij} + \left( C_2^0 - C_2^1 \sqrt{b_{kk}^2} \right) k S_{ij} + C_3 k \left( b_{ik} S_{jk} + b_{jk} S_{ik} - \frac{2}{3} b_{kl} S_{kl} \delta_{ij} \right) + C_4 k (b_{ik} W_{jk} + b_{jk} W_{ik}) \quad (2.2.11)$$

In the above,  $b_{ij}$  denotes the anisotropy tensor and  $W_{ij}$  is the mean rotation-rate (vorticity) tensor:

$$b_{ij} = \frac{\langle u_i u_j \rangle}{2k} - \frac{1}{3} \delta_{ij}; \quad W_{ij} = \frac{1}{2} \left( \frac{\partial U_i}{\partial x_j} - \frac{\partial U_j}{\partial x_i} \right).$$

The models differ only in the value of coefficients, which are given in Table 2.1. The value 0.8 of the coefficient  $C_2^0$  recommended in all three models, comes from constraint (2.1.1).

### 2.3 CALCULATION PROCEDURE

The RDT equations ((2.2.3), (2.2.8)-(2.2.9)) and modeled Reynolds stress evolution equation (2.2.10) are solved in a variety of homogeneous turbulent flows. Mean flows investigated here are:

**homogeneous shear (HS)**

$$\frac{\partial U_i}{\partial x_j} = \begin{pmatrix} 0 & S & 0 \\ 0 & 0 & 0 \\ 0 & 0 & 0 \end{pmatrix},$$

**plain strain (PS)**

$$\frac{\partial U_i}{\partial x_j} = \begin{pmatrix} S & 0 & 0 \\ 0 & -S & 0 \\ 0 & 0 & 0 \end{pmatrix},$$

**axisymmetric contraction (AC)**

$$\frac{\partial U_i}{\partial x_j} = \begin{pmatrix} S & 0 & 0 \\ 0 & -S/2 & 0 \\ 0 & 0 & -S/2 \end{pmatrix},$$

**and axisymmetric expansion (AE),**

$$\frac{\partial U_i}{\partial x_j} = \begin{pmatrix} -2S & 0 & 0 \\ 0 & S & 0 \\ 0 & 0 & S \end{pmatrix}.$$

Initial condition specification requires the definition of terms *componentiality* (C) and *dimensionality* (D) of the turbulence field. In the present paper, turbulence *dimensionality* is always equal to three unless prohibited by incompressibility condition.

In keeping with the main objective of the paper, highly anisotropic as well as isotropic turbulent velocity fields are chosen as initial conditions. Anisotropic cases considered are: one-component (1C) and axisymmetric two-component (2C) turbulent states. Three kinds of 1C initial conditions are considered:

$$b_{ij} = \begin{pmatrix} \frac{2}{3} & 0 & 0 \\ 0 & -\frac{1}{3} & 0 \\ 0 & 0 & -\frac{1}{3} \end{pmatrix}; \quad b_{ij} = \begin{pmatrix} -\frac{1}{3} & 0 & 0 \\ 0 & \frac{2}{3} & 0 \\ 0 & 0 & -\frac{1}{3} \end{pmatrix}; \quad b_{ij} = \begin{pmatrix} -\frac{1}{3} & 0 & 0 \\ 0 & -\frac{1}{3} & 0 \\ 0 & 0 & \frac{2}{3} \end{pmatrix}. \quad (2.3.1)$$

They are denoted as 1C1, 1C2, and 1C3 respectively. The three axisymmetric 2C initial conditions are

$$b_{ij} = \begin{pmatrix} -\frac{1}{3} & 0 & 0 \\ 0 & \frac{1}{6} & 0 \\ 0 & 0 & \frac{1}{6} \end{pmatrix}; \quad b_{ij} = \begin{pmatrix} \frac{1}{6} & 0 & 0 \\ 0 & -\frac{1}{3} & 0 \\ 0 & 0 & \frac{1}{6} \end{pmatrix}; \quad b_{ij} = \begin{pmatrix} \frac{1}{6} & 0 & 0 \\ 0 & \frac{1}{6} & 0 \\ 0 & 0 & -\frac{1}{3} \end{pmatrix}, \quad (2.3.2)$$

which are denoted as 2C1, 2C2, and 2C3 respectively. Isotropic condition is given by

$$b_{ij} = 0, \quad i, j = 1, 2, 3. \quad (2.3.3)$$

Values of the anisotropy tensor given in (2.3.1)-(2.3.3) are used directly to solve modeled Reynolds stress evolution equation (2.2.10).

To solve RDT equations (2.2.3), (2.2.8), and (2.2.9), initial turbulence fields with desirable properties should be generated. Since many different choices of the wavenumber vectors and the Fourier coefficients of the velocity fluctuation can yield the required anisotropy, the choice of the initial fields for these quantities must be made carefully. In the present study the following assumptions on the initial distributions of vectors  $\vec{K}(t=0)$  and  $\hat{\vec{u}}(\vec{K}, t=0)$  are made:

- Velocity fluctuations in all permissible directions are equally energetic. That is, Fourier coefficients of initial velocity fluctuations in all permissible directions have the equal magnitude. Whether Fourier coefficient vectors are permitted in a specific direction is determined from the initial turbulence componentiality.
- For a given vector  $\hat{\vec{u}}(t=0)$  all permissible wavenumber vector directions are equally probable. Permissible wavenumber vector directions are determined purely by incompressibility condition (2.2.5).

Thus, the most general (unbiased) initial velocity field can be generated for the specified Reynolds stress tensor. For 1C turbulence, the initial vector  $\hat{u}$  is aligned along the corresponding unit vector. In 2C turbulence, initial vectors  $\hat{u}$  are uniformly distributed in a circle on the permissible plane. In 3C isotropic case, vectors  $\hat{u}$  are uniformly distributed on a sphere. The magnitudes of  $\hat{u}$  are such that the total initial turbulent kinetic energy is recovered.

For each vector  $\hat{u}(t=0)$ , the corresponding wavenumber vectors  $\vec{k}(t=0)$  are determined from assumption (b) above. Because equation (2.2.8) does not depend on the magnitude of the wavenumber vector, but on its direction only, one can assume, without loss of the generality that all permissible wavenumber vectors are of equal magnitude initially. Thus, to generate initially isotropic turbulence, wavenumber vectors are distributed evenly on the surface of a unit sphere. In 1C turbulence, vectors  $\vec{k}(t)$  are uniformly distributed in the unit circle lying in the plane normal to the initial vector  $\hat{u}$ . In 2C turbulence, the generation of vectors  $\vec{k}$  is explained below for the case of 2C3 turbulence.

In 2C3 turbulence initial vectors  $\hat{u}$  are equally distributed in the plane (1,2) (Fig. 1). The corresponding wavenumber vector distribution is dictated by incompressibility condition (assumption b). Effectively, the full set of vectors  $\vec{k}$  is divided into families, with each family having the same value of the projection of  $\vec{k}$  on axis 3 (Fig. 1):  $\kappa_3^i = |\kappa| \cos(\theta^{i-1} + d\theta)$ , for  $i = 2, N$  and  $\kappa_3^i = |\kappa|$ , for  $i = 1$ . Here,  $|\kappa| = 1$ ,  $\theta^1 = 0$ , and  $d\theta = \pi / 2(N-1)$ . All families carry equal amount of energy. Then, knowing the number of vectors  $\vec{k}$  in each family, one can determine the energy associated with each vector  $\vec{k}$  and  $\hat{R}_{ij}(\vec{k}, t=0)$ . Vectors  $\vec{k}$  in the cases of 2C2 turbulence and 2C1 turbulence are generated in the similar manner.

A fourth-order Runge-Kutta scheme was used for time integration of all equations.

## 2.4 RESULTS AND DISCUSSION

Results from computations of RDT equations ((2.2.3), (2.2.8)-(2.1.9)) and modeled Reynolds stress evolution equation (2.2.10) are now presented. The mean flows, the initial conditions, and basic outcomes from the RDT and model calculations are given in Table 2.2. The RDT calculations show evolution of anisotropy level in some cases (denoted by 'E') and no evolution in others ('N'). All isotropic turbulence cases evolve from their initial states.

Our RDT data interrogation focuses on the role of the pressure-strain correlation, especially its relation to production. The analysis is centered around the anisotropy evolution equation at the RD limit:

$$\frac{db_{ij}}{dt} = \frac{1}{2k} (P''_{ij} + \Phi_{ij}(r)), \quad (2.4.1)$$

where  $P''_{ij} (= P_{ij} - 2Pb_{ij} - \frac{2}{3}\delta_{ij}P)$  is the production of anisotropy. Also a crucial value in the analysis is the magnitude of anisotropy, which evolves according to

$$\frac{1}{2} \frac{d b_{ij} b_{ij}}{dt} = \frac{1}{2k} (P''_{ij} b_{ij} + \Phi_{ij}^{(r)} b_{ij}). \quad (2.4.2)$$

We first investigate if a generalized form of constraint (1) is possible for an anisotropic flow, that is, if the pressure-strain correlation merely counteracts certain fraction of the production. In such a case, the pressure-strain correlation could have one of two forms:

$$\Phi_{ij}^{(r)} \propto P''_{ij} \quad \text{or} \quad \Phi_{ij}^{(r)} \propto P'_{ij} (= P_{ij} - \frac{2}{3}\delta_{ij}P),$$

where the proportionality coefficient in each expression could be a constant or a scalar invariant of the mean velocity gradient tensor. The simplest manner to verify the existence of such a linear relationship would be to compute the following ratios

$$R1 = \frac{\Phi_{ij}^{(r)} \Phi_{ij}^{(r)}}{P'_{ij} P''_{ij}} \quad \text{or} \quad R2 = \frac{\Phi_{ij}^{(r)} \Phi_{ij}^{(r)}}{P'_{ij} P'_{ij}}. \quad (2.4.3)$$

The first ratio  $R1$  in (2.4.3) is, probably, more justified in anisotropic turbulence considering the form of anisotropy evolution equation (2.4.1) in the RD limit. In isotropic turbulence, we have  $R1 = R2 = 0.36$  in accordance with (1). The RDT data confirm that the ratio  $R1$  is indeed preferable to  $R2$  because at  $t=0$   $R1$  shows less variation for different initial flow conditions. Nevertheless, even the ratio  $R1$  changes from case to case:  $R1=1$  for HS (1C2, 2C1) and  $R1=0.25$  for HS (2C2), PS (2C1, 2C2, 2C3), AE and AC (2C2, 2C3) flows. Further  $R1$  and  $R2$  change substantially with turbulence evolution. Some examples of  $R1$  evolution are shown in Fig. 2.2. In none of the cases considered, the ratio  $R1$  (and  $R2$ ) is equal to the isotropic value 0.36.

One clear conclusion can be drawn from RDT data: the pressure-strain correlation does more than merely counteract the anisotropy production. In the absence of a unique relationship between the production and pressure-strain correlation, subtler connections are now investigated. One of the main features of the pressure-strain correlation is its redistributive nature. The fact that the pressure-strain correlation term  $\Phi_{ij}^{(r)}$  is traceless reveals that it does not alter the total energy. It is generally believed that the pressure-strain correlation removes energy from high-energy components and enhances lower-energy components. In contrast, the production process is believed to increase anisotropy by injecting energy into selected components of the Reynolds stress tensor. The specific issues investigated are the following.

- 1) Can there be redistribution without production? That is, what happens to  $\Phi_{ij}^{(r)}$ , when

$$P''_{ij} = 0.$$

- 2) Does the “rapid” pressure-strain correlation always extract energy from high-energy components and deposit it into low-energy ones? This can be answered by monitoring the sign of  $\Phi_{ij}^{(r)} b_{ij}$  (refer to equation 2.4.2).
- 3) Can more energy be redistributed than produced in the first place? That is, can the  $R1$  (or  $R2$ ) value be greater than unity.

### 2.4.1 RDT results

#### *Non-evolving cases*

The RDT calculations demonstrate that in some cases (denoted by ‘N’ in Table 2.2) turbulence anisotropy does not change from its initial level. In other words, the term  $db_{ij}/dt$  on the left side of equation (2.4.1) is equal to zero for each component of the anisotropy tensor  $b_{ij}$ . It is straightforward to show (see the Appendix) that in such cases all components of the production term  $P''_{ij}$  are exactly equal to zero. It follows then from equation (2.4.1), that the pressure-strain tensor components should also be equal to zero. Thus, if  $P''_{ij} = 0$ , then  $\Phi_{ij}^{(r)} = 0$ . In order to confirm this, we examine the second invariant of tensors  $P''_{ij}$  and  $\Phi_{ij}^{(r)}$ , i.e.,  $P''_{ij} P''_{ij}$  and  $\Phi_{ij}^{(r)} \Phi_{ij}^{(r)}$ . The second invariant contains information about all tensor components. If all individual components of the tensor are equal to zero, so is the invariant. The RDT calculations show that when the invariant  $P''_{ij} P''_{ij}$  is equal to zero, then  $\Phi_{ij}^{(r)} \Phi_{ij}^{(r)}$  is also equal to zero. Note that in these cases,  $P_{ij}$  or  $P'_{ij}$  need not vanish.

#### *Evolving cases*

Cases in which the RDT predicts turbulence anisotropy evolution are denoted by ‘E’ in Table 2.2. If the pressure-strain correlation decreases anisotropy and the production term increases its level, then  $\Phi_{ij}^{(r)} b_{ij}$  in (2.4.2) should be negative, and  $P''_{ij} b_{ij}$  should be positive. The computed RDT values of  $P''_{ij} b_{ij}$  and  $\Phi_{ij}^{(r)} b_{ij}$  in some representative cases are plotted in Fig. 3. The  $P''_{ij} b_{ij}$  evolution is shown with a solid line (without symbols), while the  $\Phi_{ij}^{(r)} b_{ij}$  evolution is represented by dashed line (without symbols). It is clearly seen that  $P''_{ij} b_{ij}$  is always positive as expected, while  $\Phi_{ij}^{(r)} b_{ij}$  is predominantly negative (again as expected). In one case (Fig. 3e) it assumes small positive values at latter stages of simulation. It can be argued though that at this late stage of evolution, RDT equations may not represent the real turbulence physics. It would be interesting to analyze the circumstances under which  $\Phi_{ij}^{(r)} b_{ij}$  is positive. As a general rule, we conclude that  $\Phi_{ij}^{(r)} b_{ij}$  is negative, implying that the pressure-strain correlation predominantly reduces the Reynolds stress anisotropy.

The RDT data demonstrate that the magnitude of  $R1$  and  $R2$  initially never exceeds unity. Some results are shown in Fig. 2. In few cases, for example in AE (2C2) flow (Fig. 2b),  $R1$  exceeds unity at long times. This is again at time when the RDT may not accurately reflect the turbulence

physics. The conclusion then is that the magnitude of the redistribution does not in general exceed that of the production.

For strain-dominated mean flows, RDT results appear to imply that the behavior of the pressure-strain correlation is as follows irrespective of the initial anisotropy:

$$1) \Phi_{ij}^{(r)} = 0, \text{ when } P''_{ij} = 0;$$

$$2) \Phi_{ij}^{(r)} b_{ij} \leq 0;$$

$$3) R1 \text{ and } R2 \leq 1.$$

It would be reasonable to demand that models be, at least, qualitatively consistent with the RDT data.

#### 2.4.2 Model calculations

Three models for the “rapid” part of the pressure-strain correlation (IP, LRR, and SSG) are now compared with the RDT data. The most fundamental aspects of the model calculations are tabulated in Table 2.2. In the table, ‘ER’ stands for an evolving realizable trajectory and ‘EU’ denotes an evolving unrealizable solution. The table demonstrates that in many cases models yield evolution of turbulence anisotropy when the RDT clearly shows no evolution. In other cases, when the RDT shows evolution, model behavior is unrealizable. Thus, two categories of undesirable model behavior can be recognized: inconsistency with turbulence (RDT) physics and unrealizable evolution trajectories.

**Inconsistency.** If a turbulence model predicts evolution of Reynolds stress anisotropy when RDT indicates no evolution, the model is labeled as being inconsistent with turbulence physics. In Table 2.2, when a model shows evolution (denoted as ‘ER’ and ‘EU’), but the RDT does not (‘N’), we have inconsistency.

**Unrealizability.** As is common practice, a model is labeled as unrealizable, if it produces negative diagonal components of the Reynolds stress tensor (in the principal coordinates). In such a case, a model evolution trajectory passes from the realizable region (inside Lumley triangle) to the non-realizable area (outside Lumley triangle). In all cases identified with ‘EU’ (in Table 2.2), the model behavior is unrealizable.

We will now compare model calculations with RDT data and try to explain the physical failing underlying inconsistent and unrealizable model behavior. In particular, the connection between the violations and the proposed modeling guidelines will be sought.

#### Non-evolving cases

We discuss in detail, at first, the results from four cases: AC(1C2), AE(1C2), HS(1C1), and PS(1C1). The cases are identified by the mean flow and the initial turbulence anisotropy (in parentheses). In these cases, RDT calculations show no evolution, as is seen from Table 2.2.

Thus,  $b_{ij}(t) = b_{ij}(0)$ ;  $P''_{ij} b_{ij} = 0$  and  $\Phi_{ij}^{(r)} b_{ij} = 0$ . Models, however, demonstrate various behavior patterns including inconsistent and unrealizable evolution. The model evolution

trajectories are tracked on the  $(\xi, \eta)$  invariant plane: where the invariants are defined by  $6\eta^2 = b_{ij}b_{ji}$ ,  $6\xi^3 = b_{ij}b_{jk}b_{ki}$ . To assess realizability violation, the Lumley invariant triangle is also shown. A trajectory is deemed unrealizable when it crosses the boundary of the Lumley triangle.

*Case AC (IC2).* All models predict spurious evolution in this case, but evolution trajectories stay inside the Lumley triangle (Fig. 2.4a). Thus, all three models considered predict inconsistent, but realizable behavior. To understand the origin of poor model behavior, we now examine the ratio  $R1$  (Fig. 2.4b) and the invariants  $P'_{ij}b_{ij}$  and  $\Phi_{ij}^{(r)}b_{ij}$  (Fig. 2.4c). The initial value of  $\Phi_{ij}^{(r)}\Phi_{ij}^{(r)}$  implied by each model is non-zero, while the  $P'_{ij}P'_{ij}$  value is equal to zero as can be seen from  $R1 \rightarrow \infty$  at  $t=0$  (Fig. 2.4b). Non-zero model  $\Phi_{ij}^{(r)}$ , then, causes the model trajectory to evolve. In RDT calculations, both  $\Phi_{ij}^{(r)}$  and  $P'_{ij}$  are equal to zero resulting in no evolution. The connection between inconsistent model behavior and violation of criterion 1 is easily established. From Fig. 2.4(c), it is seen, that for each model,  $P'_{ij}b_{ij}$  is positive and  $\Phi_{ij}^{(r)}b_{ij}$  is negative. To summarize, all models violate criteria 1 and 3, and not criterion 2 in this case.

*Case HS (IC1).* The IP model predicts no anisotropy evolution in agreement with the RDT. In both cases - IP-model and RDT calculations - initial values of  $\Phi_{ij}^{(r)}$  and  $P'_{ij}$  are equal to zero. Results from LRR and SSG models are shown in Fig. 2.5. The LRR model shows inconsistent and unrealizable behavior. The SSG model predictions are inconsistent, but realizable (Fig. 2.5a). From Fig. 5(b) it is clear that both models violate criteria 1 and 3. As regards criterion 2, the LRR model violates it, but the SSG model does not (Fig. 5c). The inference is that unrealizable model behavior is linked to violation of criterion 2. This conclusion is further corroborated by following cases.

*Case PS (IC1).* In this case all models exhibit inconsistent and unrealizable behavior (Fig. 2.6a). All three models violate all three criteria (Figs. 2.6b and 2.6c).

*Case AE (IC2).* Again, all models predict inconsistent and unrealizable behavior (Fig. 2.7a), and all three criteria are violated (Figs. 2.7b and 2.7c). The SSG model further predicts that production tends to reduce anisotropy ( $P'_{ij}b_{ij} < 0$ ), which is completely inconsistent with the RDT and turbulence physics.

### *Evolving cases*

Now we consider cases where the RDT shows evolution of initial turbulence anisotropy (see Table 2.2). In all these cases, all three models show anisotropy evolution also. In this sense their behavior is consistent with the RDT. When a model predicts consistent and realizable behavior, no criterion violation is observed. Some examples are shown in Figs. 2.3 (a-c) for criterion 2 and in Figs. 2.2(a) and 2.2(b) for criterion 3. Results for all cases studied are summarized in Table

2.3. In many cases, the model evolution is unrealizable. As examples, cases AC (2C2) and PS (2C2) will be discussed in detail. (Criterion 1 does not apply for evolving cases).

*Case AC (2C2).* The RDT trajectory starts from the 2C-axisymmetric turbulence corner of the Lumley triangle and evolves towards the 1C turbulence corner (Fig. 2.8a). All three model trajectories initially exit the Lumley triangle, but later recover and re-enter the realizability zone (Fig. 2.8a). The model prediction after the first trajectory exit from the Lumley triangle is irrelevant and, therefore, the model behavior must be deemed unrealizable. The reason for the violation can be seen in Fig. 2.3(d). The value of  $\Phi_{ij}^{(r)}b_{ij}$  predicted by each model is initially positive leading to an increase of anisotropy level. At later times, the  $\Phi_{ij}^{(r)}b_{ij}$  values become negative as the Reynolds stresses recover to realizable values. The RDT value of  $\Phi_{ij}^{(r)}b_{ij}$  is always negative. Criterion 2 is violated, but not criterion 3 (Fig. 2.2c).

*Case PS (2C2).* The RDT trajectory is similar to the AC(2C2) case (Fig. 2.8b). All models are again unrealizable (Fig. 2.8b). The degree of violation in this case is much larger and there is no recovery to realizable values. The explanation is again found by investigating the behavior of  $\Phi_{ij}^{(r)}b_{ij}$  presented in (Fig. 2.3e). The model values of  $\Phi_{ij}^{(r)}b_{ij}$  are positive and substantially larger than in the previous case making recovery to realizable values difficult. The RDT values are, again, always negative. Criterion 3 is not violated (Fig. 2.2d).

All the calculated results are summarized in Table 2.3. In Table 2.3, 'C1', 'C2', and 'C3' represent the three criteria. Violation of a criterion is denoted by 'V' and non-violation is shown by 'N'. To clearly demonstrate the connection between undesirable behavior and criteria violation, two columns – recording consistency and realizability - are also added in Table 2.3. In these columns, again 'V' indicates violation and 'N' shows non-violation. The relationship between undesirable model behavior and modeling guideline violation is clearly evident. Violations of criteria 1 and 3 are associated with spurious evolution and inconsistent model behavior. Violations of criterion 2 and realizability condition are connected.

Implications of the RDT and model calculations are now summarized.

- 1) Without exceptions, the RDT data indicates that  $\Phi_{ij}^{(r)} = 0$ , when  $P''_{ij} = 0$ . Inconsistent model behavior is imminent when  $\Phi_{ij}^{(r)}$  is non-zero as  $P''_{ij}$  vanishes. Therefore, criterion 1 is a mathematical constraint that a model must be mandated to satisfy. Another important inference is that for this combination of Reynolds stresses and mean velocity gradients, the "rapid" pressure-strain correlation assumes a unique value, which is zero.
- 2) From the results in this section, it is clear that  $\Phi_{ij}^{(r)}b_{ij}$  being positive is not a desirable feature in a model, since all observed realizability violations are associated with such behavior. In all these cases, the RDT values of  $\Phi_{ij}^{(r)}b_{ij}$  remain negative. The underlying physics is now explained. When  $\Phi_{ij}^{(r)}b_{ij}$  is positive, the model extracts energy from low-energy components and deposits it into high-energy components. This action continues even



when the low-energy component is completely depleted, driving that component into negative values. Mathematically, this is much like counter-gradient transport, which almost always has a destabilizing influence. While the RDT data does permit this destabilizing energy transfer in very rare instances, physics incumbent in the RDT equations ensures a delicate balance between production and redistributive processes leading to realizable behavior. It remains to be seen if single-point closure models can be developed to replicate this delicate balance. Until this issue is addressed satisfactorily, criterion 2 must be considered as an important constraint that a model should satisfy.

- 3) Much like criterion 2, criterion 3 appears to be physically reasonable, although not always true in RDT. This criterion also suggests approximate bounds on the pressure-strain correlation magnitude:  $0 \leq \Phi_{ij}^{(r)} \Phi_{ij}^{(r)} \leq P''_{ij} P''_{ij}$ . Thus, the larger the anisotropy production, the wider is the range of values that the correlation can take. The margin of error incurred in pressure-strain correlation modeling is therefore likely to increase with increasing anisotropy production, even with the most accurate models.

## 2.5 CONCLUSIONS

Rapid distortion calculations of initially anisotropic turbulence are performed to better understand the physics of the pressure-strain correlation. The specific objectives are to establish "universal" principles that underlie pressure-strain correlation behavior and estimate the extent of range of values that the correlation can take for given combinations of Reynolds stresses and mean velocity gradients.

In the rapid distortion limit, turbulence evolution depends on various factors: type of anisotropy, degree of anisotropy, and the imposed mean-flow deformation. Consequently, the pressure-strain correlation term will also depend on these parameters. While the behavior of the pressure-strain correlation can be quite complex and not easily generalized in anisotropic turbulence, certain physical features can be identified as being universal. The RDT calculations performed in this paper show that in mean strain-dominated flows the dynamics of turbulence is such that:

- i)  $\Phi_{ij}^{(r)} = 0$ , when  $P''_{ij} = 0$ .
- ii)  $P''_{ij} b_{ij} > 0$ , whereas  $\Phi_{ij}^{(r)} b_{ij} \leq 0$ .
- iii)  $0 \leq \Phi_{ij}^{(r)} \Phi_{ij}^{(r)} \leq P''_{ij} P''_{ij}$ .

It is proposed that the above criteria be used as guidelines for developing "rapid" pressure-strain correlation models.

Reynolds stress transport model calculations performed at the rapid distortion limit display unphysical (inconsistent) and unrealizable behavior for some initial turbulence anisotropies and mean flows. Inconsistent behavior refers to spurious evolution predicted by a model when the RDT indicates no change in anisotropy from its initial level. Clearly, in a full-turbulence equation set, there may be evolution from an anisotropic initial state. But this evolution must be initiated by "slow" pressure-strain correlation or dissipation terms.

Close examination of the RSTM results reveal that both unrealizable and inconsistent model behavior can be directly related to violations of the constraints proposed in this paper. Inconsistent behavior occurs when the model pressure-strain correlation does not vanish as the production of anisotropy goes to zero. Unrealizable model behavior is observed when the model pressure-strain correlation unphysically attempts to increase anisotropy rather than diminish it.

In ongoing work<sup>14</sup> we demonstrate that current models yield realizable and consistent behavior when their coefficients are modified to satisfy the constraints proposed in this paper.

The results and analysis presented in this paper should aid in better understanding the role of the pressure-strain correlation in turbulence and hence, enable us to develop improved models for this term. Similar examination of mean rotation-dominated flows will be undertaken in the future.

#### *ACKNOWLEDGEMENT*

This work was sponsored (in part) by the Air Force Office of Scientific Research, USAF, under grant/contract number F49620-01-1-0476. Part of the work was also supported by NASA under NAG-01-005. The first author would like to thank Drs. C. L. Streett and B. A. Singer of NASA Langley Research Center for their encouragement and support.

## APPENDIX:

The RDT results show (Table 2.2) that in the following cases: 1C1, 1C3 (for all mean flows), 1C2 (AC, AE, PS), 2C1(AC, AE), and 2C2(HS), initial anisotropy of turbulence does not change. These are cases, when the production-of-anisotropy term  $P''_{ij}$  in equation (2.4.1) is equal to zero for all Reynolds stresses at  $t = 0$ .

As an example, let us consider the mean flow under axisymmetric contraction, where  $U_{1,1} = S$ ,  $U_{2,2} = U_{3,3} = -S/2$ , and the rest of the components is equal to zero. In such a flow, the components of the Reynolds stress production tensor

$$P_{ij} = -\langle u_i u_k \rangle \frac{\partial U_j}{\partial x_k} - \langle u_j u_k \rangle \frac{\partial U_i}{\partial x_k}$$

are  $P_{11} = -2S \langle u_1 u_1 \rangle$ ,  $P_{22} = S \langle u_2 u_2 \rangle$ ,  $P_{33} = S \langle u_3 u_3 \rangle$ , and the others are equal to zero.

For different initial turbulence anisotropy cases one has

$$1C1: \langle u_1 u_1 \rangle = 2k, P_{11} = -4Sk, P_{22} = P_{33} = 0, 2P = -4Sk,$$

$$1C2: \langle u_2 u_2 \rangle = 2k, P_{22} = 2Sk, P_{11} = P_{33} = 0, 2P = 2Sk,$$

$$1C3: \langle u_3 u_3 \rangle = 2k, P_{33} = 2Sk, P_{11} = P_{22} = 0, 2P = 2Sk,$$

$$2C1: \langle u_1 u_1 \rangle = 0, \langle u_2 u_2 \rangle = \langle u_3 u_3 \rangle = k, P_{11} = 0, P_{22} = P_{33} = Sk, 2P = 2Sk,$$

$$2C2: \langle u_2 u_2 \rangle = 0, \langle u_1 u_1 \rangle = \langle u_3 u_3 \rangle = k, P_{11} = -2kS, P_{22} = 0, P_{33} = Sk, 2P = -Sk,$$

$$2C3: \langle u_3 u_3 \rangle = 0, \langle u_1 u_1 \rangle = \langle u_2 u_2 \rangle = k, P_{11} = -2kS, P_{22} = Sk, P_{33} = 0, 2P = -Sk.$$

Then, the components of the production-of-anisotropy tensor  $P''_{ij} = P_{ij} - 2Pb_{ij} - \frac{2}{3}\delta_{ij}P$  in each case are

$$1C1: P''_{11} = P''_{22} = P''_{33} = 0,$$

$$1C2: P''_{11} = P''_{22} = P''_{33} = 0,$$

$$1C3: P''_{11} = P''_{22} = P''_{33} = 0,$$

$$2C1: P''_{11} = P''_{22} = P''_{33} = 0,$$

$$2C2: P''_{11} = -\frac{3}{2}Sk, P''_{22} = 0, P''_{33} = \frac{3}{2}Sk,$$

$$2C3: P''_{11} = -\frac{3}{2}Sk, P''_{22} = \frac{3}{2}Sk, P''_{33} = 0.$$

Non-diagonal components of  $P''_{ij}$  are equal to zero in all cases. It is seen that only in two cases (2C2 and 2C3) there are non-zero components of  $P''_{ij}$  and, therefore, the invariant  $P''_{ij}P''_{ij}$  has a non-zero value. In these two cases, the RDT data show the turbulence anisotropy evolution

from the initial level. In other cases (1C1, 1C2, 1C3, and 2C1) there is no production of anisotropy and, as RDT computations demonstrate, no change of initial anisotropy occurs. It follows then from equation (2.4.1), that the pressure-strain tensor components have to be also equal to zero in such cases.

For other mean flow configurations, the similar analysis can be easily made, which leads to the same conclusions.

## REFERENCES

1. S. Crow, "Viscoelastic properties of fine-grained turbulence," *J. Fluid Mech.* **33**, 1 (1968).
2. J. C. Rotta, "Statistische theorie nichthomogener turbulenz 1," *Z.Phys.* **129**, 547 (1951).
3. J. C. R. Hunt and D. J. Carruthers, "Rapid distortion theory and the "problems "of turbulence," *J. Fluid Mech.* **212**, 497 (1990).
4. K. R. Sreenivasan and R. Narasimha, "Rapid distortion of axisymmetric turbulence," *J. Fluid Mech.* **84**, 497 (1978).
5. M. R. Maxey, "Distortion of turbulence in flows with parallel streamlines," *J. Fluid Mech.* **124**, 261 (1982).
6. B. E. Launder, G. J. Reece, and W. Rodi, "Progress in the development of a Reynolds stress turbulent model," *J. Fluid Mech.* **68**, 537 (1973).
7. J. L. Lumley, "Computational modeling of turbulent flows," *Adv. Appl. Mech.* **18**, 123 (1978).
8. S. B. Pope, *Turbulent Flows* (Cambridge University Press, Cambridge, 2000).
9. C. Cambon and J. F. Scott, "Linear and nonlinear models of anisotropic turbulence," *Annual Rev. Fluid Mech.* **31**, 1 (1999).
10. S. C. Kassinos and W. C. Reynolds, "A particle representation model for the deformation of homogeneous turbulence," *Annual Research Briefs, Center for Turbulence Research, NASA Ames/Stanford University*, 1996, p. 31.
11. D. Naot, A. Shavit, and M. Wolfshtein, "Interactions between components of the turbulent velocity correlation tensor due to pressure fluctuations," *Israel J. Technol.* **8**, 259 (1970).
12. C. G. Speziale, S. Sarkar, and T. B. Gatski, "Modeling the pressure-strain correlation of turbulence: An invariant dynamical systems approach," *J. Fluid Mech.* **227**, 245 (1991).
13. W. C. Reynolds and S. C. Kassinos, "A one-point model for the evolution of the Reynolds stress and structure tensors in rapidly deformed homogeneous turbulence," *Proc. R. Soc. London, Ser. A*, **451**, 87 (1995).
14. S. S. Girimaji and Sambasivan (2002).

	LRR-IP	LRR-QI	SSG
$C_1^1$	0	0	1.8
$C_2^0$	0.8	0.8	0.8
$C_2^1$	0	0	1.3
$C_3$	1.2	1.75	1.25
$C_4$	1.2	1.31	0.4

**Table 2.1** Model coefficients for expression (12)

Initial conditions	Flow	Solution trajectories			
		RDT	Model		
			IP	LRR	SSG
1C1	AC	N	EU	EU	EU
	AE	N	ER	ER	ER
	PS	N	EU	EU	EU
	HS	N	N	EU	ER
1C2	AC	N	ER	ER	ER
	AE	N	EU	EU	EU
	PS	N	ER	ER	ER
	HS	E	ER	ER	ER
1C3	PS	N	N	EU	EU
	HS	N	N	EU	EU
2C1	AC	N	ER	ER	ER
	AE	N	EU	EU	EU
	PS	E	ER	ER	ER
	HS	E	ER	ER	ER
2C2	AC	E	EU	EU	EU
	AE	E	ER	ER	ER
	PS	E	EU	EU	EU
	HS	N	N	ER	ER
2C3	PS	E	ER	ER	ER
	HS	E	ER	ER	ER
isotropic	AC	E	ER	ER	ER
	AE	E	ER	ER	ER
	PS	E	ER	ER	ER
	HS	E	ER	ER	ER

**Table 2.2** Notations: (E) evolving trajectory; (N) no evolving; (U) unrealizable evolution; (R) realizable evolution. 1C3 (AC, AE) case is equivalent to 1C2 (AC, AE); and 2C3 (AC, AE) case is equivalent to 2C2 (AC, AE).

Mean flow	Anisotropy condition	Model	Realizability	Consistency	C1	C2	C3
AC	1C1	IP	V	V	V	V	V
		LRR	V	V	V	V	V
		SSG	V	V	V	V	V
	1C2	IP	N	V	V	N	V
		LRR	N	V	V	N	V
		SSG	N	V	V	N	V
	2C1	IP	N	V	V	N	V
		LRR	N	V	V	N	V
		SSG	N	V	V	N	V
	2C2	IP	V	N	N	V	N
		LRR	V	N	N	V	N
		SSG	V	N	N	V	N
AE	1C1	IP	N	V	V	N	V
		LRR	N	V	V	N	V
		SSG	N	V	V	N	V
	1C2	IP	V	V	V	V	V
		LRR	V	V	V	V	V
		SSG	V	V	V	V	V
	2C1	IP	V	V	V	V	V
		LRR	V	V	V	V	V
		SSG	V	V	V	V	V
PS	1C1	IP	V	V	V	V	V
		LRR	V	V	V	V	V
		SSG	V	V	V	V	V
	1C2	IP	N	V	V	N	V
		LRR	N	V	V	N	V
		SSG	N	V	V	N	V
	1C3	LRR	V	V	V	V	V
		SSG	V	V	V	V	V
	2C2	IP	V	N	N	V	N
		LRR	V	N	N	V	N
		SSG	V	N	N	V	N
HS	1C1	LRR	V	V	V	V	V
		SSG	N	V	V	N	V
	1C3	LRR	V	V	V	V	V
		SSG	V	V	V	V	V
	2C2	LRR	N	V	V	N	V
		SSG	N	V	V	N	V

**Table 2.3** Notations: (C1) criterion 1; (C2) criterion 2; (C2) criterion 3 (C3); (N) non-violation; (V) violation .

**Figure 2.1** Coordinate scheme for the 2C3 initial turbulence state.

**Figure 2.2** Evolution of the ratio  $R1$ . Cases: a) HS (1C2), b) AE (2C2), c) AC (2C2), d) PS (2C2).

Notations are (—) RDT, ( $\bullet^*$ ) IP model, ( $\oplus$ ) LRR model, ( $\boxtimes$ ) SSG model.

**Figure 2.3** Evolution of terms  $P'_{ij} b_{ij}$  and  $\Phi_{ij}^{(r)} b_{ij}$  in equation (17). Cases: a) PS (isotropic), b) HS (1C2), c) AE (2C2), d) AC (2C2), e) PS (2C2). Notations: for  $P'_{ij} b_{ij}$  (—) RDT, ( $\circ$ —) IP, ( $\triangle$ —) LRR, ( $\square$ —) SSG; for  $\Phi_{ij}^{(r)} b_{ij}$  (- -) RDT, ( $\circ$ -) IP, ( $\triangle$ -) LRR, ( $\square$ -) SSG.

**Figure 2.4** AC flow with 1C2 initial turbulence state: a) Lumley triangle, b) evolution of the  $R1$  parameter, c) evolution of invariants  $P'_{ij} b_{ij}$  and  $\Phi_{ij}^{(r)} b_{ij}$ . In Fig. 4(a) the black dots ( $\bullet$ ) mark the corners of Lumley triangle corresponding to isotropic, 2C, and 1C conditions. Other notations see in Figs. 2.2 and 2.3.

**Figure 2.5** HS flow with 1C1 initial turbulence state: a) Lumley triangle, b) evolution of the  $R1$  parameter, c) evolution of invariants  $P'_{ij} b_{ij}$  and  $\Phi_{ij}^{(r)} b_{ij}$  (notations are the same as in Figs. 2.2-2.4).

**Figure 2.6** PS flow with 1C1 initial turbulence state: a) Lumley triangle, b) evolution of the  $R1$  parameter, c) evolution of invariants  $P'_{ij} b_{ij}$  and  $\Phi_{ij}^{(r)} b_{ij}$  (notations are the same as in Figs. 2.2-2.4).

**Figure 2.7** AE flow with 1C2 initial turbulence state: a) Lumley triangle, b) evolution of the  $R1$  parameter, c) evolution of invariants  $P'_{ij} b_{ij}$  and  $\Phi_{ij}^{(r)} b_{ij}$  (notations are the same as in Figs. 2.2-2.4).

**Figure 2.8** Solution trajectories in the Lumley triangle Cases: a) AC (2C2 and isotropic), b) PS (2C2 and isotropic). Notations are (—) RDT, ( $\circ$ ) IP model, ( $\triangle$ ) LRR model, ( $\square$ ) SSG model for initially anisotropic turbulence. The corners of Lumley triangle are marked with ( $\bullet$ ).



**Fig. 2.1**

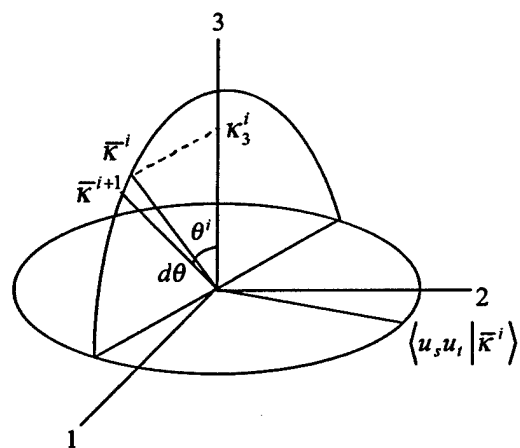
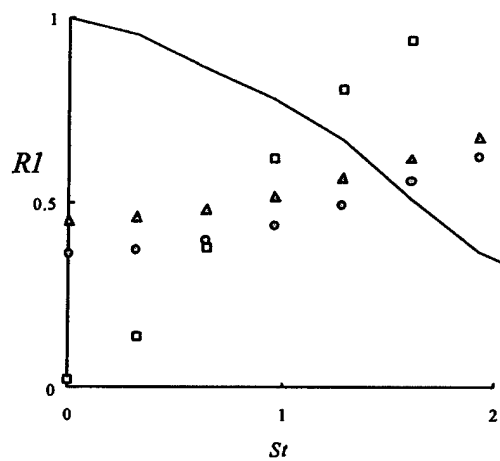
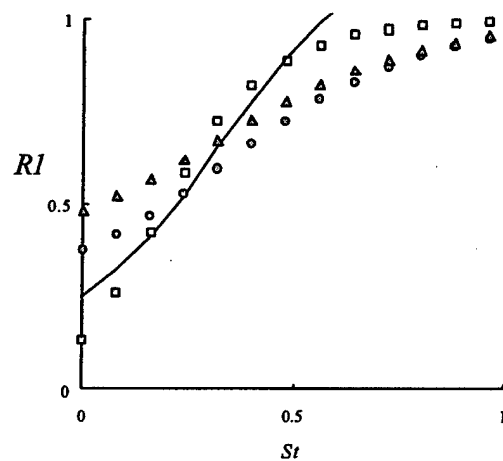


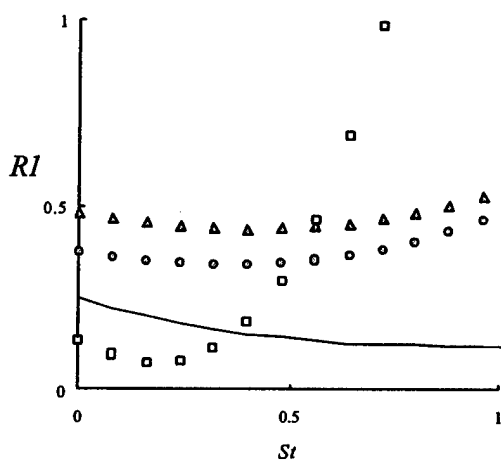
Fig. 2.2



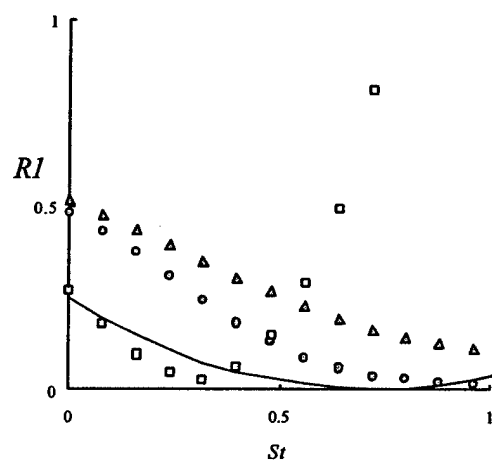
(a)



(b)

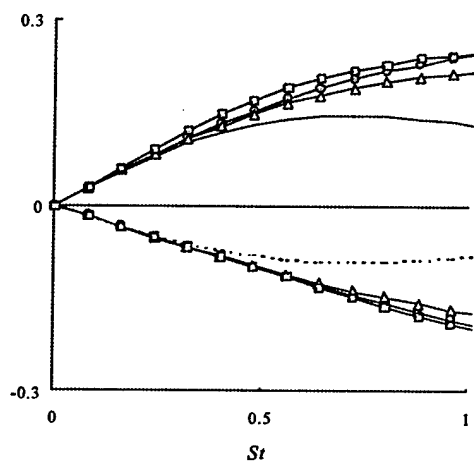


(c)

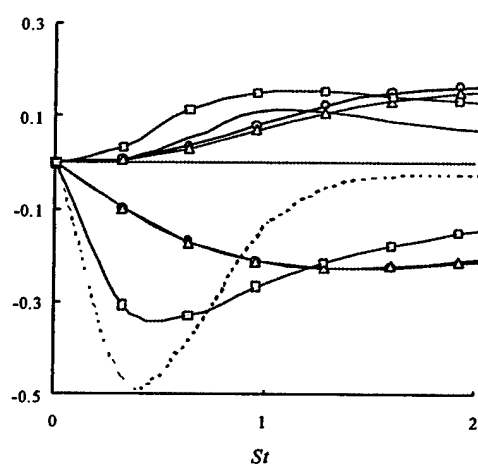


(d)

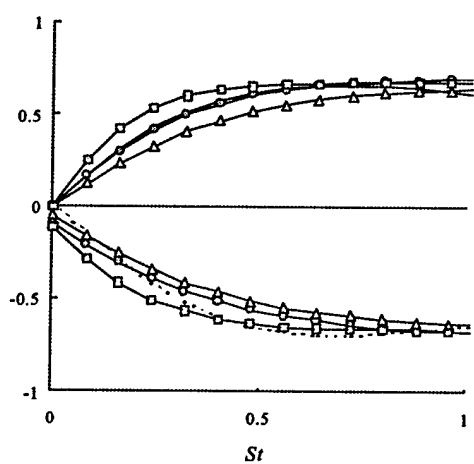
**Fig. 2.3**



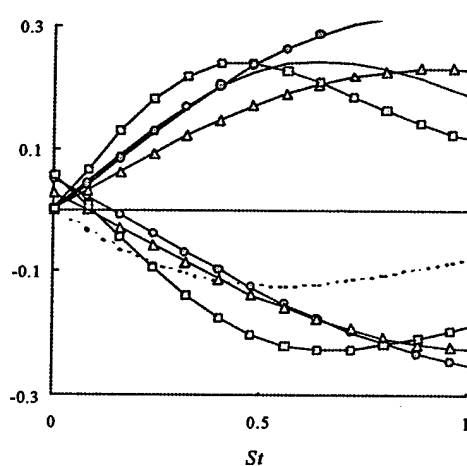
(a)



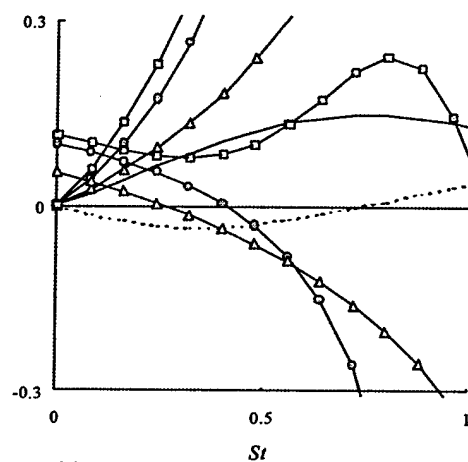
(b)



(c)

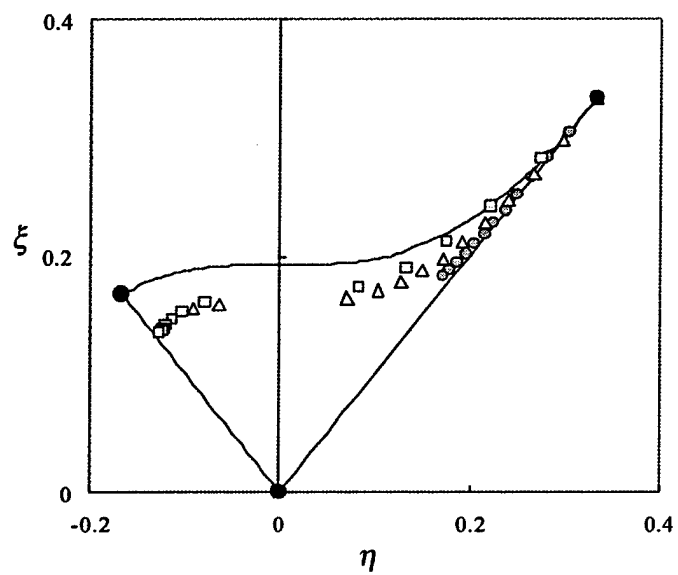


(d)

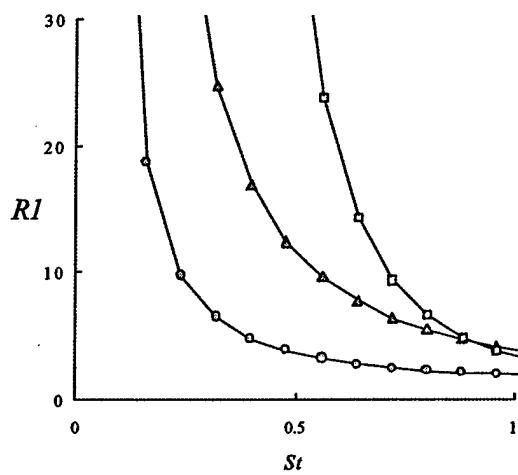


(e)

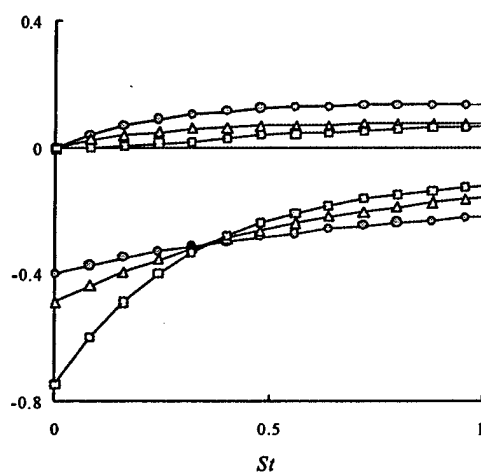
**Fig. 2.4**



**(a)**

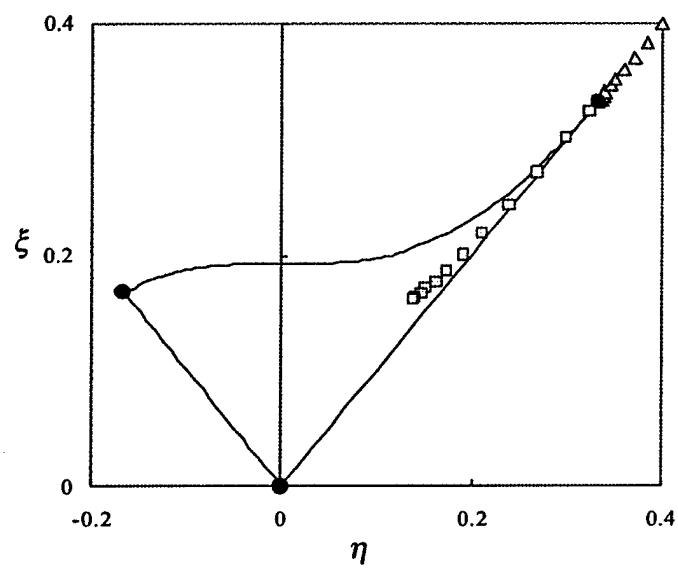


**(b)**

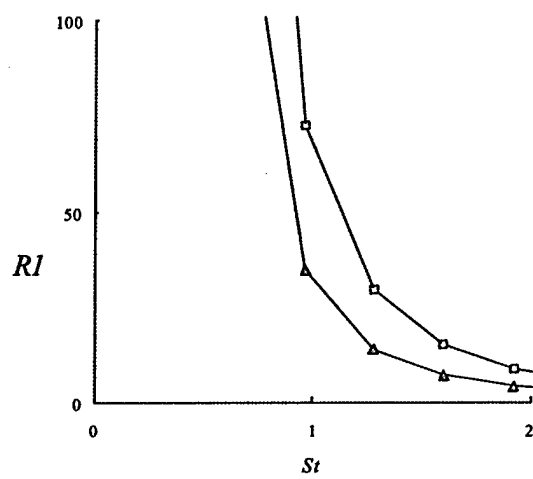


**(c)**

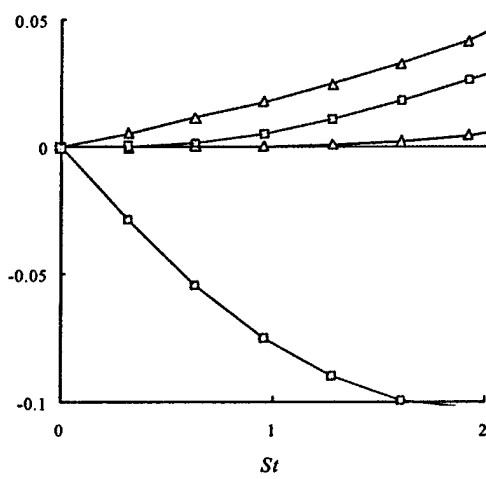
**Fig. 2.5**



(a)

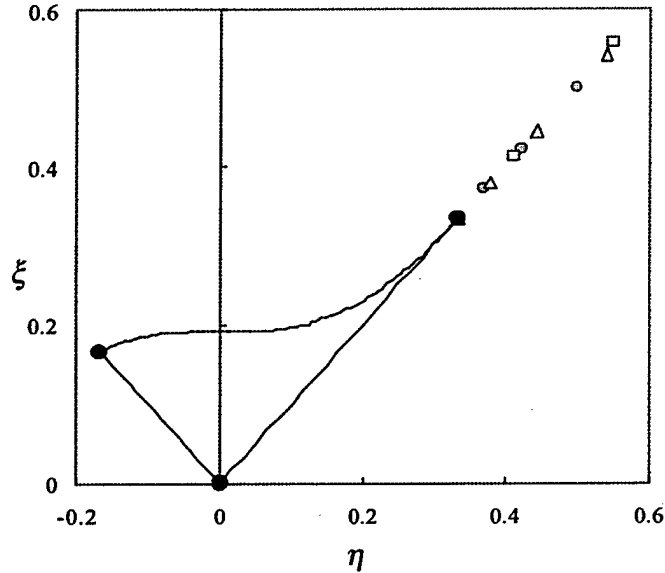


(b)

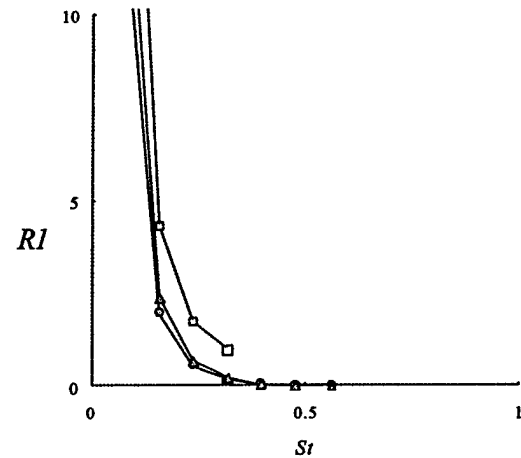


(c)

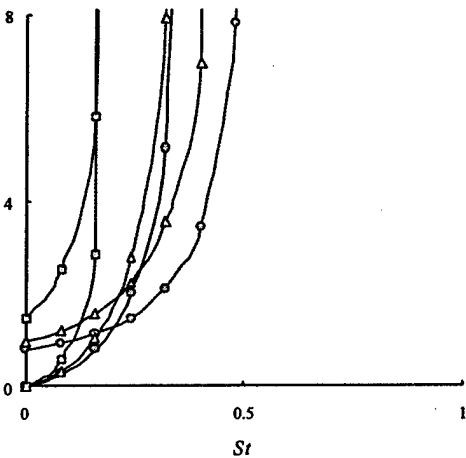
**Fig. 2.6**



(a)



(b)



(c)

**Fig. 2.7**

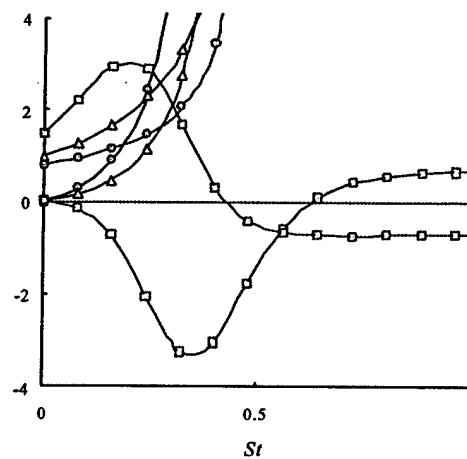
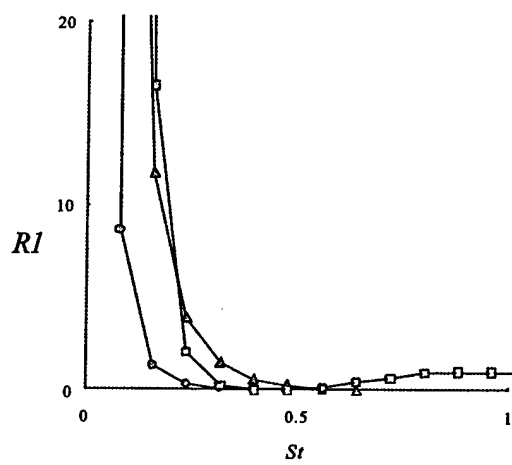
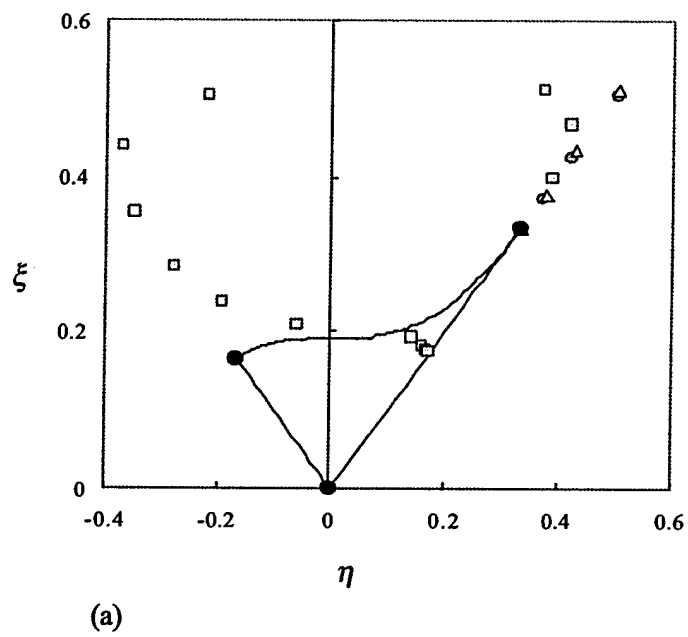
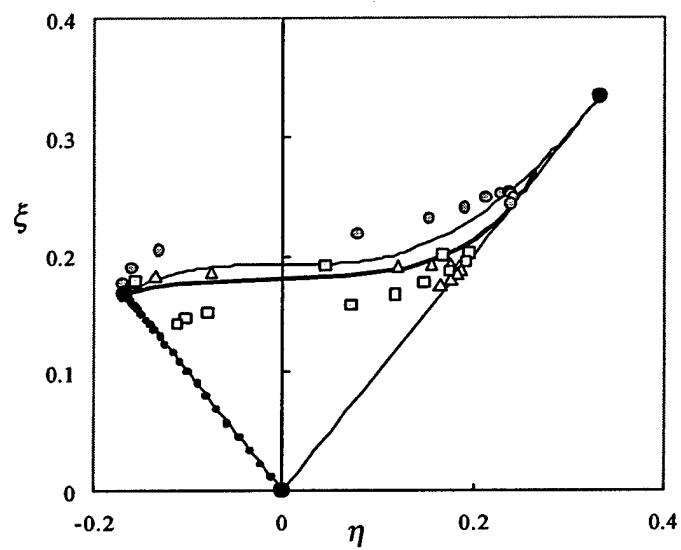
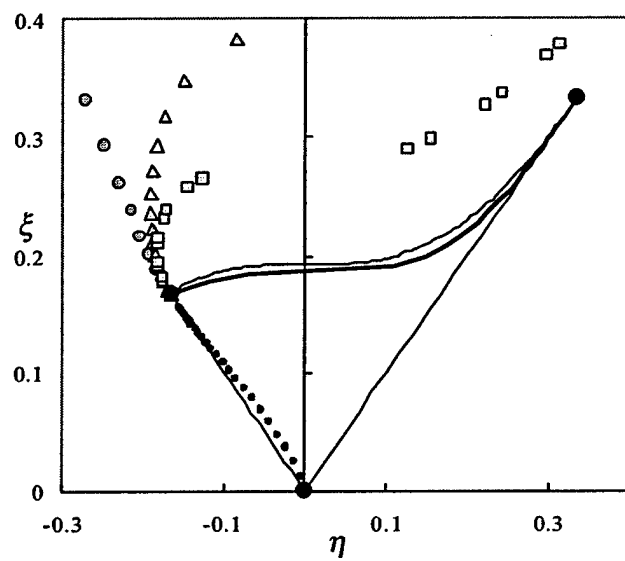


**Fig. 2.8**



(a)



(b)



## CHAPTER 4

### 4.1. Turbulent Transport Models for PANS

The two-equation PANS model as derived by Girimaji, 2003 [1] is as follows

$$\frac{\partial K_u}{\partial t} + U_j \frac{\partial K_u}{\partial x_j} = P_u - \epsilon_u + \frac{\partial}{\partial x_j} \left( \frac{\nu_t}{\sigma_k} \frac{\partial K_u}{\partial x_j} \right) + (U_j - \overline{U_j}) \frac{\partial K_u}{\partial x_j} \quad (1)$$

$$\begin{aligned} \frac{\partial \epsilon_u}{\partial t} + U_j \frac{\partial \epsilon_u}{\partial x_j} = & C_{\epsilon 1} \frac{P_u \epsilon_u}{K_u} - \left( C_{\epsilon 1} + \frac{f_k}{f_\epsilon} (C_{\epsilon 2} - C_{\epsilon 1}) \right) \frac{\epsilon_u^2}{K_u} + \frac{\partial}{\partial x_j} \left( \frac{\nu_t}{\sigma_\epsilon} \frac{\partial \epsilon_u}{\partial x_j} \right) \\ & + (U_j - \overline{U_j}) \frac{\partial \epsilon_u}{\partial x_j} \end{aligned} \quad (2)$$

where the two terms for transport of unresolved kinetic energy and dissipation,  $T_{k_u}$  and  $T_{\epsilon_u}$  are

$$T_{k_u} = \frac{\partial}{\partial x_j} \left( \frac{\nu_t}{\sigma_k} \frac{\partial K_u}{\partial x_j} \right) - (\overline{U_j} - U_j) \frac{\partial K_u}{\partial x_j} \quad (3)$$

$$T_{\epsilon_u} = \frac{\partial}{\partial x_j} \left( \frac{\nu_t}{\sigma_\epsilon} \frac{\partial \epsilon_u}{\partial x_j} \right) - (\overline{U_j} - U_j) \frac{\partial \epsilon_u}{\partial x_j} \quad (4)$$

In the above equations, the unclosed terms that require modeling are the **convection of  $K_u, \epsilon_u$  by resolved fluctuations**  $(\overline{U_j} - U_j)$ . This is considered next. The equations for  $T_{k_u}$  and  $T_{\epsilon_u}$  can be written wholly in terms of PANS variables by expressing the ratio of total viscosity to turbulent Prandtl numbers as

$$\frac{\nu_t}{(\sigma_k, \sigma_\epsilon)} = \frac{C_\mu (K^2/\epsilon)}{(\sigma_k, \sigma_\epsilon)} = \frac{1}{(\sigma_k, \sigma_\epsilon)} \frac{C_\mu K_u^2 f_\epsilon}{\epsilon_u f_k^2} = \frac{\nu_u f_\epsilon}{(\sigma_k, \sigma_\epsilon) f_k^2} \quad (5)$$

In order to close these transport terms completely, we examine two extremes or limits.

**Zero-Transport assumption:** This assumption is based on the fact that the *resolved fluctuations*  $(\overline{U_j} - U_j)$  do not take part in the net transport of unresolved kinetic energy ( $K_u$ ) at the scales of resolution in which we are interested (see Fig 1.).

Let,  $\overline{V_j} = (\overline{U_j} - U_j)$ , then

$$\overline{V_j} K_u = A \quad \text{and} \quad (6)$$

$$\overline{V_j} \epsilon_u = B \quad (7)$$

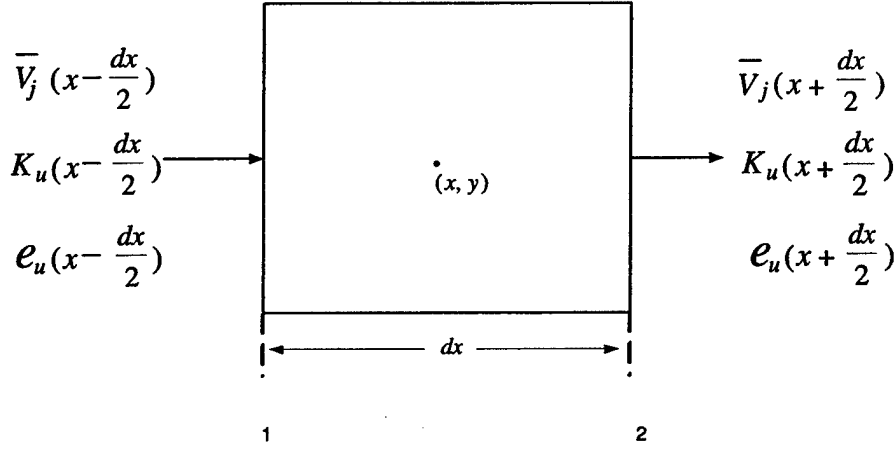


Figure 1: Control Volume showing flux of  $K_u$  and  $\epsilon_u$

Now, the first assumption implies  $(A, B) \approx \text{constant}$  in the scales of interest and hence,

$$\frac{\partial(A, B)}{\partial x_j} = 0 \quad \text{in the large scales of interest} \quad (8)$$

Thus, we are only left with

$$T_{k_u} = \frac{\partial}{\partial x_j} \left( \frac{\nu_u f_\epsilon}{\sigma_k f_k^2} \frac{\partial K_u}{\partial x_j} \right) \quad (9)$$

$$T_{\epsilon_u} = \frac{\partial}{\partial x_j} \left( \frac{\nu_u f_\epsilon}{\sigma_\epsilon f_k^2} \frac{\partial \epsilon_u}{\partial x_j} \right) \quad (10)$$

which is finally written as

$$T_{k_u} = \frac{\partial}{\partial x_j} \left( \frac{\nu_u}{\sigma_{k_u}} \frac{\partial K_u}{\partial x_j} \right) \quad (11)$$

$$T_{\epsilon_u} = \frac{\partial}{\partial x_j} \left( \frac{\nu_u}{\sigma_{\epsilon_u}} \frac{\partial \epsilon_u}{\partial x_j} \right) \quad (12)$$

with the unresolved Prandtl numbers expressed as

$$\sigma_{k_u} = \frac{f_k^2}{f_\epsilon} \sigma_k \quad (13)$$

$$\sigma_{\epsilon_u} = \frac{f_k^2}{f_\epsilon} \sigma_\epsilon \quad (14)$$

**Maximum-Transport Model:** The second case is based on a more generalized gradient-transport closure and states that *the resolved field velocity is proportional to the resolved field eddy viscosity*  $\nu_r$ , which can be defined as

$$\nu_r = \nu_t - \nu_u = C_\mu \frac{K^2}{\epsilon} - C_\mu \frac{K_u^2}{\epsilon_u} \quad (15)$$

Thus,

$$A = \frac{\nu_r}{\sigma_k} \frac{\partial K_u}{\partial x_j} = \frac{(\nu_t - \nu_u)}{\sigma_k} \frac{\partial K_u}{\partial x_j} \quad (16)$$

$$B = \frac{\nu_r}{\sigma_\epsilon} \frac{\partial \epsilon_u}{\partial x_j} = \frac{(\nu_t - \nu_u)}{\sigma_\epsilon} \frac{\partial \epsilon_u}{\partial x_j} \quad (17)$$

and hence

$$\frac{\partial(A)}{\partial x_j} = \frac{\partial}{\partial x_j} \left( \frac{(\nu_t - \nu_u)}{\sigma_k} \frac{\partial K_u}{\partial x_j} \right) \quad (18)$$

$$\frac{\partial(B)}{\partial x_j} = \frac{\partial}{\partial x_j} \left( \frac{(\nu_t - \nu_u)}{\sigma_\epsilon} \frac{\partial \epsilon_u}{\partial x_j} \right) \quad (19)$$

From equations (3.3) and (3.4), we get

$$\begin{aligned} (T_{k_u}, T_{\epsilon_u}) &= \frac{\partial}{\partial x_j} \left( \frac{\nu_t}{(\sigma_k, \sigma_\epsilon)} \frac{\partial(K_u, \epsilon_u)}{\partial x_j} \right) - \frac{\partial}{\partial x_j} \left( \frac{(\nu_t - \nu_u)}{(\sigma_k, \sigma_\epsilon)} \frac{\partial(K_u, \epsilon_u)}{\partial x_j} \right) \\ &= \frac{\partial}{\partial x_j} \left( \frac{\nu_u}{(\sigma_k, \sigma_\epsilon)} \frac{\partial(K_u, \epsilon_u)}{\partial x_j} \right) \end{aligned} \quad (20)$$

which is expressed explicitly as,

$$T_{k_u} = \frac{\partial}{\partial x_j} \left( \frac{\nu_u}{\sigma_{k_u}} \frac{\partial K_u}{\partial x_j} \right) \quad \text{and} \quad (21)$$

$$T_{\epsilon_u} = \frac{\partial}{\partial x_j} \left( \frac{\nu_u}{\sigma_{\epsilon_u}} \frac{\partial \epsilon_u}{\partial x_j} \right) \quad (22)$$

with the modified Prandtl numbers for unresolved kinetic energy and dissipation as,

$$\sigma_{k_u} = \sigma_k \quad (23)$$

$$\sigma_{\epsilon_u} = \sigma_\epsilon \quad (24)$$

If we consider a continuum (Fig.1) whose width ( $dx$ ) corresponds to an order of length equal to the intermediate scales of motion, then the flux of  $K_u$  (or  $\epsilon_u/e_u$ ) between regions 1 and 2 of the continuum is given by

$$\overline{V}_j(x + \frac{dx}{2}) K_u(x + \frac{dx}{2}) - \overline{V}_j(x - \frac{dx}{2}) K_u(x - \frac{dx}{2}) \quad (25)$$

Expanding each term in a Taylor series and after cancelling various terms, we are left with the convection term for  $K_u$ ,  $\overline{V}_j \frac{\partial K_u}{\partial x_j}$  and similarly  $\epsilon_u$ ,  $\overline{V}_j \frac{\partial \epsilon_u}{\partial x_j}$ . Now since  $\epsilon_u$  is a small-scale quantity and consequently its statistics converge to a mean value quickly, for a given width of the continuum, it is reasonable to assume that its mean changes slowly between regions 1 and 2, and hence its gradient (or transport) is negligibly small in the region of interest.i.e.

$$\frac{\partial \epsilon_u}{\partial x_j} \approx 0 \quad (26)$$

Thus, in equation (3.4) the only remaining term is the viscous transport term

$$T_{\epsilon_u} = \frac{\partial}{\partial x_j} \left( \frac{\nu_t}{\sigma_\epsilon} \frac{\partial \epsilon_u}{\partial x_j} \right) \quad (27)$$

where the ratio of the total viscosity ( $\nu_t$ ) to the dissipation Prandtl number ( $\sigma_\epsilon$ ) can be written as

$$\frac{\nu_t}{\sigma_\epsilon} = \frac{C_\mu \frac{K^2}{\epsilon}}{\sigma_\epsilon} = \frac{C_\mu \frac{K_u^2}{\epsilon_u}}{\sigma_\epsilon \frac{f_k^2}{f_\epsilon}} = \frac{\nu_u}{\sigma_{\epsilon_u}} \quad (28)$$

which is essentially the **Zero-Transport** model for unresolved dissipation  $\epsilon_u$ .

In the equation for  $K_u$  however, transport terms due to both viscosity and resolved fluctuations exist, as  $K_u$  is a large scale quantity whose mean changes considerably between regions 1 and 2 and therefore its gradient (or transport) between regions 1 and 2 of the continuum is significant and cannot be neglected. Hence, in this case we have

$$T_{k_u} = \frac{\partial}{\partial x_j} \left( \frac{\nu_t}{\sigma_k} \frac{\partial K_u}{\partial x_j} \right) - (\overline{U_j} - U_j) \frac{\partial K_u}{\partial x_j} \quad (29)$$

and therefore make use of the second assumption based on gradient-transport closure and obtain

$$\begin{aligned} T_{k_u} &= \frac{\partial}{\partial x_j} \left( \frac{\nu_t}{\sigma_k} \frac{\partial K_u}{\partial x_j} \right) - \frac{\partial}{\partial x_j} \left( \frac{(\nu_t - \nu_u)}{\sigma_k} \frac{\partial K_u}{\partial x_j} \right) \\ &= \frac{\partial}{\partial x_j} \left( \frac{\nu_u}{\sigma_k} \frac{\partial K_u}{\partial x_j} \right) \end{aligned} \quad (30)$$

which is essentially the **Maximum-Transport** model for unresolved kinetic energy,  $K_u$ . This proves that the ZT model is better suited for modeling unresolved dissipation ( $\epsilon_u$ ), while the MT model is adequate for unresolved kinetic energy ( $K_u$ ).

**Objective:** The objective of the current study is to determine which of these two transport models performs better for  $K_u$  and  $\epsilon_u$ .

## 4.2. RESULTS AND DISCUSSION

### 4.2.1. Maximum-Transport Vs Zero-Transport Model

In this section, the unsteady and turbulent flow results from numerical simulations conducted on the three-dimensional lid-driven cavity flow for a spanwise aspect ratio ( $SAR = 2L/W$ ) of 3:1:1 are presented and compared with published experimental observations and LES (Jordan, 1994 [2]). The results present comparisons made between simulations conducted using the Maximum-Transport (MT) and the Zero-Transport (ZT) models to ascertain which of the models performs better for  $K_u$  and  $\epsilon_u$ . Qualitative comparisons are available in terms of contours of X-vorticity, while quantitative comparisons with LES are realized through plots of Centerline Mean Velocities at a  $z = 0.28$  plane, although experimental results are available at the symmetry plane.

All figures have been generated on completion of the flow simulation corresponding to a flow time ( $T$ ) of approximately 115 seconds. The plots for statistical quantities along cavity centerlines have been generated such that for the first 10 cycles (corresponding to about 60 seconds of flow time), no sampling of data is done in order for the flow to become fully turbulent, after which data is sampled every 6.5 seconds to obtain realizations of mean quantities. Results have been presented for  $f_k$  values of 1.0 (RANS), 0.7 and 0.4.

Figures 2 and 3 show snapshots of the mean  $U$  and  $V$  velocity profiles along the cavity centerlines, while Fig. 4 presents contours of X-vorticity for a typical RANS ( $f_k=1$ ) simulation. Very few flow features are visible in the contour plots which illustrates the fact that RANS is inherently incapable of capturing many of the flow features and the results for statistical quantities show its inability to produce accurate results, especially near the boundaries of the cavity.

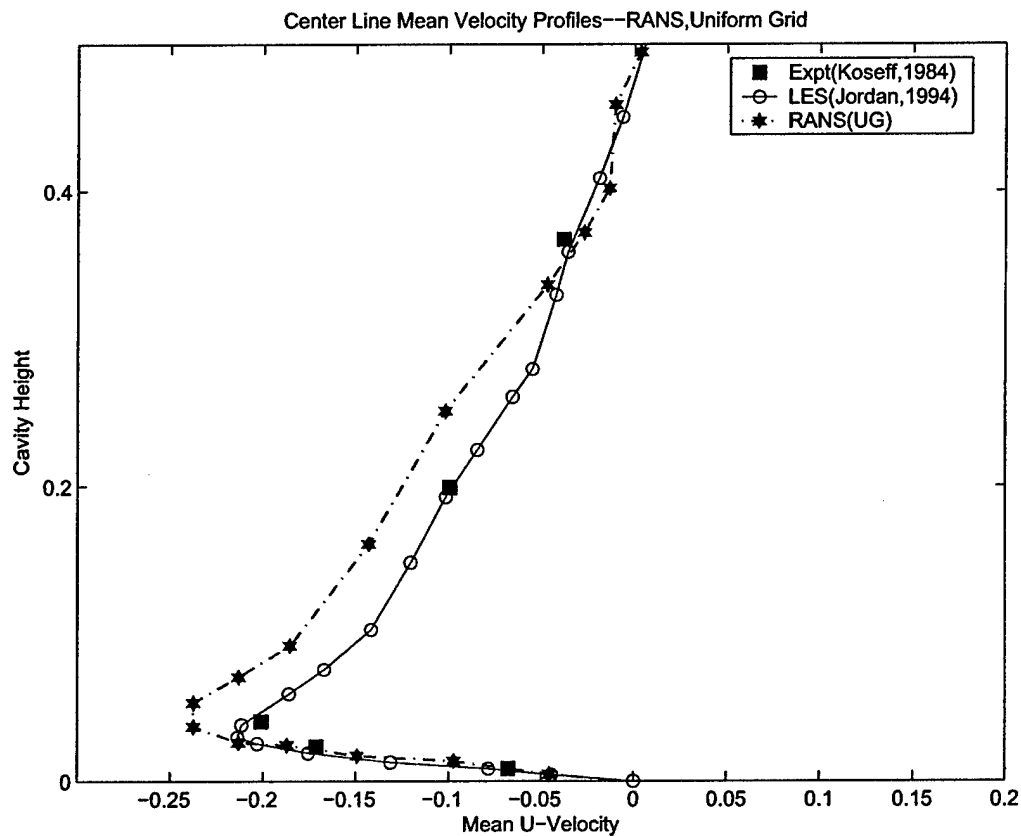


Figure 2: Mean U-Velocity profiles, bottom wall closeup, (RANS, UG)

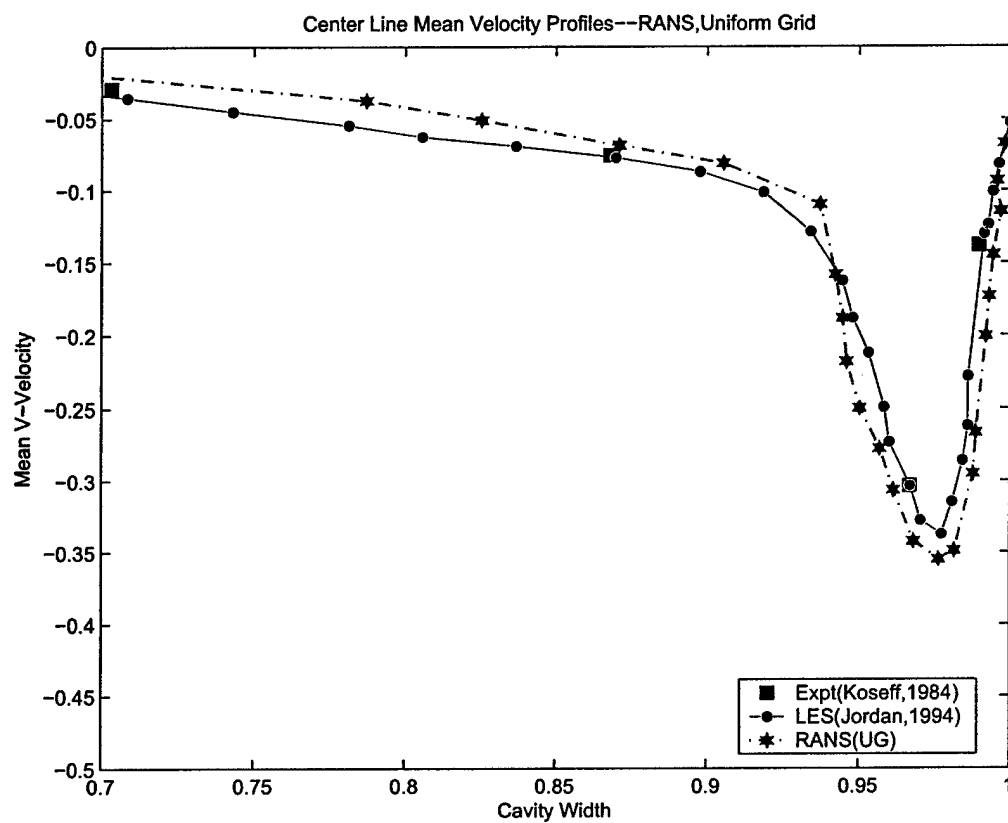


Figure 3: Mean V-Velocity profiles, downstream wall closeup, (RANS, UG)

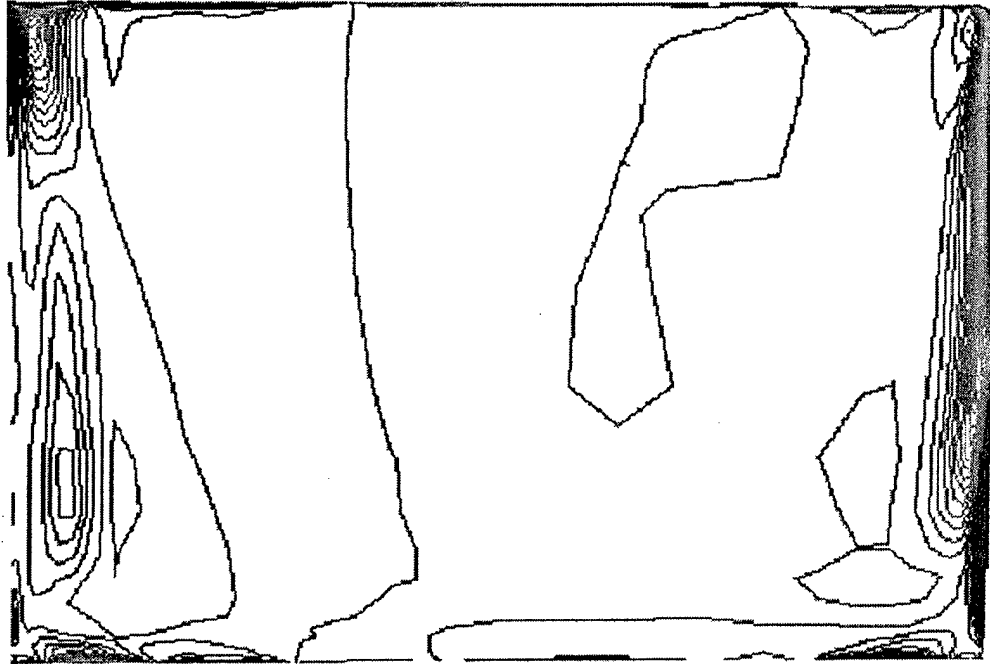


Figure 4: X-Vorticity Contours along downstream wall, (RANS, UG)

The next set of figures (5-13) show comparisons of the two turbulent transport models, ZT and MT, with each other as well as against LES and experiment. From the statistical comparisons for  $f_k = 0.7$  (Figs. 5, 6), it appears that (i) both models seem to be performing better than RANS and show greater convergence of the PANS calculations towards LES results; and (ii) the plots also illustrate the fact that the ZT model performs marginally better than the corresponding MT model near the cavity boundaries. Although marginally better accuracy is observed from the statistical comparisons, instantaneous X-Vorticity contours (Figs. 7 and 8) along the downstream wall display the fact that considerably more scales of flow are resolved by the ZT model when compared to the MT model, while both models are able to uncover significantly more scales of flow than RANS, in terms of appearance of Taylor Goertler (TGL) vortex pairs. About three pairs of TGL vortices are observed for the ZT model (Fig. 7) while only one pair can be seen for the MT model (Fig. 8), for a value of  $f_k=0.7$ .

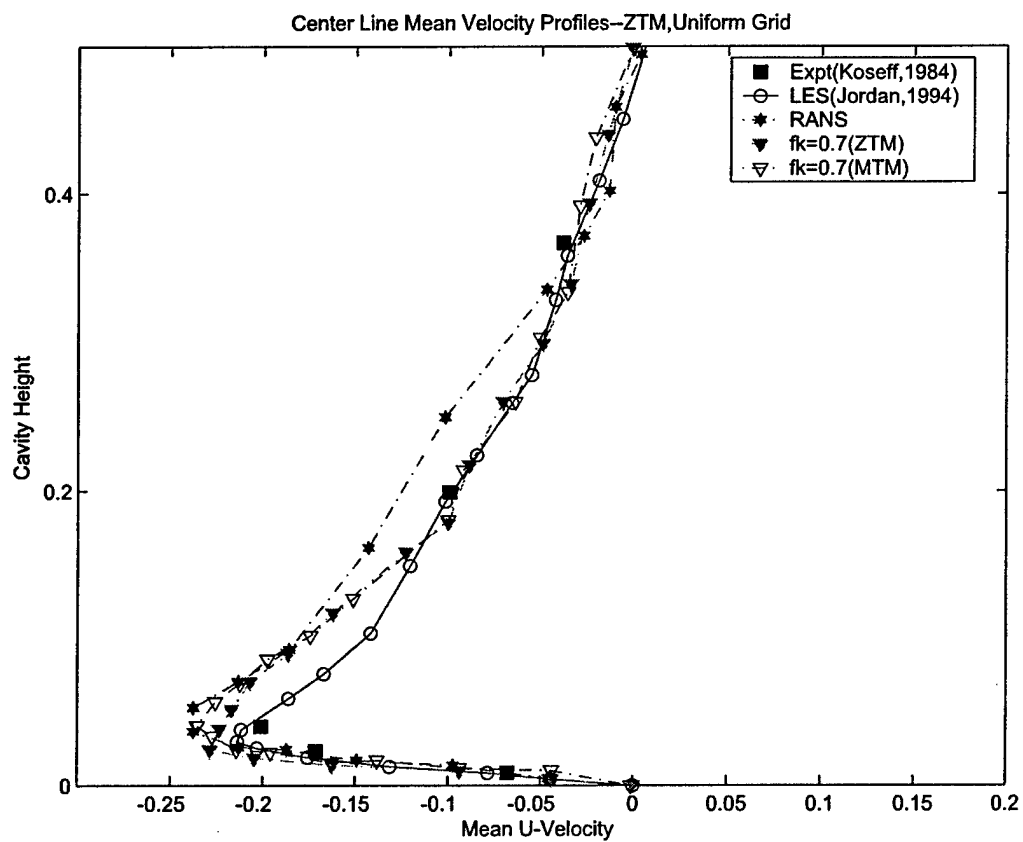


Figure 5: Mean U-Velocity profiles, bottom wall closeup,  $f_k = 0.7$ , (ZT Vs MT)



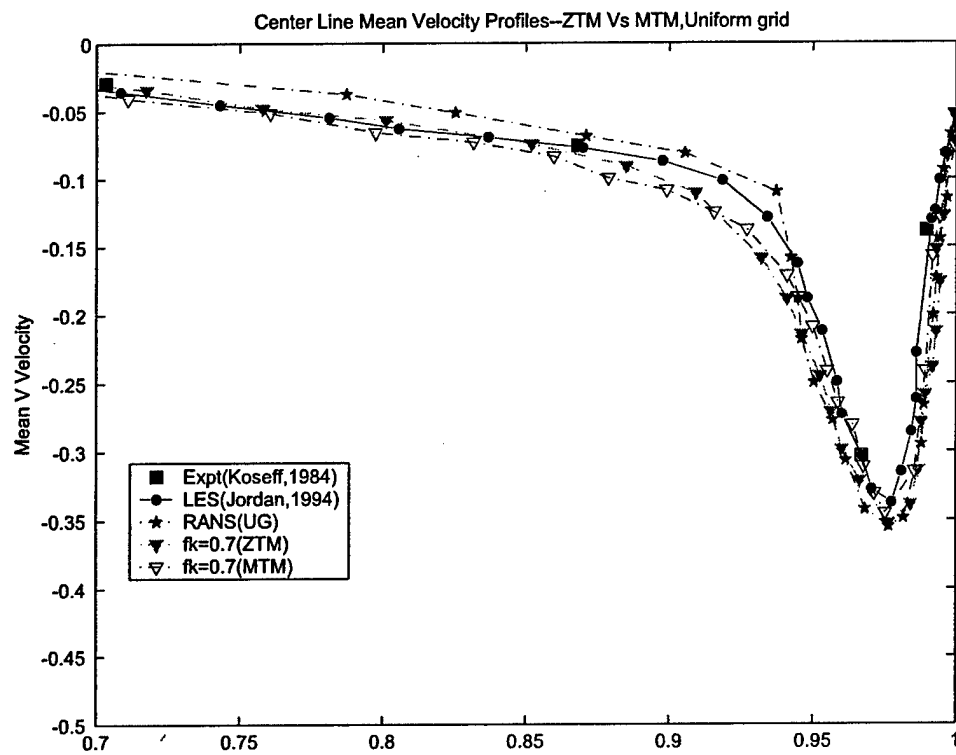


Figure 6: Mean V-Velocity profiles, downstream wall closeup,  $f_k = 0.7$ , (ZT Vs MT)

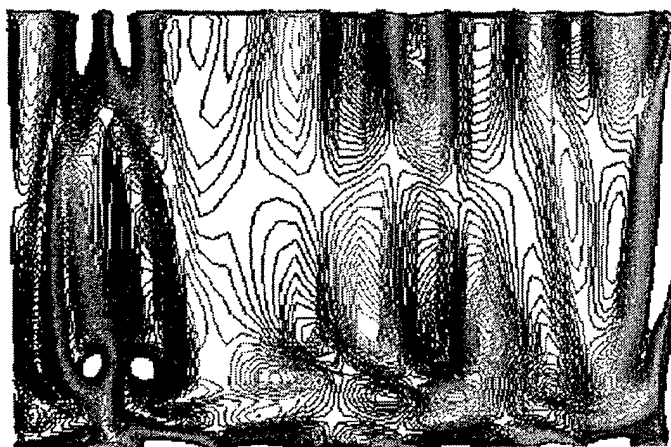


Figure 7: X-Vorticity Contours along downstream wall,  $f_k = 0.7$ , (ZT, UG)

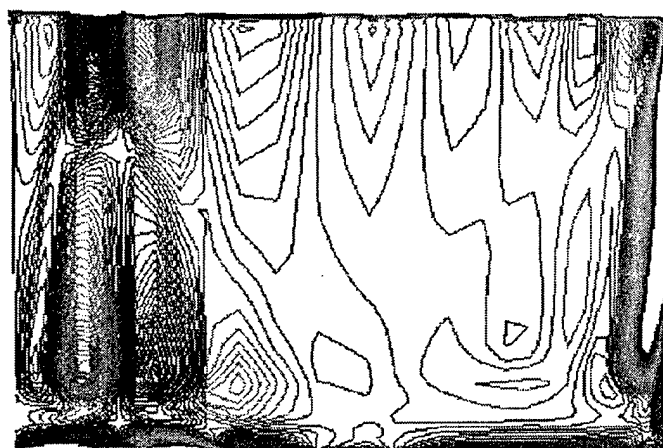


Figure 8: X-Vorticity Contours along downstream wall,  $f_k = 0.7$ , (MT, UG)

As the value of  $f_k$  is reduced, more and more pairs of vortices are uncovered and the number of flow features resolved by the ZT model is considerably more than the corresponding MT model for a given  $f_k$ , specifically, 5 pairs of TGL vortices are observed for the ZT model as against 3 pairs for the MT model, for  $f_k=0.4$  (Figs. 11, 12). Statistical comparisons for the models indicate that although both models seem to perform fairly well along the center of the cavity, the ZT model appears to perform better than the MT model in the layers adjoining the upper and lower boundaries. Further, as the value of  $f_k$  is reduced, the ZT model shows closer agreement with LES and experiment than the corresponding MT model, for a given  $f_k$ . This trend is evident in figure 9, 10 ( $f_k = 0.4$ ).

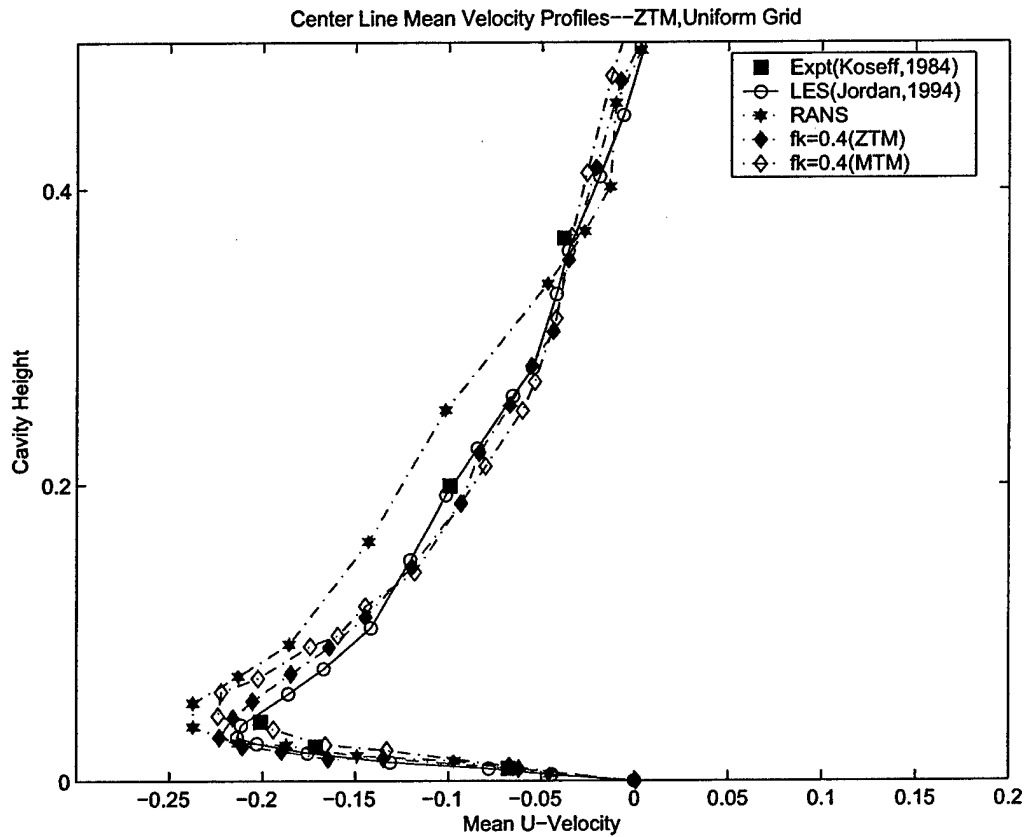


Figure 9: Mean U-Velocity profiles, bottom wall closeup,  $f_k = 0.4$ , (ZT Vs MT)

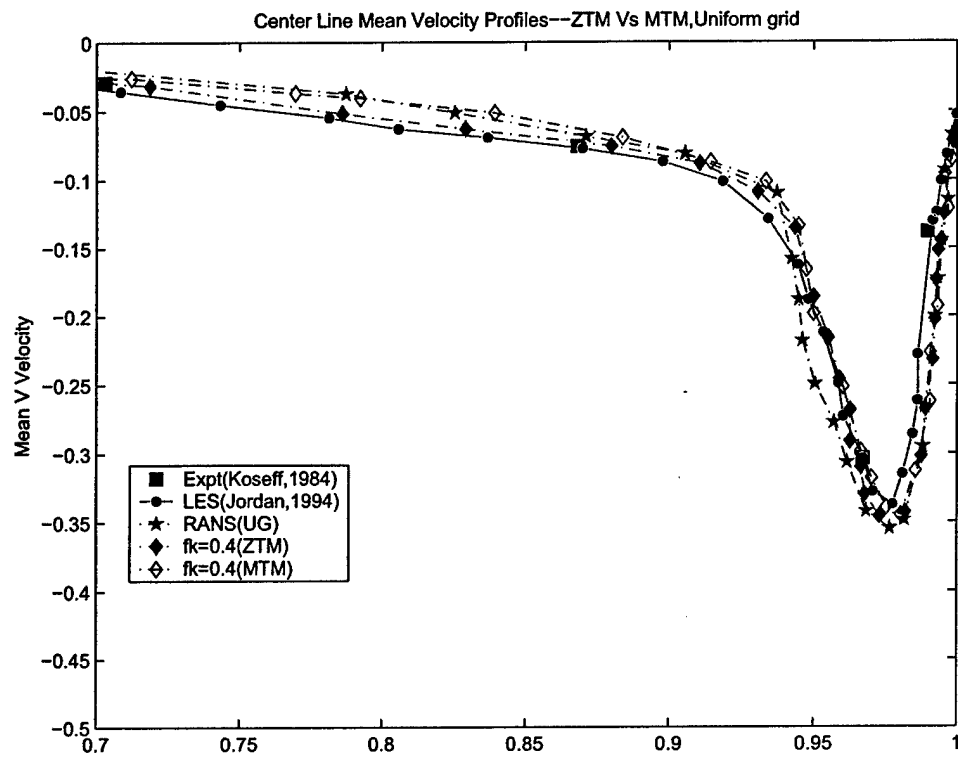


Figure 10: Mean V-Velocity profiles, downstream wall closeup,  $f_k = 0.4$ , (ZT Vs MT)

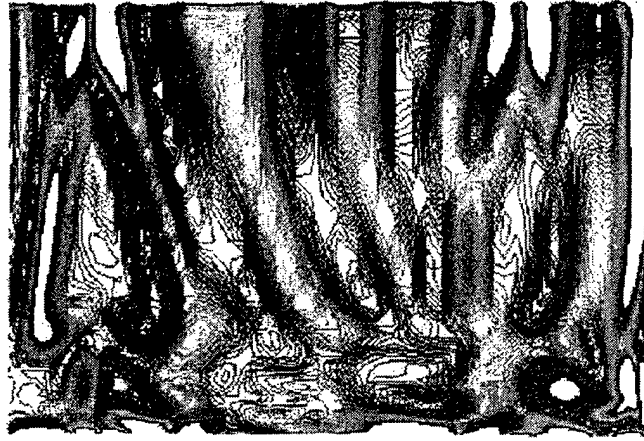


Figure 11: X-Vorticity Contours along downstream wall,  $f_k = 0.4$ , (ZT, UG)

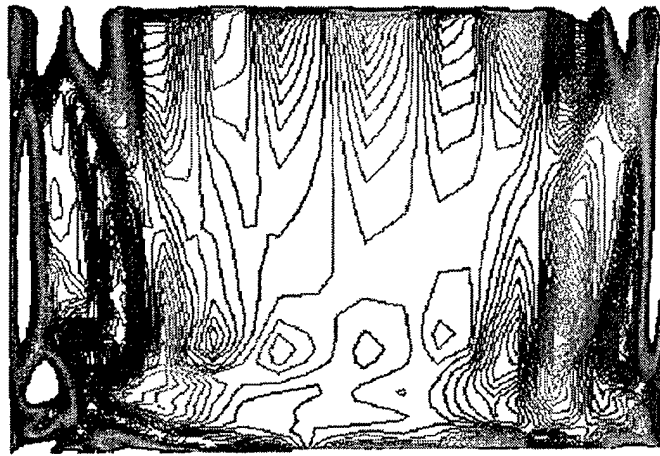


Figure 12: X-Vorticity Contours along downstream wall,  $f_k = 0.4$ , (MT, UG)

Finally, two important inferences that can be drawn from these results are (i) the ZT model performs better than the corresponding MT model for a given  $f_k$  and (ii) as the value of  $f_k$  is decreased, better convergence towards LES and experiment is observed. The second inference is especially evident in plots 13-16. Figures 17-20 show a comparison between plots of contours of X-vorticity for various  $f_k$  values and essentially display the fact that a reduction in the value of  $f_k$  causes more and more scales to be resolved.

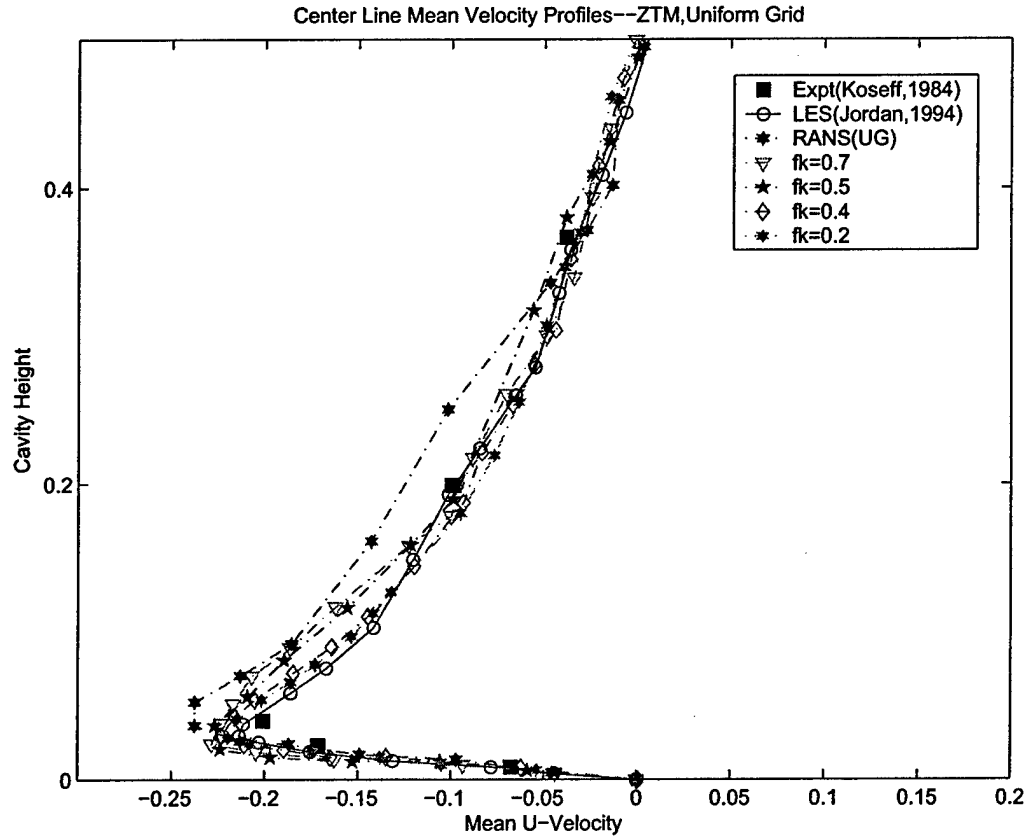


Figure 13: Mean U-Velocity profiles, bottom wall closeup, (ZT, UG)

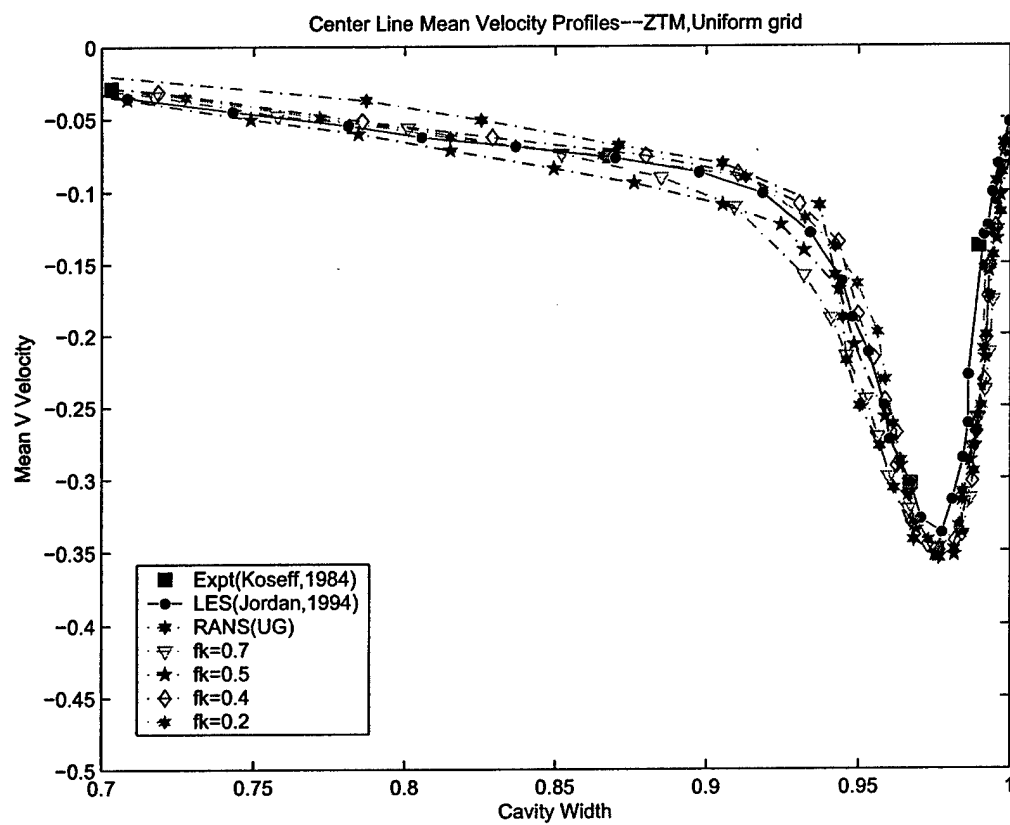


Figure 14: Mean V-Velocity profiles, downstream wall closeup, (ZT, UG)



Figure 15: X-Vorticity Contours:  $f_k = 0.2$



Figure 16: X-Vorticity Contours:  $f_k = 0.4$

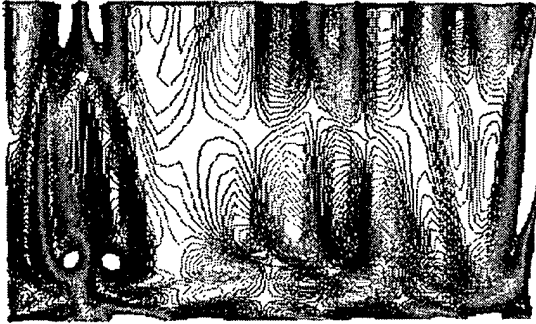


Figure 17: X-Vorticity Contours:  $f_k = 0.7$

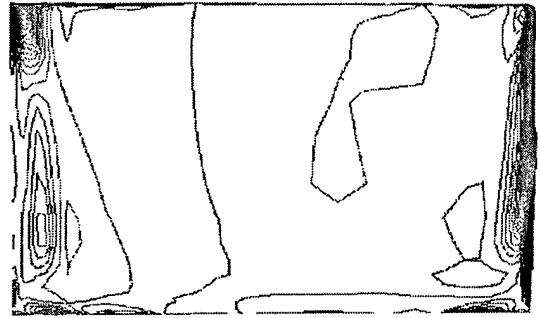


Figure 18: X-Vorticity Contours: RANS

#### 4.3. CONCLUSIONS AND SUMMARY

In the present study, a detailed numerical investigation of the three-dimensional lid-driven cavity flow is carried out using a new turbulence modeling technique, known as the Partially Averaged Navier Stokes method or PANS. Flow studies have been conducted at  $Re=10000$  on a lid-driven cavity for a spanwise aspect ratio (SAR) of 3:1:1, with the top surface imparted with a constant velocity of 1 m/s. The investigation primarily focuses on the effects of two turbulent transport models (the Zero-Transport (ZT) and Maximum-Transport (MT)) on PANS calculations to ascertain which model performs better for  $K_u$  and  $\epsilon_u$ .



The main conclusions that can be drawn by observing all the results are: (i) as the value of  $f_k$  is decreased from 1 (RANS) to 0 (DNS) more scales of flow are resolved in terms of the appearance of flow features, such as the TGL vortices, as evident from the contour plots of X-vorticity, and more importantly (ii) the ZT model appears to perform better than the MT model. As a final note, in view of all the results, it seems justifiable to conclude that the PANS model is capable of serving as **abridging model** between RANS and DNS.

## References

- [1] Girimaji, S. S., 2003, "Partially-Averaged Navier-Stokes Method: A Variable Resolution (from RANS to DNS) Turbulence Model", submitted to *Physics of Fluids*.
- [2] Jordan, S. A., and Ragab, S. A., 1994, "On the Unsteady and Turbulent Characteristics of Three-Dimensional Shear-Driven Cavity flow ", *Journal of Fluids Engineering*, Vol. 116, pp. 439-449.